

1 **Drosophila Synaptotagmin 7 negatively regulates synaptic vesicle fusion and replenishment**
2 **in a dosage-dependent manner**

3

4 Zhuo Guan*, Mónica C. Quiñones-Frías*, Yulia Akbergenova, J. Troy Littleton

5

6 The Picower Institute for Learning and Memory, Department of Biology and Department of Brain
7 and Cognitive Sciences, Massachusetts Institute of Technology, Cambridge, MA 02139

8

9 * Z.G. and M.C.Q.F. contributed equally to this work.

10

11 Correspondence and requests for materials should be addressed to J.T.L. (troy@mit.edu).

12

13 The authors declare no competing interests.

14 **Abstract**

15 Synchronous neurotransmitter release is triggered by Ca^{2+} binding to the synaptic vesicle protein
16 Synaptotagmin 1, while asynchronous fusion and short-term facilitation is hypothesized to be
17 mediated by plasma membrane-localized Synaptotagmin 7 (SYT7). We generated mutations in
18 *Drosophila Syt7* to determine if it plays a conserved role as the Ca^{2+} sensor for these processes.
19 Electrophysiology and quantal imaging revealed evoked release was elevated 2-fold. *Syt7* mutants
20 also had a larger pool of readily-releasable vesicles, faster recovery following stimulation, and
21 robust facilitation. *Syt1/Syt7* double mutants displayed more release than *Syt1* mutants alone,
22 indicating SYT7 does not mediate the residual asynchronous release remaining in the absence of
23 SYT1. SYT7 localizes to an internal membrane tubular network within the peri-active zone, but
24 does not enrich at release sites. These findings indicate the two Ca^{2+} sensor model of SYT1 and
25 SYT7 mediating all phases of neurotransmitter release and facilitation is not applicable at
26 *Drosophila* synapses.

27

28 Introduction

29 Neurotransmitter release from presynaptic terminals is the primary mechanism of synaptic
30 communication and is mediated by fusion of synaptic vesicles (SVs) with the plasma membrane
31 at specific sites known as active zones (AZs) (Katz, 1969; Südhof, 2013; Zhai and Bellen, 2004).
32 A highly conserved protein machinery composed of the SNARE complex drives fusion between
33 the SV and AZ lipid bilayers (Littleton et al., 1998; Söllner et al., 1993; Sutton et al., 1998; Tucker
34 et al., 2004). Ca^{2+} influx through voltage-gated Ca^{2+} channels functions as the trigger to activate
35 the fusion process (Borst and Sakmann, 1996; Katz and Miledi, 1970, 1967; Schneggenburger and
36 Rosenmund, 2015; Südhof, 2012). The majority of SVs fuse during a synchronous phase that
37 occurs within a few milliseconds of Ca^{2+} entry (Borst and Sakmann, 1996; Goda and Stevens,
38 1994; Llinás et al., 1981; Sabatini and Regehr, 1996; Yoshihara and Littleton, 2002). Many
39 synapses also have an asynchronous component that results in SV release over hundreds of
40 milliseconds (Goda and Stevens, 1994; Hefft and Jonas, 2005; Kaeser and Regehr, 2014;
41 Yoshihara and Littleton, 2002). Asynchronous release normally accounts for less than 5% of SV
42 fusion following single action potentials at *Drosophila* neuromuscular junctions (NMJs) (Jorquera
43 et al., 2012). This slower phase of release becomes more prominent during high rates of stimulation
44 (Atluri and Regehr, 1998; Lu and Trussell, 2000; Rozov et al., 2019; Zucker and Regehr, 2002)
45 and mediates all SV fusion at some neuronal connections (Best and Regehr, 2009; Peters et al.,
46 2010). Changes in the kinetics and amount of SV fusion also occur during high frequency
47 stimulation, resulting in facilitation or depression depending on the synapse (Zucker and Regehr,
48 2002). Defining the molecular machinery and Ca^{2+} sensors that regulate the distinct modes and
49 kinetics of SV release is essential for understanding synaptic transmission.

50 The Synaptotagmin (SYT) family of Ca^{2+} binding proteins contain key regulators that control
51 the timing of SV release. SYT proteins contain a transmembrane domain and two Ca^{2+} binding C2
52 domains termed C2A and C2B (Adolfson et al., 2004; Adolfson and Littleton, 2001; Perin et al.,
53 1990; Sugita et al., 2002; Ullrich and Südhof, 1995). Mammals have three SYT family members
54 that localize to SVs (SYT1, SYT2 and SYT9), while *Drosophila* contains a single member of the
55 SV subfamily (SYT1) (Littleton et al., 1993a; Pang et al., 2006; Xu et al., 2007). These SYT
56 isoforms bind Ca^{2+} and activate synchronous fusion of SVs via interactions with membranes and
57 the SNARE complex (Chang et al., 2018; Chapman and Jahn, 1994; Fernández-Chacón et al.,
58 2001; Geppert et al., 1994; Guan et al., 2017; Lee et al., 2013; Lee and Littleton, 2015; Littleton

59 et al., 1994, 1993b; Mackler et al., 2002; Nishiki and Augustine, 2004; Tucker et al., 2004; Xu et
60 al., 2007; Yoshihara and Littleton, 2002; Young and Neher, 2009). Beyond SV localized SYTs,
61 SYT7 is the only other family member implicated in Ca²⁺-dependent SV trafficking, although
62 additional SYT isoforms participate in Ca²⁺-dependent fusion of other secretory organelles and
63 dense core vesicles (DCVs) (Adolfson et al., 2004; Cao et al., 2011; Dean et al., 2012; Li et al.,
64 1995; Moghadam and Jackson, 2013; Park et al., 2014; Shin et al., 2002; Yoshihara et al., 2005).

65 Multiple mechanisms have been proposed to mediate the asynchronous component of
66 neurotransmitter release, including distinct Ca²⁺ sensors, heterogeneity in SV protein content, SV
67 distance from Ca²⁺ channels, distinct Ca²⁺ entry pathways, or regulation of Ca²⁺ extrusion and
68 buffering (Chanaday and Kavalali, 2018; Fesce, 1999; Kaeser and Regehr, 2014; Pang and Südhof,
69 2010; Rozov et al., 2019; Zucker and Regehr, 2002). Although several mechanisms may
70 contribute, the observation that *Syt1* mutants have enhanced asynchronous release indicates
71 another Ca²⁺ sensor(s) activates the remaining slower Ca²⁺-dependent component of exocytosis
72 (Huson et al., 2019; Kochubey and Schneggenburger, 2011; Nishiki and Augustine, 2004; Turecek
73 and Regehr, 2019; Yang et al., 2010; Yoshihara et al., 2010; Yoshihara and Littleton, 2002).
74 Though controversial, SYT7 has emerged as a popular candidate for the asynchronous Ca²⁺ sensor
75 (Bacaj et al., 2013; Chen et al., 2017; Maximov et al., 2008; Saraswati et al., 2007; Turecek and
76 Regehr, 2019, 2018; Weber et al., 2014; Wen et al., 2010). SYT7 has also been postulated to
77 function as the Ca²⁺ sensor for short-term synaptic facilitation (Chen et al., 2017; Jackman et al.,
78 2016; Turecek and Regehr, 2018). SYT7 has higher Ca²⁺ sensitivity, tighter membrane binding
79 affinity and longer Ca²⁺-lipid disassembly kinetics than SYT1 (Hui et al., 2005; Sugita et al., 2002,
80 2001; Voleti et al., 2017). These properties suggest SYT7 may regulate SV dynamics farther away
81 from the AZ Ca²⁺ nanodomains that are required for SYT1 activation, or during temporal windows
82 following the decay of the initial peak of Ca²⁺ influx. Together, these data have led to a two Ca²⁺
83 sensor model for evoked SV exocytosis, with SYT1 triggering the rapid synchronous phase of
84 neurotransmitter release and SYT7 mediating asynchronous fusion and facilitation.

85 Although SYT7 manipulations can alter asynchronous release and facilitation at some
86 synapses, several studies have suggested alternative explanations for the reduced fusion or
87 identified unrelated defects in SV trafficking (Figure 1A). The recent observation that
88 asynchronous release at mammalian synapses is anti-correlated with the levels of the synchronous
89 Ca²⁺ sensors SYT1 and SYT2, but does not correlate with SYT7, prompted re-interpretation of

90 earlier data on the protein's function (Turecek and Regehr, 2019). Besides asynchronous release,
91 mammalian SYT7 has been implicated in SV endocytosis, SV replenishment, SV pool mobility,
92 and DCV fusion and replenishment (Bacaj et al., 2015; Dolai et al., 2016; Durán et al., 2018;
93 Fukuda et al., 2004; Gustavsson et al., 2011; Li et al., 2017; Liu et al., 2014; Schonn et al., 2008;
94 Tsuboi and Fukuda, 2007; Virmani et al., 2003; Wu et al., 2015). SYT7 has also been shown to
95 regulate cell migration, lysosomal fusion and membrane repair in non-neuronal cells (Barzilai-
96 Tutsch et al., 2018; Chakrabarti et al., 2003; Colvin et al., 2010; Czubener et al., 2006; Flannery et
97 al., 2010; Jaiswal et al., 2004; Martinez et al., 2000; Reddy et al., 2001; Zhao et al., 2008).

98 Similar to the uncertainty surrounding SYT7 function, its subcellular localization is also
99 unclear, with different studies localizing the protein to the plasma membrane, DCVs, lysosomes,
100 endosomes or other internal compartments (Adolfson et al., 2004; Czubener et al., 2006; Flannery
101 et al., 2010; Martinez et al., 2000; Mendez et al., 2011; Monterrat et al., 2007; Schonn et al., 2008;
102 Shin et al., 2002; Sugita et al., 2001; Zhao et al., 2008). A key supporting argument for SYT7 as
103 the asynchronous Ca^{2+} sensor is its reported localization to the AZ plasma membrane, positioning
104 it at sites of SV fusion (Sugita et al., 2001). If SYT7 were present on endosomes or other internal
105 membrane compartments, it would be more compatible with a role in SV trafficking rather than
106 the fusion process itself. In summary, conflicting studies have generated confusion over how SYT7
107 contributes to neurotransmission and if the protein plays distinct roles across different neuronal
108 subpopulations or species.

109 To examine the function of SYT7 in *Drosophila*, we generated and characterized *Syt7* null
110 mutants. The *Drosophila* NMJ exhibits similar asynchronous release and facilitation properties to
111 those of mammals (Jan and Jan, 1976; Jorquera et al., 2012; Yoshihara and Littleton, 2002),
112 making it a useful system to examine evolutionary conserved functions of SYT7 in
113 neurotransmitter release. *Syt7* mutants and *Syt1*; *Syt7* double mutants display increased evoked
114 neurotransmitter release, indicating SYT7 negatively regulates SV fusion independent of SYT1.
115 In addition, CRISPR-mediated tagging of the endogenous *Syt7* locus indicates SYT7 localizes to
116 a tubular network inside the presynaptic terminal that resides within the peri-active zone (peri-AZ)
117 region, but is not enriched at sites of SV fusion. These data define a role for SYT7 in restricting
118 SV availability and fusion, and indicate SYT7 is not a major Ca^{2+} sensor for asynchronous release
119 and facilitation in *Drosophila*.

120 **Results**

121 **Evolutionary conservation and structural comparison of SYT1 and SYT7**

122 Synaptotagmins form one of the largest protein families involved in membrane tracking, with
123 17 *Syt* genes encoded in mammals and 7 *Syt* genes found in *Drosophila* (Adolfson and Littleton,
124 2001; Craxton, 2010; Sugita et al., 2002). Unlike the SV subfamily of SYTs, only a single *Syt7*
125 gene is present in vertebrate and invertebrate genomes, making phenotypic comparisons easier. To
126 examine the evolutionary relationship between SYT1, SYT7 and the more distantly related
127 extended-Synaptotagmin (E-SYT) proteins, a phylogenetic tree was generated using the
128 BLOSUM62 matrix and neighbor joining clustering analysis with protein sequences from placozoa
129 (*Trichoplax adhaerens*), invertebrates (*Caenorhabditis elegans*, *Drosophila melanogaster*, *Ciona*
130 *intestinalis*) and vertebrates (*Danio rerio*, *Rattus norvegicus*, *Homo sapiens*, Figure 1B). Although
131 *Trichoplax* lacks neurons, it is the earliest metazoan that encodes *Syt* genes and contains both a
132 SYT1 and SYT7 homolog (Barber et al., 2009). The phylogenetic tree contains independent
133 clusters that correspond to the SYT1, SYT7 and E-SYT2 protein families. The clustering of SYT1
134 homologs across evolution correlates with nervous system complexity, with the *Trichoplax*
135 homolog forming the outlier member of the cluster. Within the SYT7 cluster, *C. elegans* SYT7 is
136 the most distantly related member, with the *Trichoplax* homolog residing closer within the cluster.
137 *Drosophila* SYT7 is more distant from the vertebrate subfamily clade than is *Drosophila* SYT1
138 within its subfamily, suggesting SYT7 sequence conservation is not as closely related to nervous
139 system complexity as SYT1. These observations are consistent with SYT7's broader expression
140 pattern and function within neuronal and non-neuronal cells (MacDougall et al., 2018).

141 To compare SYT1 and SYT7 proteins, we performed homology modeling between
142 *Drosophila* SYT7 and the published structure of mammalian SYT7 (*R. norvegicus* SYT7; PBD:
143 6ANK) (Voleti et al., 2017). Key structural features are highly conserved in the homology model,
144 including the eight-stranded β -barrel and the Ca^{2+} binding loops that form the core of C2 domains
145 (Figure 1C). In contrast to SYT1, both *Drosophila* and mammalian SYT7 lack the C2B HB helix
146 previously found to have an inhibitory role in SV fusion (Xue et al., 2010). We next performed
147 sequence alignment of SYT proteins from *H. sapiens*, *R. norvegicus* and *D. melanogaster* (Figure
148 1 – figure supplement 1). *Drosophila* SYT7 is 59% identical to human SYT7. Comparing the SYT1
149 and SYT7 subfamilies, the N-terminus encoding the transmembrane domain and linker region has
150 the greatest variability and shares only 21% identity. Within the C2 domains, there is 100%

151 conservation of the negatively charged Ca²⁺ binding residues in the C2 loops. A polybasic stretch
152 in the C2B domain that mediates Ca²⁺-independent PI(4,5)P₂-lipid interactions is also conserved.
153 These sequence conservations indicate Ca²⁺-dependent and Ca²⁺-independent membrane binding
154 are key properties of both SYT proteins.

155 Beyond lipid binding, SYT1's interaction with the SNARE complex is essential for its ability
156 to activate SV fusion. Five key C2B residues (S332, R334, E348, Y391, A455) form the primary
157 interaction site that docks SYT1 onto the SNARE complex (Guan et al., 2017; Zhou et al., 2015).
158 Four of the five primary SNARE binding residues are not conserved in *Drosophila* SYT7 (Figure
159 1C, Figure 1 – figure supplement 1). In addition, *Drosophila* and mammalian SYT7 contain
160 specific amino acids substitutions at two of these residues that block SNARE binding and abolish
161 SYT1 function in SV fusion (Guan et al., 2017), including C285 (corresponding to *Syt1* mutant
162 R334C) and K299 (corresponding to *Syt1* mutant E348K). A secondary SNARE complex-binding
163 interface on SYT1 is mediated by conserved basic residues at the bottom on the C2B β-barrel
164 (R451/R452 in *Drosophila*; R388/R389 in rodents) and is also not conserved in the SYT7
165 subfamily (Wang et al., 2016; Xue et al., 2010; Zhou et al., 2015). As such, SYT7 is unlikely to
166 engage the SNARE complex via the primary or secondary C2B interface, highlighting a key
167 difference in how the proteins regulate membrane trafficking. Beyond SNARE-binding, 20
168 nonsynonymous amino acid substitutions are conserved only in the SYT1 or SYT7 subfamilies,
169 suggesting additional interactions have likely diverged during evolution from the common
170 ancestral SYT protein. In summary, SYT1 and SYT7 are likely to regulate membrane trafficking
171 through distinct mechanisms, consistent with chimeric SYT1/SYT7 rescue experiments in
172 mammals (Xue et al., 2010).

173

174 **Generation of *Drosophila Syt7* mutations**

175 To assay SYT7 function in *Drosophila*, the CRISPR-Cas9 system was used to generate null
176 mutations in the *Syt7* locus. Using a guide RNA targeted near the *Syt7* start codon, several missense
177 mutations were obtained. To disrupt the coding frame of *Syt7*, a single base pair cytosine deletion
178 mutant (*Syt7^{M1}*) located seven amino acids downstream of the start codon was used for most of the
179 analysis, with an unaffected Cas9 injection line as control (Figure 1D). A Minos transposon
180 insertion in the second coding exon of *Syt7* was also identified from the BDGP gene disruption
181 project (Bellen et al., 2004) that generates a premature stop codon before the C2A domain,

182 providing a second independent allele (*Syt7^{M2}*) in a distinct genetic background (Figure 1D). To
183 characterize the effects of SYT7 overexpression, a UAS-*Syt7* transgene was crossed with the
184 neuronal *elav^{C155}*-GAL4 driver. Western analysis of adult brain extracts with anti-SYT7 antisera
185 confirmed the absence of SYT7 protein in *Syt7^{M1}* and *Syt7^{M2}* mutants and a 2.5-fold increase in
186 SYT7 protein levels in *elav^{C155}*-GAL4; UAS-*Syt7* (Figure 1E). Similar to the loss of SYT7 in mice
187 (Maximov et al., 2008), *Drosophila Syt7* null mutants are viable and fertile with no obvious
188 behavioral defects.

189

190 **Dosage-dependent regulation of neurotransmitter release by SYT7**

191 To assay SYT's role in synaptic transmission, two-electrode voltage clamp (TEVC) recordings
192 were performed at glutamatergic NMJs from 3rd instar larval motor neurons at segment A3 muscle
193 6 in 2 mM extracellular Ca²⁺. No significant changes in spontaneous release parameters were
194 identified, as miniature excitatory junctional current (mEJC) amplitude, kinetics and frequency
195 were similar between *Syt7^{M1}* mutants, *Syt7^{M1}* heterozygotes (*Syt7^{M1/+}*) and controls (Figure 2A-
196 D). In contrast to spontaneous release, evoked SV fusion (excitatory evoked junctional current
197 (eEJC)) was dramatically enhanced in *Syt7^{M1}* single mutants and elevated to an intermediate level
198 in *Syt7^{M1}* heterozygotes (Figure 2E, F; control: 158.33 ± 19.13 nA, n=9; *Syt7^{M1/+}*: p<0.05, 233.08
199 ± 19.16 nA, n=14; *Syt7^{M1}*: p<0.005, 262.96 ± 13.01 nA, n=10). Although evoked release was
200 increased ~2-fold, there was no change in eEJC kinetics in *Syt7^{M1}* or *Syt7^{M1/+}* (Figure 2G, H). Both
201 eEJC rise time and eEJC half-width were unaffected (Figure 2I, J). Loss of SYT7 increased evoked
202 release regardless of whether quantal content was estimated using eEJC amplitude (which
203 primarily measures synchronous release, 98% increase, Figure 2K) or eEJC charge (which
204 measures both synchronous and asynchronous release, 128% increase, Figure 2L). We conclude
205 loss of SYT7 enhances SV fusion with no major effect on release kinetics at *Drosophila* NMJs.

206 The synaptic levels of SYT7 are likely to be rate-limiting for its ability to regulate synaptic
207 transmission since *Syt7^{M1/+}* heterozygotes displayed an intermediate increase in evoked release
208 compared to *Syt7^{M1}* null mutants. To determine if the effects of SYT7 are dosage-sensitive, SYT7
209 was overexpressed 2.5-fold by driving a UAS-*Syt7* transgene with neuronal *elav^{C155}*-GAL4 (Figure
210 1E). Overexpression of SYT7 had no significant effect on spontaneous mEJC kinetics or amplitude
211 (Figure 3A, B), similar to the lack of effect in *Syt7* null mutants. However, SYT7 overexpression
212 resulted in a ~2-fold decrease in mEJC frequency (Figure 2C, p<0.05), suggesting elevated levels

213 of SYT7 can reduce spontaneous fusion. Unlike the increased evoked release in *Syt7^{MI}* and
214 *Syt7^{MI/+}* mutants, SYT7 overexpression caused a striking reduction in eEJC amplitude (Figure
215 3D, E) and eEJC charge (Figure 3F), with only mild effects on SV release kinetics (Figure 3G).
216 To determine if the inhibitory action of SYT7 on SV release is secondary to a presynaptic role,
217 SYT7 was overexpressed postsynaptically using the muscle specific *Mhc*-GAL4 driver.
218 Overexpression of SYT7 in muscles had no effect on eEJC amplitude or kinetics (Figure 3 –
219 supplemental figure 1A, B). We conclude that increased presynaptic SYT7 levels reduce both
220 spontaneous and evoked SV fusion, indicating SYT7 functions as a negative regulator of
221 neurotransmitter release.

222

223 **Analysis of synaptic structure and AZ morphology in *Syt7* mutants**

224 To determine if enhanced SV fusion in the absence of SYT7 results from an increase in AZ
225 number or SV docking, synaptic morphology and ultrastructure at the NMJ was analyzed in *Syt7^{MI}*
226 mutants. Motor neurons form en passant synaptic boutons along the axon that contain hundreds of
227 individual AZs marked by a central filamentous T-bar composed of the ELKS/CAST homolog
228 Bruchpilot (BRP) (Ehmann et al., 2014; Wagh et al., 2006). Immunostaining for BRP, the SV-
229 associated protein Complexin (CPX) and a general marker for neuronal membranes (anti-HRP)
230 was performed at muscle 6/7 and muscle 4, the two NMJs analyzed in this study (Figure 4A-H).
231 There was no change in the total number of synaptic boutons (Figure 4C, F), AZ number defined
232 by BRP puncta (Figure 4D, G), or AZ number per muscle surface area (Figure 4E, H). To examine
233 the AZ T-bar where SVs cluster, high-resolution structured illumination microscopy (SIM) was
234 performed on larval muscle 4 NMJs following anti-BRP immunostaining. *Syt7^{MI}* mutants
235 displayed the normal BRP ring architecture and showed no major difference in morphology
236 compared to controls (Figure 4I). Individual T-bar size and intra-terminal T-bar spacing was
237 quantified in controls and *Syt7^{MI}* mutants on a Zeiss Airyscan confocal. Although BRP ring
238 structure was intact, *Syt7^{MI}* mutants displayed a 25% decrease in the average volume of individual
239 BRP-labeled T-bars (Figure 4J), but no change in the spacing of T-bars relative to each other
240 (Figure 4K). We conclude that loss of SYT7 does not disrupt overall AZ morphology or AZ
241 number, though *Syt7^{MI}* mutants display a mild decrease in T-bar volume.

242 To determine if enhanced SV docking could increase the number of SVs available for release
243 in *Syt7* mutants, SV distribution was quantified at larval muscle 6/7 NMJs in control and *Syt7^{MI}*

244 using transmission electron microscopy (TEM, Figure 5A). No change in overall SV density was
245 observed within *Syt7^{MI}* boutons, indicating SV recycling is largely unperturbed (Figure 5B). In
246 contrast to the mild decrease in T-bar area (Figure 4J), there was no change in the length of
247 individual AZs defined by the electron dense synaptic cleft (Figure 5C, $p=0.93$; control: $404 \pm$
248 34.5 nm, $n=21$ AZs from 5 larvae; *Syt7^{MI}*: 409 ± 28.9 nm, $n=29$ AZs from 5 larvae). To examine
249 docking, SVs in contact with the plasma membrane under the T-bar (within 100 nm, Figure 5D)
250 or just outside the T-bar (100 to 400 nm, Figure 5E) were quantified. No significant change in the
251 number of SVs docked at the AZ plasma membrane was detected (Fig 5D-F), indicating
252 morphological docking defined by EM is not altered in *Syt7^{MI}* mutants. To quantify SV distribution
253 in the cytoplasm around AZs, SV number was binned into four concentric hemi-circles from 100
254 to 400 nm radius centered on the T-bar. No significant difference in SV distribution was observed
255 in any bin (Figure 5G, H), indicating the morphological distribution of SVs around T-bars is intact
256 in the absence of SYT7. We conclude the enhanced release in *Syt7^{MI}* mutants is not due to
257 increased AZ number or docked SVs.

258

259 **Optical quantal mapping in *Syt7* mutants**

260 Given quantal size (Figure 2B), AZ number (Figure 4D, G) and SV docking (Figure 5H) are
261 unchanged in *Syt7* mutants, increased release probability (P_r) at individual AZs is a candidate
262 mechanism to mediate the elevated quantal content during single stimuli. We previously developed
263 a quantal imaging approach to map AZ P_r at Drosophila NMJs by expressing myristoylated
264 GCaMP6s in muscles (Akbergenova et al., 2018; Melom et al., 2013). Using this approach, P_r
265 maps for evoked release were generated for all AZs from 1b boutons at muscle 4 NMJs in control
266 and *Syt7^{MI}* mutants. Similar to controls, AZs formed by single motor neurons in *Syt7^{MI}* displayed
267 heterogeneous P_r (Figure 6A). However, P_r distribution was strikingly different between the
268 genotypes, with a greater number of high P_r and fewer low P_r AZs at *Syt7^{MI}* NMJs (Figure 6B).
269 *Syt7^{MI}* NMJs also had fewer silent AZs that showed no release (control: 19.9%; *Syt7^{MI}*: 4.6%).
270 Overall, mean P_r was increased 2-fold (Figure 6C, $p<0.01$; control: 0.063 ± 0.002 , $n=1158$ AZs;
271 *Syt7^{MI}*: 0.12 ± 0.004 , $n=768$ AZs). In contrast, the maximum AZ P_r in the two genotypes was
272 unchanged (Figure 6C, control: 0.61; *Syt7^{MI}*: 0.63), indicating an upper limit on release strength
273 for single AZs that is similar between controls and *Syt7^{MI}*. We conclude that the enhanced release
274 in the absence of SYT7 results from an increase in average P_r across the AZ population.

275

276 **Loss of SYT7 enhances SV release in *Syt1* null mutants**

277 *Drosophila Syt1* null mutants have dramatically reduced synchronous SV fusion and enhanced
278 asynchronous and spontaneous release (Jorquera et al., 2012; Lee et al., 2013; Yoshihara et al.,
279 2010; Yoshihara and Littleton, 2002). We generated *Syt1; Syt7* double mutants to determine if
280 SYT7 mediates the residual asynchronous release present in *Syt1* nulls. A complete loss of
281 asynchronous release in *Syt1; Syt7* double mutants should occur if SYT7 functions as the sole
282 asynchronous Ca²⁺ sensor, while a reduction in release is expected if it is one of several sensors
283 mediating the residual synaptic transmission in *Syt1*. Animals lacking SYT1 were obtained by
284 crossing an intragenic *Syt1* deletion (*Syt1^{N13}*) with a point mutant containing an early stop codon
285 (*Syt1^{AD4}*), an allelic combination referred to as *Syt1^{Null}*. Loss of SYT1 results in lethality throughout
286 development, although some *Syt1^{Null}* mutants survive to adulthood when cultured under special
287 conditions (Loewen et al., 2001). Surviving *Syt1^{Null}* adults are severely uncoordinated and die
288 within several days. Quantification of survival rates demonstrated 45.3% of *Syt1^{Null}* mutants
289 survived from the 1st instar to the pupal stage, with 44.1% of mutant pupae surviving to adulthood
290 (n=5 groups with >40 starting animals each). In contrast, 5.6% of *Syt1^{Null}; Syt7^{M2}* double mutants
291 (referred to as *Double^{Null}*) survived from the 1st instar to the pupal stage, and 6.6% of mutant pupae
292 survived to adulthood (n=6 groups with >80 animals each). Western analysis confirmed loss of
293 both proteins in *Double^{Null}* mutants and demonstrated no change in expression of SYT1 or SYT7
294 in the absence of the other family member in individual null mutant backgrounds (Figure 7A).
295 Although loss of both SYTs caused synergistic defects in survival, residual synaptic transmission
296 must exist given some *Double^{Null}* mutants survive.

297 To assay synaptic transmission, recordings were performed from 3rd instar larval muscle 6 in
298 2 mM extracellular Ca²⁺ in *Syt1^{Null}* and *Double^{Null}* mutants. No change in spontaneous mEJC
299 amplitude or kinetics was found between the two genotypes (Figure 7B), indicating postsynaptic
300 sensitivity, neurotransmitter loading, and fusion pore dynamics were not disrupted by loss of
301 SYT7. However, a ~2-fold increase in mEJC frequency was observed in the *Double^{Null}* compared
302 to *Syt1^{Null}* (Figure 7C, p<0.001; *Syt1^{Null}*: 2.99 ± 0.23 Hz, n=16; *Double^{Null}*: 5.33 ± 0.42 Hz, n=14),
303 demonstrating loss of both SYTs enhances the already elevated spontaneous release rate found in
304 *Syt1^{Null}* mutants alone. Measurements of evoked release revealed both amplitude and charge
305 transfer were increased ~2-fold in *Double^{Null}* compared to *Syt1^{Null}* mutants (Figure 7D-F; eEJC

306 amplitude: $p < 0.001$; *Syt1^{Null}*: 3.18 ± 0.4 nA, $n=15$; *Double^{Null}*: 6.12 ± 0.62 nA, $n=13$; eEJC charge:
307 $p < 0.05$; *Syt1^{Null}*: 33.2 ± 4.4 nA*ms, $n=15$; *Double^{Null}*: 52.6 ± 5.8 nA*ms, $n=13$). In addition, more
308 SVs fused in the first 15 ms following stimulation (Figure 7G, H), with less SVs available for
309 release later in the response. *Double^{Null}* mutants also had a reduced rate of evoked failures
310 following nerve stimulation compared to *Syt1^{Null}*, consistent with an increased probability of SV
311 fusion (Figure 7I, $p < 0.01$; *Syt1^{Null}*: $21.1 \pm 3.5\%$ failure rate, $n=17$; *Double^{Null}*: $7.4 \pm 3.4\%$ failure
312 rate, $n=14$). These results indicate SYT7 does not mediate the residual release found in the absence
313 of SYT1. We conclude SYT7 negatively regulates SV fusion with or without SYT1 present at the
314 synapse.

315

316 **Short-term facilitation does not require SYT7**

317 Although these results indicate SYT7 is not a key asynchronous Ca^{2+} sensor in *Drosophila*,
318 the protein has also been implicated as the Ca^{2+} sensor for facilitation (Chen et al., 2017; Jackman
319 et al., 2016; Turecek and Regehr, 2018), a short-term form of presynaptic plasticity that results in
320 enhanced SV fusion during closely-spaced stimuli. To examine facilitation, $[\text{Ca}^{2+}]$ was lowered
321 from 2 mM to 0.175 mM or 0.2 mM to identify conditions where the initial P_r was matched
322 between control and *Syt7* mutants. In 0.175 mM Ca^{2+} , controls displayed an 11% failure ratio in
323 response to single action potentials, while *Syt7^{MI}* had no failures (Figure 8A). In 0.2 mM Ca^{2+} ,
324 neither genotype had failures (Figure 8A), although evoked release was increased 3-fold in *Syt7^{MI}*
325 (Figure 7B, C, $p < 0.01$, control: 7.73 ± 1.5 nA, $n=9$; *Syt7^{MI}*: 23.72 ± 6.2 nA, $n=9$). In contrast, EJC
326 amplitude was not statistically different between control in 0.2 mM Ca^{2+} (7.73 ± 1.5 nA, $n=9$) and
327 *Syt7^{MI}* in 0.175 mM Ca^{2+} (8.70 ± 1.6 nA, $n=9$). Facilitation was assayed in these conditions where
328 initial P_r was comparable. Control and *Syt7^{MI}* mutants displayed robust facilitation to paired-pulses
329 separated by 10 or 50 ms at both Ca^{2+} concentrations (Figure 8D). A modest reduction in paired-
330 pulse ratio was observed in *Syt7^{MI}* at 0.175 Ca^{2+} compared to control at 0.2 mM Ca^{2+} (Figure 8E,
331 F, $p < 0.05$; 10 ms interval: 31% decrease; 50 ms interval: 22% decrease). These data indicate SYT7
332 is not the sole effector of facilitation. The mild defect in *Syt7* mutants could be due to a partially
333 redundant role for SYT7 in facilitation or secondary to differences in Ca^{2+} available to activate the
334 true facilitation sensor. Given $[\text{Ca}^{2+}]$ was lowered in *Syt7^{MI}* to match initial P_r between the
335 genotypes, the latter explanation is more likely.

336 To determine if short-term facilitation could be elicited in the absence of both SYT1 and SYT7,
337 a 10 Hz stimulation train in 2.0 mM Ca^{2+} was given to *Double^{Null}* mutants and eEJC responses
338 were compared to *Syt1^{Null}* mutants alone. Similar to the increased quantal content to single action
339 potentials, *Double^{Null}* mutants displayed larger facilitating responses during the early phase of
340 stimulation (Figure 8G-I; cumulative average release for 10 stimuli: *Syt1^{Null}* (n=12): 87 ± 7.0
341 quanta; *Double^{Null}* (n=13): 109 ± 9.9 quanta; 20 stimuli: *Syt1^{Null}*: 209 ± 13.8 quanta; *Double^{Null}*:
342 261 ± 22.6 quanta; 50 stimuli: *Syt1^{Null}*: 594 ± 34.5 quanta; *Double^{Null}*: 745 ± 56.2 quanta, $p < 0.03$).
343 These results indicate short-term facilitation can occur in the absence of both SYT1 and SYT7,
344 and is enhanced during the early phases of stimulation, consistent with SYT7 negatively regulating
345 SV fusion with or without SYT1.

346

347 ***Syt7* mutants have access to a larger pool of fusogenic SVs but maintain a normal SV** 348 **endocytosis rate at steady-state**

349 Enhanced SV release in *Syt7* mutants could reflect increased fusogenicity of the entire SV
350 population or conversion of a non-fusogenic SV pool into one capable of fusion in the absence of
351 SYT7. To test whether SYT7 normally renders a pool of SVs non-fusogenic, 1000 stimuli at 10
352 Hz were applied in 2 mM Ca^{2+} at 3rd instar muscle 6 NMJs to deplete the readily releasable pool
353 (RRP) and drive SV cycling to steady-state. The total number of released SVs and the SV recycling
354 rate was then measured. Both control and *Syt7^{MI}* eEJCs depressed during the stimulation train.
355 However, SV release in *Syt7^{MI}* mutants remained elevated over much of the initial stimulation
356 (Figure 9A) and the integral of release during the train was greater than controls (Figure 9B),
357 indicating *Syt7* nulls have access to more fusogenic SVs. SV release rate in *Syt7^{MI}* eventually
358 reached the same level as control following depletion of the RRP (Figure 9C, control quantal
359 content: 131.5 ± 10.7 , n=7; *Syt7^{MI}* quantal content: 123.1 ± 10.5 , n=8). We conclude that SV
360 endocytosis and recycling rate is SYT7-independent at steady-state, although *Syt7^{MI}* mutants
361 contain a larger RRP available for fusion.

362 To further examine SV recycling, FM1-43 dye uptake and release assays were performed in
363 control and *Syt7^{MI}* mutants at 3rd instar muscle 6/7 NMJs. At low stimulation rates (0.5 Hz), *Syt7^{MI}*
364 mutants took up significantly more FM1-43 dye than controls (Figure 9D, F), consistent with the
365 increased SV fusion observed by physiology. In contrast, no significant difference in FM1-43
366 uptake was found following high frequency 10 Hz stimulation for 500 stimuli (Figure 9E, G).

367 These data suggest previously exocytosed SVs re-enter the RRP more often in the absence of SYT7
368 given the normal recycling rate (Figure 9C). Consistent with this hypothesis, no change in FM1-
369 43 release was detected with high [K⁺] stimulation following 10 Hz loading (Figure 9H). Together
370 with the electrophysiology data, we conclude *Syt7* mutants have a larger RRP, but no changes in
371 SV endocytosis.

372

373 ***Syt7* mutants have enhanced refilling of the readily-releasable SV pool independent of** 374 **endocytosis**

375 To probe how SYT7 regulates SV cycling and the transition between distinct SV pools, eEJC
376 recovery kinetics following high frequency stimulation were characterized. A paradigm consisting
377 of 30 stimuli at 0.5 Hz, 500 stimuli at 10 Hz and a final 50 stimuli at 0.5 Hz was given to *Syt7^{M1}*
378 mutants, *Syt7^{M1/+}* heterozygotes and controls in 2 mM Ca²⁺ (Figure 10A). During 0.5 Hz
379 stimulation, *Syt7^{M1}* and *Syt7^{M1/+}* displayed elevated levels of release. Following the onset of high
380 frequency stimulation, *Syt7^{M1}* and *Syt7^{M1/+}* synapses depressed while controls displayed a mild
381 facilitation before quickly transitioning to depression (Figure 10B). Remarkably, *Syt7^{M1}* and
382 *Syt7^{M1/+}* displayed an extremely rapid recovery of eEJC amplitude and quantal content during the
383 2 second interval following termination of the 10 Hz train compared to controls (Figure 10C). A
384 similar rapid recovery was observed in *Syt7^{M1}* after 2000 stimuli were given at 10 Hz to fully
385 deplete the RRP and normalize release rates to control levels (Figure 10 – figure supplement 1A-
386 C). These observations suggest SYT7 functions to reduce SV entry into the RRP, while also
387 negatively regulating fusion of newly regenerated SVs. The enhanced refilling of the RRP did not
388 require SYT1 function, as *Double^{Null}* mutants also displayed larger eEJCs than *Syt1^{Null}* alone during
389 the recovery from a 10 Hz stimulation train (Fig. 8G).

390 The partial elevation in RRP refilling rate at *Syt7^{M1/+}* synapses indicates the amount of SYT7
391 in the presynaptic terminal regulates SV entry into the releasable pool. To determine if RRP
392 refilling is dosage-sensitive, the stimulation paradigm above (0.5 Hz/10 Hz/0.5 Hz) was applied
393 to SYT7 overexpression larvae (*elav^{C155}-GAL4; UAS-Syt7*) in 2 mM Ca²⁺. Presynaptic
394 overexpression of SYT7 had the opposite effect of *Syt7* mutants and *Syt7/+* heterozygotes, not only
395 reducing eEJC amplitude at 0.5 Hz, but greatly limiting the ability of SVs to re-enter the RRP
396 following termination of the 10 Hz stimulation train (Figure 10 – supplemental figure 2A-C). We

397 conclude that SYT7 limits release in a dosage-sensitive manner by negatively regulating the
398 number of SVs available for fusion and slowing recovery of the RRP following stimulation.

399 To determine if increased RRP refilling in *Syt7^{M1}* requires an enhanced rate of SV endocytosis
400 or is mediated through refilling from a pre-existing SV pool, recordings were repeated in the
401 presence of the proton pump inhibitor bafilomycin. Bafilomycin blocks neurotransmitter reloading
402 of newly endocytosed SVs and should eliminate the enhanced refilling of the RRP if recycling is
403 essential. Alternatively, if SVs are recruited more rapidly from pre-existing pools, bafilomycin
404 would not abolish the enhanced recovery. The same 0.5 Hz/10 Hz/0.5 Hz paradigm was applied
405 in three successive epochs in the presence of 4 μ M bafilomycin or DMSO (control) in the bath
406 solution. As expected, bafilomycin progressively reduced eEJC amplitude throughout the
407 experiment and eliminated most evoked responses during the 3rd stimulation epoch (Figure 10D).
408 *Syt7^{M1}* mutants displayed a similar fold-enhancement in the recovery of the RRP in the presence
409 of bafilomycin, though the absolute numbers of SVs re-entering the pool decreased following the
410 2nd 10 Hz stimulation as the number of neurotransmitter-containing SVs declined (Figure 10E, F).
411 We conclude that the rapid refilling of the RRP can occur from pre-existing SV pools. In addition
412 to reducing fusogenicity of SVs already docked at the AZ, these data indicate SYT7 regulates
413 transition kinetics between vesicle pools by reducing the number of SVs moving from the reserve
414 pool to the RRP.

415

416 **SYT7 localizes to an internal membrane network within the peri-AZ that resides in** 417 **proximity to multiple presynaptic compartments**

418 Defining the subcellular localization of SYT7 could help elucidate how it modulates SV
419 dynamics. SYT7 could be a resident protein of the SV pool it regulates or reside on an alternative
420 compartment that exerts control over a subset of SVs. To examine the subcellular localization of
421 SYT7, an RFP tag was introduced at the 3'-end of the endogenous *Syt7* locus using CRISPR
422 (Figure 11A). This approach generated a SYT7^{RFP} C-terminal fusion protein expressed under its
423 endogenous enhancers to avoid any overexpression that might trigger changes in its normal
424 localization. A sfGFP version (SYT7^{GFP}) was also generated with CRISPR that showed the same
425 intra-terminal expression pattern as SYT7^{RFP} (Figure 11 – supplemental figure 1A). Western
426 analysis with anti-RFP identified a single band at the predicted molecular weight (73kD) of the
427 fusion protein in SYT7^{RFP} animals (Figure 11B), indicating a single SYT7 isoform is expressed in

428 *Drosophila*. Immunostaining of 3rd instar larvae with anti-RFP antisera revealed SYT7^{RFP} was
429 enriched in presynaptic terminals and formed an expansive tubular network near the plasma
430 membrane that extended into the center of the bouton (Figure 11C, D). Neuronal knockdown of
431 *Syt7* with two independent RNAi lines (*elav^{CI55}-GAL4*; UAS-*Syt7* RNAi) dramatically reduced
432 SYT7^{RFP} on Westerns (Figure 11B) and eliminated expression of SYT7^{RFP} at the NMJ (Figure 11
433 – supplemental figure 2), indicating the signal is specific to SYT7 and localizes predominantly to
434 the presynaptic compartment.

435 To further characterize the subsynaptic localization of SYT7, fluorescently-tagged
436 compartmental markers or compartment-specific antisera were used for labeling in the Syt7^{RFP}
437 background. Images were collected on a Zeiss Airyscan and analyzed in FIJI and Matlab to
438 generate cytofluorogram co-localization plots to calculate the Pearson correlation (r) between
439 SYT7^{RFP} and labeled compartments from individual synaptic boutons at muscle 6/7 NMJs (Figure
440 12, $n=3$ animals each). Co-labeling of the SV proteins nSYB and SYT1 served as a positive control
441 (Figure 12A, $r=0.71$). SYT7^{RFP} and the Golgi marker, Golgin84, served as a negative control since
442 Golgi is absent from presynaptic terminals (Figure 12L, $r=-0.43$). Co-localization analysis
443 indicates SYT7 resides on a membrane compartment that does not completely overlap with any
444 protein tested (Figure 12B-L). The largest overlap was with Dynamin (Figure 12B, $r=0.22$), a
445 GTPase involved in endocytosis that localizes to the peri-AZ. The t-SNARE SYX1 also
446 overlapped with a subset of SYT7 immunolabeling near the plasma membrane (Figure 12C,
447 $r=0.15$). Although SYT7's pattern of inter-connectivity within the bouton appeared similar to
448 peripheral ER, it did not co-localize with Reticulon-like 1 (RTLN1, Figure 12D, $r=0.01$), a
449 peripheral ER marker. In addition, SYT7 did not co-localize with SVs ($r=-0.07$), DCVs labeled
450 with ANF-GFP ($r=-0.19$), exosomes ($r=-0.29$), late endosomes ($r=-0.29$), lysosomes ($r=-0.01$) or
451 the plasma membrane (anti-HRP, $r=-0.06$). Neither SYT7^{RFP} (Figure 12G, $r=-0.11$) or SYT7^{GFP}
452 (Figure 11 – supplemental figure 1B) was enriched at AZs, but instead surrounded BRP as
453 previously described for other peri-AZ proteins. These data are in agreement with anti-SYT7
454 antibody labeling of sucrose gradient-separated subcellular fractions from wildtype *Drosophila*
455 head extracts that localized SYT7 to a distinct membrane compartment separate from SVs and the
456 plasma membrane (Adolfson et al., 2004). In conclusion, SYT7 surrounds AZs marked by BRP
457 (Figure 11 – supplemental figure 1B, Figure 12G), indicating the protein localizes in part to the
458 previously described peri-AZ domain. Peri-AZs are enriched in proteins regulating SV endocytosis

459 and endosomal trafficking (Coyle et al., 2004; Koh et al., 2004; Marie et al., 2004; Rodal et al.,
460 2008; Sone et al., 2000), indicating SYT7 may modulate SV re-entry into the RRP by interfacing
461 with sorting machinery within this domain.

462 SYT7 localization was widespread within the peri-AZ region, with SYT7^{RFP} tubules in close
463 proximity to other labeled membrane compartments, including endosomes, lysosomes, and the
464 plasma membrane (Figure 12 – figure supplement 1). To determine if the SYT7 compartment
465 required endosomal trafficking for its assembly or maintenance, a panel of dominant-negative,
466 constitutively-active or wildtype endosomal UAS-RAB proteins (Zhang et al., 2007) were
467 expressed with *elav*^{C155}-GAL4 in the SYT7^{RFP} background. Manipulations of RAB5 (early
468 endosomes), RAB7 (late endosomes) or RAB4 and RAB11 (recycling endosomes) did not disrupt
469 the abundance or morphology of the SYT7 tubular network (Figure 12 – supplemental figure 2).
470 Similarly, no change in the distribution of several compartment markers were found in *Syt7^{MI}*
471 mutants, including the early endosomal marker RAB5, the late endosomal/peri-AZ marker RAB11
472 and the peri-AZ protein Nervous Wreck (NWK) (Figure 12 – supplemental figure 3). In addition,
473 no defect was observed in trans-synaptic transfer of the exosomal protein SYT4 to the postsynaptic
474 compartment, indicating SYT7 does not regulate exosome trafficking as described for several other
475 peri-AZ proteins (Walsh et al., 2019). Although no sub-compartment overlapped completely with
476 SYT7, the protein is positioned within the peri-AZ to interact with SVs, endosomes and the
477 recycling machinery to negatively regulate the size of releasable SV pools (Figure 12 –
478 supplemental figure 4). We conclude that SYT7 does not localize to SVs and is not enriched at
479 AZs, consistent with SYT7 negatively regulating SV release through an indirect mechanism that
480 does not require its presence at sites of SV fusion.

481 Discussion

482 To characterize the location and function of SYT7 in *Drosophila*, we used the CRISPR-Cas9
483 system to endogenously label the protein and generate null mutations in the *Syt7* locus. Our
484 findings indicate SYT7 acts as a negative regulator of SV release, AZ P_r , RRP size, and RRP
485 refilling. The elevated P_r across the AZ population in *Syt7* mutants provides a robust explanation
486 for why minor defects in asynchronous release and facilitation are present in *Drosophila*. SYT7's
487 presence on an internal tubular membrane network within the peri-AZ positions the protein to
488 interface with the SV cycle at multiple points to regulate membrane trafficking. In addition, the
489 increased SV fusion in animals lacking both SYT1 and SYT7 indicate the full complement of Ca^{2+}
490 sensors that mediate the distinct phases of SV fusion remain unknown.

491 492 *Syt7* mutants have increased P_r at *Drosophila* NMJs

493 Using a combination of synaptic physiology and imaging approaches, our findings indicate
494 SYT7 acts to reduce SV recruitment and fusion. Minor defects in asynchronous release and
495 facilitation were identified in *Drosophila Syt7* mutants, as observed in mouse and zebrafish models
496 (Bacaj et al., 2013; Chen et al., 2017; Jackman et al., 2016; Turecek and Regehr, 2019, 2018;
497 Weber et al., 2014; Wen et al., 2010). However, we attribute these mild defects to reduced SV
498 availability as a result of increased P_r in *Syt7* mutants. Indeed, a key feature of facilitation is its
499 critical dependence on initial P_r (Neher and Brose, 2018; Zucker and Regehr, 2002). Low P_r
500 synapses increase SV fusogenicity as Ca^{2+} levels rise during paired-pulses or stimulation trains,
501 resulting in short-term increases in P_r for SVs not recruited during the initial stimuli. In contrast,
502 depression occurs at high P_r synapses due to the rapid depletion of fusion-capable SVs during the
503 initial response. Prior quantal imaging at *Drosophila* NMJs demonstrated facilitation and
504 depression can occur across different AZs within the same neuron, with high P_r AZs depressing
505 and low P_r AZs facilitating (Peled and Isacoff, 2011). Given the elevated P_r in *Syt7* mutants, the
506 facilitation defects are likely related to differences in initial P_r and depletion of fusion-competent
507 SVs available for release during the 2nd stimuli.

508 A similar loss of SVs due to elevated P_r in *Syt7* mutants would reduce fusogenic SVs that are
509 available during the delayed phase of the asynchronous response. *Syt1; Syt7* double mutants
510 continue to show asynchronous fusion and facilitation, conclusively demonstrating there must be
511 other Ca^{2+} sensors that mediate these components of SV release. The predominant localization of

512 endogenous SYT7 to an internal tubular membrane compartment at the peri-AZ also places the
513 majority of the protein away from release sites where it would need to reside to directly activate
514 SV fusion. As such, our data indicate SYT7 regulates SV release through a distinct mechanism
515 from SYT1.

516 We can also conclude that the remaining components of asynchronous fusion and facilitation
517 must be mediated by an entirely different family of Ca²⁺-binding proteins than Synaptotagmins (or
518 through Ca²⁺-lipid interactions). Of the seven *Syt* genes in the Drosophila genome, only 3 SYT
519 proteins are expressed at the motor neuron synapses assayed in our study – SYT1, SYT4 and SYT7
520 (Adolfson et al., 2004). For the remaining SYTs in the genome, SYT- α and SYT- β are expressed
521 in neurosecretory neurons and function in DCV fusion (Adolfson et al., 2004; Park et al., 2014).
522 SYT12 and SYT14 lack Ca²⁺ binding residues in their C2 domains and are not expressed in motor
523 neurons (Adolfson et al., 2004). In addition, SYT4 is found on exosomes and transferred to
524 postsynaptic cells, where it participates in retrograde signaling (Adolfson et al., 2004; Harris et al.,
525 2016; Korkut et al., 2013; Walsh et al., 2019; Yoshihara et al., 2005). *Syt1*; *Syt4* double mutants
526 display the same SV fusion defects found in *Syt1* mutants alone, indicating SYT4 cannot
527 compensate for SYT1 function in SV release (Barber et al., 2009; Saraswati et al., 2007). As such,
528 SYT1 and SYT7 are the only remaining SYT isoforms that could contribute to SV trafficking
529 within Drosophila motor neuron terminals.

530 A prior study from our lab using *Syt7* RNAi also found no change in facilitation or
531 asynchronous release following knockdown of SYT7 (Saraswati et al., 2007). However, the RNAi
532 knockdown did not result in enhanced release. Although a reduction in ectopic expression of SYT7
533 in muscles could be seen with *Mhc*-GAL4 driving UAS-*Syt7* RNAi, our anti-SYT7 antisera could
534 not recognize the endogenous protein in neurons by immunocytochemistry, preventing a
535 determination of presynaptic SYT7 levels following neuronal RNAi. Based on the current data,
536 the *Syt7* UAS-RNAi line was likely ineffective in knocking down endogenous SYT7 in neurons.
537 Both *Syt7*^{M1} and *Syt7*^{M2} alleles result in early stop codons and lack SYT7 expression by Western
538 analysis. Given both null mutants show elevated release, and SYT7 overexpression reduces
539 release, our data indicate SYT7 normally acts to suppress SV fusogenicity as demonstrated by both
540 electrophysiology and optical *P_r* imaging.

541

542 *SYT7 regulates the recruitment and fusion of SVs in a dosage-dependent manner*

543 Although our data indicate SYT7 is not the primary asynchronous or facilitation Ca^{2+} sensor
544 in *Drosophila*, we found it inhibits SV fusion in a dosage-sensitive manner. This is not due to
545 altered endocytosis, as *Syt7* mutants have a normal steady-state rate of SV release following
546 depletion of the RRP. Instead, SYT7 regulates SV fusogenicity at a stage between SV endocytosis
547 and fusion. Given the rapid enhanced refilling of the RRP observed in *Syt7* mutants, and the
548 suppression of RRP refilling following SYT7 overexpression, our data indicate SYT7 regulates
549 releasable SVs in part through changes in SV mobilization to the RRP. Ca^{2+} is well known to
550 control the replenishment rate of releasable SVs, with Calmodulin-UNC13 identified as one of
551 several molecular pathways that accelerate RRP refilling in a Ca^{2+} -dependent manner (Dittman et
552 al., 2000; Dittman and Regehr, 1998; Junge et al., 2004; Lipstein et al., 2013; Ritzau-Jost et al.,
553 2018). Our findings indicate SYT7 acts in an opposite fashion and slows RRP refilling, providing
554 a Ca^{2+} -dependent counter-balance for SV recruitment into the RRP. Although such an effect has
555 not been described for mammalian SYT7, defects in RRP replenishment have been observed when
556 both SYT1 and SYT7 are deleted or following high frequency stimulation trains (Bacaj et al.,
557 2015; Durán et al., 2018; Liu et al., 2014).

558 SYT7's role in restricting SV fusion and RRP size also affects spontaneous release. Although
559 *Syt7* mutants alone do not show elevated mini frequency, *Double^{Null}* mutants have a 2-fold increase
560 in spontaneous release. Similar increases in spontaneous release were observed at mammalian
561 synapses lacking both SYT7 and SYT1 (or SYT2), with the effect being attributed to a dual role
562 in clamping fusion in the absence of Ca^{2+} (Luo and Südhof, 2017; Turecek and Regehr, 2019). Our
563 results indicate the elevation in spontaneous release at *Drosophila* synapses is a result of an
564 increase in releasable SVs rather than a clamping function for SYT7. Following overexpression of
565 SYT7, there is a reduction in the number of fusogenic SVs available for both evoked and
566 spontaneous release. The dosage-sensitivity of the various phenotypes indicate SYT7 abundance
567 is a critical node in controlling SV release rate. Indeed, mammalian SYT7 levels are post-
568 transcriptionally modulated by γ -secretase proteolytic activity and APP, linking it to SV trafficking
569 defects in Alzheimer's disease (Barthet et al., 2018).

570

571 *How does SYT7 negatively regulate recruitment and fusion of SVs?*

572 The precise mechanism by which SYT7 reduces release and slows refilling of the RRP is
573 uncertain given it is not enriched at sites of SV fusion. Although we cannot rule out the possibility

574 that a small fraction of the protein is found at AZs, SYT7 is predominantly localized to an internal
575 membrane compartment at the peri-AZ where SV endocytosis and endosomal sorting occurs
576 (Coyle et al., 2004; Koh et al., 2004; Marie et al., 2004; Rodal et al., 2008; Sone et al., 2000).
577 SYT7 membrane tubules are in close proximity and could potentially interact with peri-AZs
578 proteins, endosomes, lysosomes and the plasma membrane. Given its primary biochemical activity
579 is to bind membranes in a Ca²⁺-dependent manner, SYT7 could mediate cargo or lipid movement
580 across multiple compartments within peri-AZs. In addition, it is possible SYT7 tubules could form
581 part of the poorly defined SV recycling endosome compartment. However, we observed no change
582 in SV density or SV localization around AZs, making it unlikely SYT7 would be essential for
583 endosomal trafficking of SVs. The best characterized regulator of the SV endosome compartment
584 in *Drosophila* is the RAB35 GAP Skywalker (SKY) (Uytterhoeven et al., 2011). Although *Sky*
585 mutations display some similarities to *Syt7*, including increased neurotransmitter release and larger
586 RRP size, *Syt7* lacks most of the well-described *Sky* phenotypes such as behavioral paralysis, FM1-
587 43 uptake into discrete punctated compartments, cisternal accumulation within terminals and
588 reduced SV density. In addition, we found no co-localization between SKY-GFP and SYT7^{RFP}
589 within presynaptic terminals.

590 By blocking SV refilling with bafilomycin, our findings indicate the fast recovery of the RRP
591 can occur via enhanced recruitment from the reserve pool and does not require changes in
592 endocytosis rate. The phosphoprotein Synapsin has been found to maintain the reserve SV pool by
593 tethering vesicles to actin filaments at rest (Akbergenova and Bykhovskaia, 2007; Bykhovskaia,
594 2011; Hilfiker et al., 1999; Milovanovic and De Camilli, 2017; Shupliakov et al., 2011). Synapsin
595 interacts with the peri-AZ protein Dap160/Intersectin to form a protein network within the peri-
596 AZ that regulates clustering and release of SVs (Gerth et al., 2017; Marie et al., 2004; Winther et
597 al., 2015). Synapsin-mediated phase separation is also implicated in clustering SVs near release
598 sites (Milovanovic et al., 2018; Milovanovic and De Camilli, 2017). SYT7 could similarly
599 maintain a subset of SVs in a non-releasable pool and provide a dual mechanism for modulating
600 SV mobilization. Phosphorylation of Synapsin and Ca²⁺ activation of SYT7 would allow multiple
601 activity-dependent signals to regulate SV entry into the RRP. As such, SYT7 could play a key role
602 in organizing membrane trafficking and protein interactions within the peri-AZ network by adding
603 a Ca²⁺-dependent regulator of SV recruitment and fusogenicity.

604 Additional support for a role for SYT7 in regulating SV availability through differential SV
605 sorting comes from recent studies on the SNARE complex binding protein CPX. Analysis of
606 *Drosophila Cpx* mutants, which have a dramatic increase in minis (Buhl et al., 2013; Huntwork
607 and Littleton, 2007; Jorquera et al., 2012), revealed a segregation of recycling pathways for SVs
608 undergoing spontaneous versus evoked fusion (Sabeva et al., 2017). Under conditions where
609 intracellular Ca^{2+} is low and SYT7 is not activated, spontaneously-released SVs do not transit to
610 the reserve pool and rapidly return to the AZ for re-release. In contrast, SVs released during high
611 frequency evoked stimulation when Ca^{2+} is elevated and SYT7 is engaged, re-enter the RRP at a
612 much slower rate. This mechanism slows re-entry of SVs back into the releasable pool when
613 stimulation rates are high and large numbers of SV proteins are deposited onto the plasma
614 membrane at the same time, allowing time for endosomal sorting that might be required in these
615 conditions. In contrast, SVs released during spontaneous fusion or at low stimulation rates would
616 likely have less need for endosomal re-sorting. Given SYT7 restricts SV transit into the RRP, it
617 provides an activity-regulated Ca^{2+} -triggered switch for redirecting and retaining SVs in a non-
618 fusogenic pool that could facilitate sorting mechanisms.

619 Beyond SV fusion, presynaptic membrane trafficking is required for multiple signaling
620 pathways important for developmental maturation of NMJs (Harris and Littleton, 2015; McCabe
621 et al., 2003; Packard et al., 2002; Piccioli and Littleton, 2014; Rodal et al., 2011). In addition,
622 alterations in neuronal activity or SV endocytosis can result in synaptic undergrowth or overgrowth
623 (Akbergenova et al., 2018; Budnik et al., 1990; Dickman et al., 2006; Guan et al., 2005; Koh et
624 al., 2004). We did not find any defect in synaptic bouton or AZ number, indicating SYT7 does not
625 participate in membrane trafficking pathways that regulate synaptic growth and maturation.
626 However, a decrease in T-bar area in *Syt7* mutants was found. Although it is unclear how this
627 phenotype arises, it may represent a form of homeostatic plasticity downstream of elevated
628 synaptic transmission (Frank et al., 2020). There is also ample evidence that SV distance to Ca^{2+}
629 channels plays a key role in defining the kinetics of SV release and the size of the RRP (Böhme et
630 al., 2016; Chen et al., 2015; Neher, 2015; Neher and Brose, 2018; Wadel et al., 2007), suggesting
631 a change in such coupling in *Syt7* mutants might contribute to elevations in P_r and RRP refilling.
632 Further studies will be required to examine the role of this morphological alteration in release sites
633 in *Syt7* mutants.

634

635 **Materials and Methods**

636

637 *Drosophila stocks*

638 *Drosophila melanogaster* were cultured on standard medium at 22-25°C. Genotypes used in the
639 study include: *elav*^{C155}-GAL4 (Bloomington Drosophila Stock Center (BDSC)#8765), UAS-ANF-
640 Emerald (BDSC#7001), SYT4^{GFP-2M} (Harris et al., 2016), *Syt1*^{AD4} (DiAntonio and Schwarz, 1994),
641 *Syt1*^{N13} (Littleton et al., 1993b), UAS-*Syt7* (Saraswati et al., 2007), *Mhc*-GAL4 (BDSC#55132),
642 UAS-*Syt7* RNAi#1 (Vienna#24989) and UAS-*Syt7* RNAi#2 (BDSC#27279). Lines used for
643 testing co-localization with SYT7^{RFP} or mis-localization in *Syt7*^{M1} include: endogenous nSYB^{GFP}
644 (this study), UAS-NHE-GFP (this study), UAS-ANF-Emerald (BDSC#7001), SYT4^{GFP-2M} (Harris
645 et al., 2016), UAS-RTNL1-GFP (BDSC#77908), RAB5-YFP (BDSC#62543) and RAB11-YFP
646 (BDSC#62549). Lines used for assaying SYT7^{RFP} localization after overexpressing RABs: UAS-
647 RAB4-YFP (BDSC#9767), UAS-RAB4(Q67L)-YFP (BDSC#9770), UAS-RAB5-YFP
648 (BDSC#24616), UAS-RAB5(S43N)-YFP (BDSC#9772), UAS-RAB5(T22N)-YFP
649 (BDSC#9778), UAS-RAB7-YFP (BDSC#23641), UAS-RAB7(Q67L)-YFP (BDSC#9779), UAS-
650 RAB11-YFP (BDSC#50782) and UAS-RAB11(S25N)-YFP (BDSC#9792) (Zhang et al., 2007).

651

652 *Genome engineering of Syt7^{M1} mutant and SYT7^{RFP} knock-in*

653 Guide RNAs were selected using the CRISPR Optimal Target Finder resource (Gratz et al., 2014)
654 and cloned into the plasmid pCFD4-U6:1_U6:3tandemgRNAs (Addgene #49411) (Port et al.,
655 2014). To generate *Syt7*^{M1}, guide RNA containing pCFD4 plasmid was injected into *vasa*-Cas9
656 embryos (BDSC #56552) by Best Gene Inc (Chino Hills, CA, USA). *Syt7*^{M1} and an unaffected
657 injection line (control) were brought into the *white* background and the *vasa*-Cas9 chromosome
658 was removed. To generate SYT7^{RFP}, a donor plasmid that flanked RFP and a DsRed cassette was
659 generated from the pScarless plasmid (courtesy of Kate O'Connor-Giles) with 1 Kb homology
660 arms from the 3' end of the *Syt7* gene. The left homology arm was generated by PCR and the right
661 homology arm was synthesized by Epoch Life Science (Sugarland, TX, USA). The donor plasmid
662 and guide RNA containing pCFD4 plasmid was co-injected into Act5C-Cas9, Lig4 (BDSC
663 #58492) by Best Gene Inc. *Syt7*^{M1} and SYT7^{RFP} transformants were confirmed by DNA
664 sequencing.

665

666 *Sequence alignment, phylogenetic tree construction and molecular modeling*

667 NCBI BLAST was used to identify homologs of SYT1, SYT7 and ESYT-2 in the genomes of *C.*
 668 *elegans*, *C. intestinalis*, *D. rerio*, *M. musculus*, *H. sapiens*, *R. norvegicus* and *T. adherens*. Jalview
 669 was used to align SYT1 and SYT7 protein sequences from *D. melanogaster*, *M. Musculus* and *H.*
 670 *sapiens* with the T-coffee multiple sequence alignment algorithm. Jalview and Matlab were used
 671 to generate a phylogenetic tree using BLOSUM62 matrix and neighbor joining clustering. The
 672 SWISS model server (<https://swissmodel.expasy.org>) was used for homology modeling of
 673 *Drosophila* SYT7 from *R. norvegicus* SYT7 (PBD: 6ANK) (Waterhouse et al., 2018). The PyMOL
 674 Molecular Graphics System (Version 2.0 Schrödinger, LLC) was used to visualize SYT1 and
 675 SYT7 protein structures.

676

Sequences used for sequence alignment and phylogenetic tree		
Protein	Species	NCBI Accession number
ESYT2	<i>C. elegans</i>	NP_741181.1
	<i>C. intestinalis</i>	XP_018671537.1
	<i>D. melanogaster</i>	NP_733011.2
	<i>D. rerio</i>	XP_005171456.1
	<i>H. sapiens</i>	XP_024302614.1
	<i>R. norvegicus</i>	NP_001258098.1
	<i>T. adhaerens</i>	EDV19885.1
SYT1	<i>C. elegans</i>	NP_495394.3
	<i>C. intestinalis</i>	NP_001107602.1
	<i>D. melanogaster</i>	NP_523460.2
	<i>D. rerio</i>	NP_001314758.1
	<i>H. sapiens</i>	NP_001129277.1

	<i>R. norvegicus</i>	NP_001028852.2
	<i>T. adhaerens</i>	XP_002117742.1
SYT7	<i>C. elegans</i>	NP_001254022.1
	<i>C. intestinalis</i>	XP_026696415.1
	<i>D. melanogaster</i>	NP_726560.5
	<i>D. rerio</i>	XP_021326273.1
	<i>H. sapiens</i>	NP_004191.2
	<i>R. norvegicus</i>	NP_067691.1
	<i>T. adhaerens</i>	XP_002117784.1

677

678 *Western analysis and immunocytochemistry*

679 Western blotting of adult head lysates (1 head/lane) was performed using standard laboratory
680 procedures with anti-SYT7 (1:500) (Adolfson et al., 2004), anti-SYX1 (8C3, 1:1000,
681 Developmental Studies Hybridoma Bank (DSHB, Iowa City, IA) and anti-RFP (600-401-379;
682 Rockland, 1:5000). Visualization and quantification were performed with a LI-COR Odyssey
683 Imaging System (LI-COR Biosciences, Lincoln, MA, USA). Secondary antibodies for Westerns
684 included Alexa Fluor 680-conjugated goat anti-rabbit IgG (1:5000, Invitrogen; A21109) and IR
685 Dye 800-conjugated goat anti-mouse IgG (1:5000, LICOR; 926-32211).

686 Immunostaining for AZ and bouton counting was performed on wandering stage 3rd instar
687 larvae dissected in Ca²⁺-free HL3.1 and fixed for 17 min in Ca²⁺-free HL3.1 containing 4% PFA.
688 Larvae were blocked and permeabilized for 1 hr in PBS containing 0.1% Triton X-100, 2.5% NGS,
689 2.5% BSA and 0.1% sodium azide. Larvae were incubated overnight with primary antibody at 4°C
690 and 2 hrs in secondary antibody at room temperature. Samples were mounted on slides with
691 Vectashield (Vector Laboratories, Burlingame, CA). Immunostaining for SYT7^{RFP} and STY7^{GFP}
692 co-localization analysis was similar, except larvae were blocked and permeabilized overnight in
693 PBS containing 0.25% Saponin, 2.5% normal goat serum (NGS), 2.5% bovine serum albumin
694 (BSA) and 0.1% sodium azide. Fixed larvae were incubated with primary antibody at 4°C for 24
695 hrs and with secondary antibodies for 1.5 hrs at room temperature. Fixed larvae were mounted in

696 ProLong® Diamond Antifade Mountant (#P36970; Thermo Fisher Scientific, Waltham, MA,
697 USA).

698 Antibodies used for immunolabeling were: mouse anti-BRP at 1:500 (Nc82; DSHB), mouse
699 anti-DYN at 1:1000 (Clone 41, Dynamin (RUO); BD Transduction Laboratories, San Jose, CA,
700 USA), mouse anti-Golgin84 at 1:50 (Golgin84 12-1; DSHB), mouse anti-RAB7 at 1:10 (Rab7;
701 DSHB), mouse anti-RFP at 1:1000 (200-301-379; Rockland, Limerick, PA, USA) mouse anti-
702 SYX1 at 1:100 (8C3; DSHB), rabbit anti-CPX at 1:5000 (Huntwork and Littleton, 2007), rabbit
703 anti-NWK at 1:1000 (gift from Avital Rodal), rabbit anti-SYT1 1:500, mouse anti-GFP at 1:1000
704 (#A-11120; Thermo Fisher Scientific, Waltham, MA, USA), rabbit anti-GFP at 1:1000 (#G10362;
705 Thermo Fisher Scientific, Waltham, MA, USA), mouse anti-RFP at 1:1000 (200-301-379;
706 Rockland), rabbit anti-RFP at 1:1000 (600-401-379; Rockland) and DyLight 649 conjugated anti-
707 HRP at 1:1000 (#123-605-021; Jackson Immuno Research, West Grove, PA, USA). Secondary
708 antibodies used for AZ and bouton counting were used at 1:1000: goat anti-rabbit Alexa Fluor
709 488-conjugated antibody (A-11008; ThermoFisher) and goat anti-mouse Alexa Fluor 546-
710 conjugated antibody (A-11030; ThermoFisher). Secondary antibodies used for co-localization
711 were used at 1:1000: goat anti-mouse Alexa Fluor Plus 555 (A32727; ThermoFisher), goat anti-
712 mouse Alexa Fluor Plus 488 (A32723; ThermoFisher), goat anti-rabbit Alexa Fluor Plus 555
713 (A32732; ThermoFisher) and goat anti-rabbit Alexa Fluor Plus 488 (A32731; ThermoFisher).

714 Immunoreactive proteins were imaged on either a Zeiss Pascal Confocal (Carl Zeiss
715 Microscopy, Jena, GERMANY) using a 40x or 63X NA 1.3 Plan Neofluar oil immersion objective
716 or a ZEISS LSM 800 microscope with Airyscan using a 63X oil immersion objective. For AZ
717 volume and AZ proximity measurements, samples were imaged on a Zeiss Airyscan microscope
718 and BRP labeling was analyzed in Volocity 6.3.1 software (Quorum Technologies Inc., Puslinch,
719 Ontario, CAN). AZs clusters larger than $0.2 \mu\text{m}^3$ were rarely found, but could not be resolved into
720 single objects by the software. To ensure such clusters did not affect AZ size analysis, all AZs
721 larger than $0.2 \mu\text{m}^3$ were excluded from the analysis.

722

723 *Electrophysiology*

724 Postsynaptic currents from the indicated genotypes were recorded from 3rd instar muscle fiber 6 at
725 segment A3 using two-electrode voltage clamp with a -80 mV holding potential in HL3.1 saline
726 solution (in mM, 70 NaCl, 5 KCl, 10 NaHCO₃, 4 MgCl₂, 5 trehalose, 115 sucrose, 5 HEPES, pH

727 7.2) as previously described (Jorquera et al., 2012). Final $[Ca^{2+}]$ was adjusted to the level indicated
728 in the text. For experiments using bafilomycin, 4 μ m bafilomycin (LC Laboratories, Woburn, MA,
729 USA) was dissolved in dimethyl sulphoxide (DMSO, Sigma, St. Louis, MO, USA) in HL3.1 and
730 bath applied to dissected larvae. DMSO containing HL3.1 was used for control. Data acquisition
731 and analysis was performed using Axoscope 9.0 and Clampfit 9.0 software (Molecular Devices,
732 Sunnyvale, CA, USA). mEJCs were analyzed with Mini Analysis software 6.0.3 (Synaptosoft,
733 Decatur, GA, USA). Motor nerves innervating the musculature were severed and placed into a
734 suction electrode. Action potential stimulation was applied at the indicated frequencies using a
735 programmable stimulator (Master8, AMPI; Jerusalem, Israel).

736

737 *Optical quantal imaging and P_r mapping*

738 P_r mapping was performed on a Zeiss Axio Imager 2 equipped with a spinning-disk confocal head
739 (CSU-X1; Yokagawa, JAPAN) and ImagEM X2 EM-CCD camera (Hamamatsu, Hamamatsu City
740 JAPAN) as previously described (Akbergenova et al., 2018). Myristoylated-GCaMP6s was
741 expressed with 44H10-LexAp65 (provided by Gerald Rubin). Postsynaptic densities were
742 visualized by expression of GluRIIA-RFP under its endogenous promoter (provided by Stephan
743 Sigrist). An Olympus LUMFL N 60X objective with a 1.10 NA was used to acquire GCaMP6s
744 imaging data at 8 Hz. 3rd instar larvae were dissected in Ca^{2+} -free HL3 containing 20 mM $MgCl_2$.
745 After dissection, preparations were maintained in HL3 with 20 mM $MgCl_2$ and 1.0 mM Ca^{2+} for 5
746 minutes. Motor nerves were stimulated every three seconds for GCaMP6s mapping. The time and
747 location of Ca^{2+} events were imported into Excel or Matlab for further analysis. The number of
748 observed GCaMP events per AZ was divided by the number of stimuli to calculate AZ P_r .

749

750 *FMI-43 uptake and release assays*

751 3rd instar wandering larvae were dissected in Ca^{2+} -free HL3.1 and axons were severed from the
752 CNS. Axon bundles were stimulated with a suction electrode in 1.5 mM $CaCl_2$ HL3.1 solution
753 containing 2 μ M of the lipophilic dye FM 1-43FX (F35355; Thermo Fisher Scientific, Waltham,
754 MA, USA). Dye loading was performed at 10 Hz for 50 seconds (500 events) or at 0.5 Hz for 300
755 seconds (150 events), 600 seconds (300 events) and 900 seconds (600 events) as indicated. After
756 stimulation, samples were washed for 2 min in Ca^{2+} free HL3.1 containing 100 μ M Advacep-7
757 (Sigma; A3723) to help remove non-internalized FM 1-43 dye. Image stacks from muscle 6/7 at

758 segment A3 were obtained using a spinning disk confocal microscope. FM1-43 unloading was
759 done with a high K⁺ (90 mM) HL3.1 solution for 1 min, followed by washing in a Ca²⁺ free HL3.1
760 solution for 1 min. An image stack at segment A3 muscle 6-7 was obtained on a Zeiss Axio Imager
761 2 equipped with a spinning-disk confocal head with a 63X water immersion objective. Mean FM1-
762 43 intensity at the NMJ was quantified using the Volocity 3D Image Analysis software (Quorum
763 Technologies Inc., Puslinch, Ontario, CAN).

764

765 *Electron microscopy*

766 *Syt1^{MI}* and control 3rd instar larvae were dissected in Ca²⁺-free HL3.1 solution and fixed in 1%
767 glutaraldehyde, 4% formaldehyde, and 0.1 M sodium cacodylate for 10 min at room temperature
768 as previously described (Akbergenova and Bykhovskaia, 2009). Fresh fixative was added and
769 samples were microwaved in a BioWave Pro Pelco (Ted Pella, Inc., Redding, CA, USA) with the
770 following protocol: (1) 100W 1 min, (2) 1 min off, (3) 100W 1 min, (4) 300W 20 secs, (5) 20 secs
771 off, (6) 300W 20 secs. Steps 4- 6 were repeated twice more. Samples were then incubated for 30
772 min at room temperature with fixative. After washing in 0.1 M sodium cacodylate and 0.1 M
773 sucrose, samples were stained for 30 min in 1% osmium tetroxide and 1.5% potassium
774 ferrocyanide in 0.1 M sodium cacodylate solution. After washing with 0.1 M sodium cacodylate,
775 samples were stained for 30 mins in 2% uranyl acetate and dehydrated through a graded series of
776 ethanol and acetone, before embedding in epoxy resin (Embed 812; Electron Microscopy
777 Sciences). Thin sections (50–60 nm) were collected on Formvar/carbon-coated copper slot grids
778 and contrasted with lead citrate. Sections were imaged at 49,000× magnification at 80 kV with a
779 Tecnai G2 electron microscope (FEI, Hillsboro, OR, USA) equipped with a charge-coupled device
780 camera (Advanced Microscopy Techniques, Woburn, MA, USA). Type 1b boutons at muscle 6/7
781 were analyzed. All data analysis was done blinded.

782 For SV counting, T-bars at Ib boutons were identified and a FIJI macro was used to draw four
783 concentric circles with 100 nm, 200 nm, 300 nm or 400 nm radius. The concentric circles were
784 drawn with the T-bar at the center. To quantify vesicle density, FIJI was used to measure the area
785 of the bouton and quantify the total number of vesicles within it. Final analysis was performed in
786 Matlab and Excel.

787

788 *Co-localization analysis and 3D reconstruction*

789 The JaCOP FIJI algorithm (Bolte and Cordelières, 2006) was used to obtain cytofluorogram plots
790 of bouton image stacks that were probed for RFP and a 2nd labeled compartment in SYT7^{RFP} 3rd
791 instar larvae. Automatic thresholding was used to identify pixels above background for both
792 channels. To obtain an average Pearson correlation, cytofluorograms from boutons obtained from
793 3 animals were analyzed in Matlab. All data analysis was done blinded. 3D reconstruction was
794 performed using the 3D Viewer plugin in FIJI (Schmid et al., 2010). The bouton stack was
795 displayed as a surface and labeled with SYT7^{RFP} in magenta and HRP in black.

796

797 *Statistical analysis*

798 Statistical analysis and graphing was performed with either Origin Software (OriginLab
799 Corporation, Northampton, MA, USA) or GraphPad Prism (San Diego, CA, USA). Statistical
800 significance was determined using specific tests as indicated in the text. Appropriate sample size
801 was determined using GraphPad Statmate. Asterisks denote p-values of: *, $P \leq 0.05$; **, $P \leq 0.01$;
802 and ***, $P \leq 0.001$. All histograms and measurements are shown as mean \pm SEM.

803

804 **Acknowledgements**

805 This work was supported by NIH grant NS40296 to J.T.L. We thank the Bloomington Drosophila
806 Stock Center (NIH P40OD018537), Kate O’Conner-Giles, Hugo Bellen, Gerry Rubin and Stephan
807 Sigrist for Drosophila stocks, Kate O’Conner-Giles (Brown University) for help with CRISPR,
808 Avi Rodal (Brandeis University) and Noreen Reist (Colorado State University) for providing
809 antisera, Jan Melom (MIT) for generating the UAS-NHE-GFP transgenic line, Dina Volfson
810 (MIT) for assistance with Drosophila stock generation, and members of the Littleton lab for helpful
811 discussions and comments on the manuscript.

812

813 **Competing Interests**

814 The authors declare no competing interests.

815

816

817 **References**

- 818
- 819 Adolfsen, B., Littleton, J.T., 2001. Genetic and molecular analysis of the synaptotagmin family.
820 *Cell Mol Life Sci* 58, 393–402. doi:10.1007/PL00000865
- 821 Adolfsen, B., Saraswati, S., Yoshihara, M., Littleton, J.T., 2004. Synaptotagmins are trafficked to
822 distinct subcellular domains including the postsynaptic compartment. *J Cell Biol* 166, 249–
823 260. doi:10.1083/jcb.200312054
- 824 Akbergenova, Y., Bykhovskaia, M., 2007. Synapsin maintains the reserve vesicle pool and spatial
825 segregation of the recycling pool in *Drosophila* presynaptic boutons. *Brain Res* 1178, 52–
826 64. doi:10.1016/j.brainres.2007.08.042
- 827 Akbergenova, Y., Bykhovskaia, M., 2009. Stimulation-induced formation of the reserve pool of
828 vesicles in *Drosophila* motor boutons. *J Neurophysiol* 101, 2423–2433.
829 doi:10.1152/jn.91122.2008
- 830 Akbergenova, Y., Cunningham, K.L., Zhang, Y.V., Weiss, S., Littleton, J.T., 2018.
831 Characterization of developmental and molecular factors underlying release heterogeneity
832 at *Drosophila* synapses. *elife* 7. doi:10.7554/eLife.38268
- 833 Atluri, P.P., Regehr, W.G., 1998. Delayed release of neurotransmitter from cerebellar granule
834 cells. *J Neurosci* 18, 8214–8227.
- 835 Bacaj, T., Wu, D., Burré, J., Malenka, R.C., Liu, X., Südhof, T.C., 2015. Synaptotagmin-1 and -7
836 Are Redundantly Essential for Maintaining the Capacity of the Readily-Releasable Pool of
837 Synaptic Vesicles. *PLoS Biol* 13, e1002267. doi:10.1371/journal.pbio.1002267
- 838 Bacaj, T., Wu, D., Yang, X., Morishita, W., Zhou, P., Xu, W., Malenka, R.C., Südhof, T.C., 2013.
839 Synaptotagmin-1 and synaptotagmin-7 trigger synchronous and asynchronous phases of
840 neurotransmitter release. *Neuron* 80, 947–959. doi:10.1016/j.neuron.2013.10.026
- 841 Barber, C.F., Jorquera, R.A., Melom, J.E., Littleton, J.T., 2009. Postsynaptic regulation of synaptic
842 plasticity by synaptotagmin 4 requires both C2 domains. *J Cell Biol* 187, 295–310.
843 doi:10.1083/jcb.200903098
- 844 Barthet, G., Jordà-Siquier, T., Rumi-Masante, J., Bernadou, F., Müller, U., Mülle, C., 2018.
845 Presenilin-mediated cleavage of APP regulates synaptotagmin-7 and presynaptic plasticity.
846 *Nat Commun* 9, 4780. doi:10.1038/s41467-018-06813-x
- 847 Barzilai-Tutsch, H., Dewulf, M., Lamaze, C., Butler Browne, G., Pines, M., Halevy, O., 2018. A
848 promotive effect for halofuginone on membrane repair and synaptotagmin-7 levels in
849 muscle cells of dysferlin-null mice. *Hum Mol Genet* 27, 2817–2829.
850 doi:10.1093/hmg/ddy185
- 851 Bellen, H.J., Levis, R.W., Liao, G., He, Y., Carlson, J.W., Tsang, G., Evans-Holm, M., Hiesinger,
852 P.R., Schulze, K.L., Rubin, G.M., Hoskins, R.A., Spradling, A.C., 2004. The BDGP gene
853 disruption project: single transposon insertions associated with 40% of *Drosophila* genes.
854 *Genetics* 167, 761–781. doi:10.1534/genetics.104.026427
- 855 Best, A.R., Regehr, W.G., 2009. Inhibitory regulation of electrically coupled neurons in the
856 inferior olive is mediated by asynchronous release of GABA. *Neuron* 62, 555–565.
857 doi:10.1016/j.neuron.2009.04.018
- 858 Böhme, M.A., Beis, C., Reddy-Alla, S., Reynolds, E., Mampell, M.M., Grasskamp, A.T.,
859 Lützkendorf, J., Bergeron, D.D., Driller, J.H., Babikir, H., Göttfert, F., Robinson, I.M.,
860 O’Kane, C.J., Hell, S.W., Wahl, M.C., Stelzl, U., Loll, B., Walter, A.M., Sigrist, S.J., 2016.
861 Active zone scaffolds differentially accumulate Unc13 isoforms to tune Ca(2+) channel-
862 vesicle coupling. *Nat Neurosci* 19, 1311–1320. doi:10.1038/nn.4364

- 863 Bolte, S., Cordelières, F.P., 2006. A guided tour into subcellular colocalization analysis in light
864 microscopy. *J Microsc* 224, 213–232. doi:10.1111/j.1365-2818.2006.01706.x
- 865 Borst, J.G., Sakmann, B., 1996. Calcium influx and transmitter release in a fast CNS synapse.
866 *Nature* 383, 431–434. doi:10.1038/383431a0
- 867 Budnik, V., Zhong, Y., Wu, C.F., 1990. Morphological plasticity of motor axons in *Drosophila*
868 mutants with altered excitability. *J Neurosci* 10, 3754–3768.
- 869 Buhl, L.K., Jorquera, R.A., Akbergenova, Y., Huntwork-Rodriguez, S., Volfson, D., Littleton,
870 J.T., 2013. Differential regulation of evoked and spontaneous neurotransmitter release by
871 C-terminal modifications of complexin. *Mol Cell Neurosci* 52, 161–172.
872 doi:10.1016/j.mcn.2012.11.009
- 873 Bykhovskaia, M., 2011. Synapsin regulation of vesicle organization and functional pools. *Semin*
874 *Cell Dev Biol* 22, 387–392. doi:10.1016/j.semcdb.2011.07.003
- 875 Cao, P., Maximov, A., Südhof, T.C., 2011. Activity-dependent IGF-1 exocytosis is controlled by
876 the Ca(2+)-sensor synaptotagmin-10. *Cell* 145, 300–311. doi:10.1016/j.cell.2011.03.034
- 877 Chakrabarti, S., Kobayashi, K.S., Flavell, R.A., Marks, C.B., Miyake, K., Liston, D.R., Fowler,
878 K.T., Gorelick, F.S., Andrews, N.W., 2003. Impaired membrane resealing and autoimmune
879 myositis in synaptotagmin VII-deficient mice. *J Cell Biol* 162, 543–549.
880 doi:10.1083/jcb.200305131
- 881 Chanaday, N.L., Kavalali, E.T., 2018. Presynaptic origins of distinct modes of neurotransmitter
882 release. *Curr Opin Neurobiol* 51, 119–126. doi:10.1016/j.conb.2018.03.005
- 883 Chang, S., Trimbuch, T., Rosenmund, C., 2018. Synaptotagmin-1 drives synchronous Ca²⁺-
884 triggered fusion by C2B-domain-mediated synaptic-vesicle-membrane attachment. *Nat*
885 *Neurosci* 21, 33–40. doi:10.1038/s41593-017-0037-5
- 886 Chapman, E.R., Jahn, R., 1994. Calcium-dependent interaction of the cytoplasmic region of
887 synaptotagmin with membranes. Autonomous function of a single C2-homologous
888 domain. *J Biol Chem* 269, 5735–5741.
- 889 Chen, C., Satterfield, R., Young, S.M., Jonas, P., 2017. Triple Function of Synaptotagmin 7
890 Ensures Efficiency of High-Frequency Transmission at Central GABAergic Synapses. *Cell*
891 *Rep* 21, 2082–2089. doi:10.1016/j.celrep.2017.10.122
- 892 Chen, Z., Das, B., Nakamura, Y., DiGregorio, D.A., Young, S.M., 2015. Ca²⁺ channel to synaptic
893 vesicle distance accounts for the readily releasable pool kinetics at a functionally mature
894 auditory synapse. *J Neurosci* 35, 2083–2100. doi:10.1523/JNEUROSCI.2753-14.2015
- 895 Colvin, R.A., Means, T.K., Diefenbach, T.J., Moita, L.F., Friday, R.P., Sever, S., Campanella,
896 G.S.V., Abrazinski, T., Manice, L.A., Moita, C., Andrews, N.W., Wu, D., Hacohen, N.,
897 Luster, A.D., 2010. Synaptotagmin-mediated vesicle fusion regulates cell migration. *Nat*
898 *Immunol* 11, 495–502. doi:10.1038/ni.1878
- 899 Coyle, I.P., Koh, Y.-H., Lee, W.-C.M., Slind, J., Fergestad, T., Littleton, J.T., Ganetzky, B., 2004.
900 Nervous wreck, an SH3 adaptor protein that interacts with Wsp, regulates synaptic growth
901 in *Drosophila*. *Neuron* 41, 521–534.
- 902 Craxton, M., 2010. A manual collection of Syt, Esyt, Rph3a, Rph3al, Doc2, and Dblc2 genes from
903 46 metazoan genomes--an open access resource for neuroscience and evolutionary biology.
904 *BMC Genomics* 11, 37. doi:10.1186/1471-2164-11-37
- 905 Czubener, C., Sherer, N.M., Becker, S.M., Pypaert, M., Hui, E., Chapman, E.R., Mothes, W.,
906 Andrews, N.W., 2006. Ca²⁺ and synaptotagmin VII-dependent delivery of lysosomal
907 membrane to nascent phagosomes. *J Cell Biol* 174, 997–1007. doi:10.1083/jcb.200605004
- 908 Dean, C., Dunning, F.M., Liu, H., Bomba-Warczak, E., Martens, H., Bharat, V., Ahmed, S.,

- 909 Chapman, E.R., 2012. Axonal and dendritic synaptotagmin isoforms revealed by a
910 pHluorin-syt functional screen. *Mol Biol Cell* 23, 1715–1727. doi:10.1091/mbc.E11-08-
911 0707
- 912 DiAntonio, A., Schwarz, T.L., 1994. The effect on synaptic physiology of synaptotagmin
913 mutations in *Drosophila*. *Neuron* 12, 909–920. doi:10.1016/0896-6273(94)90342-5
- 914 Dickman, D.K., Lu, Z., Meinertzhagen, I.A., Schwarz, T.L., 2006. Altered synaptic development
915 and active zone spacing in endocytosis mutants. *Curr. Biol.* 16, 591–598.
- 916 Dittman, J.S., Kreitzer, A.C., Regehr, W.G., 2000. Interplay between facilitation, depression, and
917 residual calcium at three presynaptic terminals. *J Neurosci* 20, 1374–1385.
- 918 Dittman, J.S., Regehr, W.G., 1998. Calcium dependence and recovery kinetics of presynaptic
919 depression at the climbing fiber to Purkinje cell synapse. *J Neurosci* 18, 6147–6162.
- 920 Dolai, S., Xie, L., Zhu, D., Liang, T., Qin, T., Xie, H., Kang, Y., Chapman, E.R., Gaisano, H.Y.,
921 2016. Synaptotagmin-7 Functions to Replenish Insulin Granules for Exocytosis in Human
922 Islet β -Cells. *Diabetes* 65, 1962–1976. doi:10.2337/db15-1436
- 923 Durán, E., Montes, M.Á., Jemal, I., Satterfield, R., Young, S., Álvarez de Toledo, G., 2018.
924 Synaptotagmin-7 controls the size of the reserve and resting pools of synaptic vesicles in
925 hippocampal neurons. *Cell Calcium* 74, 53–60. doi:10.1016/j.ceca.2018.06.004
- 926 Ehmann, N., van de Linde, S., Alon, A., Ljaschenko, D., Keung, X.Z., Holm, T., Rings, A.,
927 DiAntonio, A., Hallermann, S., Ashery, U., Heckmann, M., Sauer, M., Kittel, R.J., 2014.
928 Quantitative super-resolution imaging of Bruchpilot distinguishes active zone states. *Nat*
929 *Commun* 5, 4650. doi:10.1038/ncomms5650
- 930 Fernández-Chacón, R., Königstorfer, A., Gerber, S.H., García, J., Matos, M.F., Stevens, C.F.,
931 Brose, N., Rizo, J., Rosenmund, C., Südhof, T.C., 2001. Synaptotagmin I functions as a
932 calcium regulator of release probability. *Nature* 410, 41–49. doi:10.1038/35065004
- 933 Fesce, R., 1999. The kinetics of nerve-evoked quantal secretion. *Philos Trans R Soc Lond, B, Biol*
934 *Sci* 354, 319–329. doi:10.1098/rstb.1999.0383
- 935 Flannery, A.R., Czibener, C., Andrews, N.W., 2010. Palmitoylation-dependent association with
936 CD63 targets the Ca²⁺ sensor synaptotagmin VII to lysosomes. *J Cell Biol* 191, 599–613.
937 doi:10.1083/jcb.201003021
- 938 Frank, C.A., James, T.D., Müller, M., 2020. Homeostatic control of *Drosophila* neuromuscular
939 junction function. *Synapse* 74, e22133. doi:10.1002/syn.22133
- 940 Fukuda, M., Kanno, E., Satoh, M., Saegusa, C., Yamamoto, A., 2004. Synaptotagmin VII is
941 targeted to dense-core vesicles and regulates their Ca²⁺-dependent exocytosis in PC12
942 cells. *J Biol Chem* 279, 52677–52684. doi:10.1074/jbc.M409241200
- 943 Geppert, M., Goda, Y., Hammer, R.E., Li, C., Rosahl, T.W., Stevens, C.F., Südhof, T.C., 1994.
944 Synaptotagmin I: a major Ca²⁺ sensor for transmitter release at a central synapse. *Cell* 79,
945 717–727. doi:10.1016/0092-8674(94)90556-8
- 946 Gerth, F., Jäpel, M., Pechstein, A., Kochlamazashvili, G., Lehmann, M., Puchkov, D., Onofri, F.,
947 Benfenati, F., Nikonenko, A.G., Fredrich, K., Shupliakov, O., Maritzen, T., Freund, C.,
948 Haucke, V., 2017. Intersectin associates with synapsin and regulates its nanoscale
949 localization and function. *Proc Natl Acad Sci U S A* 114, 12057–12062.
950 doi:10.1073/pnas.1715341114
- 951 Goda, Y., Stevens, C.F., 1994. Two components of transmitter release at a central synapse. *Proc*
952 *Natl Acad Sci U S A* 91, 12942–12946. doi:10.1073/pnas.91.26.12942
- 953 Gratz, S.J., Ukken, F.P., Rubinstein, C.D., Thiede, G., Donohue, L.K., Cummings, A.M.,
954 O'Connor-Giles, K.M., 2014. Highly specific and efficient CRISPR/Cas9-catalyzed

- 955 homology-directed repair in *Drosophila*. *Genetics* 196, 961–971.
956 doi:10.1534/genetics.113.160713
- 957 Guan, Z., Bykhovskaia, M., Jorquera, R.A., Sutton, R.B., Akbergenova, Y., Littleton, J.T., 2017.
958 A synaptotagmin suppressor screen indicates SNARE binding controls the timing and
959 Ca²⁺ cooperativity of vesicle fusion. *elife* 6. doi:10.7554/eLife.28409
- 960 Guan, Z., Saraswati, S., Adolfsen, B., Littleton, J.T., 2005. Genome-wide transcriptional changes
961 associated with enhanced activity in the *Drosophila* nervous system. *Neuron* 48, 91–107.
962 doi:10.1016/j.neuron.2005.08.036
- 963 Gustavsson, N., Wang, Y., Kang, Y., Seah, T., Chua, S., Radda, G.K., Han, W., 2011.
964 Synaptotagmin-7 as a positive regulator of glucose-induced glucagon-like peptide-1
965 secretion in mice. *Diabetologia* 54, 1824–1830. doi:10.1007/s00125-011-2119-3
- 966 Harris, K.P., Littleton, J.T., 2015. Transmission, development, and plasticity of synapses. *Genetics*
967 201, 345–375. doi:10.1534/genetics.115.176529
- 968 Harris, K.P., Zhang, Y.V., Piccioli, Z.D., Perrimon, N., Littleton, J.T., 2016. The postsynaptic t-
969 SNARE Syntaxin 4 controls traffic of Neuroligin 1 and Synaptotagmin 4 to regulate
970 retrograde signaling. *elife* 5. doi:10.7554/eLife.13881
- 971 Hefft, S., Jonas, P., 2005. Asynchronous GABA release generates long-lasting inhibition at a
972 hippocampal interneuron-principal neuron synapse. *Nat Neurosci* 8, 1319–1328.
973 doi:10.1038/nn1542
- 974 Hilfiker, S., Pieribone, V.A., Czernik, A.J., Kao, H.T., Augustine, G.J., Greengard, P., 1999.
975 Synapsins as regulators of neurotransmitter release. *Philos Trans R Soc Lond, B, Biol Sci*
976 354, 269–279. doi:10.1098/rstb.1999.0378
- 977 Hui, E., Bai, J., Wang, P., Sugimori, M., Llinas, R.R., Chapman, E.R., 2005. Three distinct kinetic
978 groupings of the synaptotagmin family: candidate sensors for rapid and delayed exocytosis.
979 *Proc Natl Acad Sci U S A* 102, 5210–5214. doi:10.1073/pnas.0500941102
- 980 Huntwork, S., Littleton, J.T., 2007. A complexin fusion clamp regulates spontaneous
981 neurotransmitter release and synaptic growth. *Nat Neurosci* 10, 1235–1237.
982 doi:10.1038/nn1980
- 983 Huson, V., van Boven, M.A., Stuefer, A., Verhage, M., Cornelisse, L.N., 2019. Synaptotagmin-1
984 enables frequency coding by suppressing asynchronous release in a temperature dependent
985 manner. *Sci. Rep.* 9, 11341. doi:10.1038/s41598-019-47487-9
- 986 Jackman, S.L., Turecek, J., Belinsky, J.E., Regehr, W.G., 2016. The calcium sensor synaptotagmin
987 7 is required for synaptic facilitation. *Nature* 529, 88–91. doi:10.1038/nature16507
- 988 Jaiswal, J.K., Chakrabarti, S., Andrews, N.W., Simon, S.M., 2004. Synaptotagmin VII restricts
989 fusion pore expansion during lysosomal exocytosis. *PLoS Biol* 2, E233.
990 doi:10.1371/journal.pbio.0020233
- 991 Jan, L.Y., Jan, Y.N., 1976. Properties of the larval neuromuscular junction in *Drosophila*
992 melanogaster. *J Physiol (Lond)* 262, 189–214. doi:10.1113/jphysiol.1976.sp011592
- 993 Jorquera, R.A., Huntwork-Rodriguez, S., Akbergenova, Y., Cho, R.W., Littleton, J.T., 2012.
994 Complexin controls spontaneous and evoked neurotransmitter release by regulating the
995 timing and properties of synaptotagmin activity. *J Neurosci* 32, 18234–18245.
996 doi:10.1523/JNEUROSCI.3212-12.2012
- 997 Junge, H.J., Rhee, J.-S., Jahn, O., Varoqueaux, F., Spiess, J., Waxham, M.N., Rosenmund, C.,
998 Brose, N., 2004. Calmodulin and Munc13 form a Ca²⁺ sensor/effector complex that
999 controls short-term synaptic plasticity. *Cell* 118, 389–401. doi:10.1016/j.cell.2004.06.029
- 1000 Kaeser, P.S., Regehr, W.G., 2014. Molecular mechanisms for synchronous, asynchronous, and

- 1001 spontaneous neurotransmitter release. *Annu Rev Physiol* 76, 333–363.
1002 doi:10.1146/annurev-physiol-021113-170338
- 1003 Katz, B., Miledi, R., 1967. The timing of calcium action during neuromuscular transmission. *J*
1004 *Physiol (Lond)* 189, 535–544. doi:10.1113/jphysiol.1967.sp008183
- 1005 Katz, B., Miledi, R., 1970. Further study of the role of calcium in synaptic transmission. *J Physiol*
1006 (Lond) 207, 789–801. doi:10.1113/jphysiol.1970.sp009095
- 1007 Katz, B.S., 1969. *The Release of Neural Transmitter Substances (Sherrington Lecture)*: Bernard
1008 S. Katz: 9780853230601: Amazon.com: Books. Liverpool University Press.
- 1009 Kochubey, O., Schneggenburger, R., 2011. Synaptotagmin increases the dynamic range of
1010 synapses by driving Ca²⁺-evoked release and by clamping a near-linear remaining Ca²⁺
1011 sensor. *Neuron* 69, 736–748. doi:10.1016/j.neuron.2011.01.013
- 1012 Koh, T.-W., Verstreken, P., Bellen, H.J., 2004. Dap160/intersectin acts as a stabilizing scaffold
1013 required for synaptic development and vesicle endocytosis. *Neuron* 43, 193–205.
1014 doi:10.1016/j.neuron.2004.06.029
- 1015 Korkut, C., Li, Y., Koles, K., Brewer, C., Ashley, J., Yoshihara, M., Budnik, V., 2013. Regulation
1016 of postsynaptic retrograde signaling by presynaptic exosome release. *Neuron* 77, 1039–
1017 1046. doi:10.1016/j.neuron.2013.01.013
- 1018 Lee, J., Guan, Z., Akbergenova, Y., Littleton, J.T., 2013. Genetic analysis of synaptotagmin C2
1019 domain specificity in regulating spontaneous and evoked neurotransmitter release. *J*
1020 *Neurosci* 33, 187–200. doi:10.1523/JNEUROSCI.3214-12.2013
- 1021 Lee, J., Littleton, J.T., 2015. Transmembrane tethering of synaptotagmin to synaptic vesicles
1022 controls multiple modes of neurotransmitter release. *Proc Natl Acad Sci U S A* 112, 3793–
1023 3798. doi:10.1073/pnas.1420312112
- 1024 Li, C., Ullrich, B., Zhang, J.Z., Anderson, R.G., Brose, N., Südhof, T.C., 1995. Ca(2+)-dependent
1025 and -independent activities of neural and non-neural synaptotagmins. *Nature* 375, 594–
1026 599. doi:10.1038/375594a0
- 1027 Li, Y.C., Chanaday, N.L., Xu, W., Kavalali, E.T., 2017. Synaptotagmin-1- and Synaptotagmin-7-
1028 Dependent Fusion Mechanisms Target Synaptic Vesicles to Kinetically Distinct Endocytic
1029 Pathways. *Neuron* 93, 616–631.e3. doi:10.1016/j.neuron.2016.12.010
- 1030 Lipstein, N., Sakaba, T., Cooper, B.H., Lin, K.-H., Strenzke, N., Ashery, U., Rhee, J.-S.,
1031 Taschenberger, H., Neher, E., Brose, N., 2013. Dynamic control of synaptic vesicle
1032 replenishment and short-term plasticity by Ca(2+)-calmodulin-Munc13-1 signaling.
1033 *Neuron* 79, 82–96. doi:10.1016/j.neuron.2013.05.011
- 1034 Littleton, J.T., Bellen, H.J., Perin, M.S., 1993a. Expression of synaptotagmin in *Drosophila* reveals
1035 transport and localization of synaptic vesicles to the synapse. *Development* 118, 1077–
1036 1088.
- 1037 Littleton, J.T., Chapman, E.R., Kreber, R., Garment, M.B., Carlson, S.D., Ganetzky, B., 1998.
1038 Temperature-sensitive paralytic mutations demonstrate that synaptic exocytosis requires
1039 SNARE complex assembly and disassembly. *Neuron* 21, 401–413.
- 1040 Littleton, J.T., Stern, M., Perin, M., Bellen, H.J., 1994. Calcium dependence of neurotransmitter
1041 release and rate of spontaneous vesicle fusions are altered in *Drosophila* synaptotagmin
1042 mutants. *Proc Natl Acad Sci U S A* 91, 10888–10892.
- 1043 Littleton, J.T., Stern, M., Schulze, K., Perin, M., Bellen, H.J., 1993b. Mutational analysis of
1044 *Drosophila* synaptotagmin demonstrates its essential role in Ca(2+)-activated
1045 neurotransmitter release. *Cell* 74, 1125–1134. doi:10.1016/0092-8674(93)90733-7
- 1046 Liu, H., Bai, H., Hui, E., Yang, L., Evans, C.S., Wang, Z., Kwon, S.E., Chapman, E.R., 2014.

- 1047 Synaptotagmin 7 functions as a Ca²⁺-sensor for synaptic vesicle replenishment. *elife* 3,
1048 e01524. doi:10.7554/eLife.01524
- 1049 Llinás, R., Steinberg, I.Z., Walton, K., 1981. Relationship between presynaptic calcium current
1050 and postsynaptic potential in squid giant synapse. *Biophys J* 33, 323–351.
1051 doi:10.1016/S0006-3495(81)84899-0
- 1052 Loewen, C.A., Mackler, J.M., Reist, N.E., 2001. *Drosophila* synaptotagmin I null mutants survive
1053 to early adulthood. *Genesis* 31, 30–36. doi:10.1002/gene.10002
- 1054 Lu, T., Trussell, L.O., 2000. Inhibitory transmission mediated by asynchronous transmitter release.
1055 *Neuron* 26, 683–694. doi:10.1016/s0896-6273(00)81204-0
- 1056 Luo, F., Südhof, T.C., 2017. Synaptotagmin-7-Mediated Asynchronous Release Boosts High-
1057 Fidelity Synchronous Transmission at a Central Synapse. *Neuron* 94, 826–839.e3.
1058 doi:10.1016/j.neuron.2017.04.020
- 1059 MacDougall, D.D., Lin, Z., Chon, N.L., Jackman, S.L., Lin, H., Knight, J.D., Anantharam, A.,
1060 2018. The high-affinity calcium sensor synaptotagmin-7 serves multiple roles in regulated
1061 exocytosis. *J Gen Physiol* 150, 783–807. doi:10.1085/jgp.201711944
- 1062 Mackler, J.M., Drummond, J.A., Loewen, C.A., Robinson, I.M., Reist, N.E., 2002. The C(2)B
1063 Ca(2+)-binding motif of synaptotagmin is required for synaptic transmission in vivo.
1064 *Nature* 418, 340–344. doi:10.1038/nature00846
- 1065 Marie, B., Sweeney, S.T., Poskanzer, K.E., Roos, J., Kelly, R.B., Davis, G.W., 2004.
1066 Dap160/intersectin scaffolds the periaxonal zone to achieve high-fidelity endocytosis and
1067 normal synaptic growth. *Neuron* 43, 207–219. doi:10.1016/j.neuron.2004.07.001
- 1068 Martinez, I., Chakrabarti, S., Hellevik, T., Morehead, J., Fowler, K., Andrews, N.W., 2000.
1069 Synaptotagmin VII regulates Ca(2+)-dependent exocytosis of lysosomes in fibroblasts. *J*
1070 *Cell Biol* 148, 1141–1149. doi:10.1083/jcb.148.6.1141
- 1071 Maximov, A., Lao, Y., Li, H., Chen, X., Rizo, J., Sørensen, J.B., Südhof, T.C., 2008. Genetic
1072 analysis of synaptotagmin-7 function in synaptic vesicle exocytosis. *Proc Natl Acad Sci U*
1073 *S A* 105, 3986–3991. doi:10.1073/pnas.0712372105
- 1074 McCabe, B.D., Marqués, G., Haghghi, A.P., Fetter, R.D., Crotty, M.L., Haerry, T.E., Goodman,
1075 C.S., O’Connor, M.B., 2003. The BMP homolog Gbb provides a retrograde signal that
1076 regulates synaptic growth at the *Drosophila* neuromuscular junction. *Neuron* 39, 241–254.
1077 doi:10.1016/s0896-6273(03)00426-4
- 1078 Melom, J.E., Akbergenova, Y., Gavornik, J.P., Littleton, J.T., 2013. Spontaneous and evoked
1079 release are independently regulated at individual active zones. *J Neurosci* 33, 17253–
1080 17263. doi:10.1523/JNEUROSCI.3334-13.2013
- 1081 Mendez, J.A., Bourque, M.-J., Fasano, C., Kortleven, C., Trudeau, L.-E., 2011. Somatodendritic
1082 dopamine release requires synaptotagmin 4 and 7 and the participation of voltage-gated
1083 calcium channels. *J Biol Chem* 286, 23928–23937. doi:10.1074/jbc.M111.218032
- 1084 Milovanovic, D., De Camilli, P., 2017. Synaptic vesicle clusters at synapses: A distinct liquid
1085 phase? *Neuron* 93, 995–1002. doi:10.1016/j.neuron.2017.02.013
- 1086 Milovanovic, D., Wu, Y., Bian, X., De Camilli, P., 2018. A liquid phase of synapsin and lipid
1087 vesicles. *Science* 361, 604–607. doi:10.1126/science.aat5671
- 1088 Moghadam, P.K., Jackson, M.B., 2013. The functional significance of synaptotagmin diversity in
1089 neuroendocrine secretion. *Front Endocrinol (Lausanne)* 4, 124.
1090 doi:10.3389/fendo.2013.00124
- 1091 Monterrat, C., Grise, F., Benassy, M.N., Hémar, A., Lang, J., 2007. The calcium-sensing protein
1092 synaptotagmin 7 is expressed on different endosomal compartments in endocrine,

- 1093 neuroendocrine cells or neurons but not on large dense core vesicles. *Histochem Cell Biol*
1094 127, 625–632. doi:10.1007/s00418-007-0271-0
- 1095 Neher, E., 2015. Merits and limitations of vesicle pool models in view of heterogeneous
1096 populations of synaptic vesicles. *Neuron* 87, 1131–1142.
1097 doi:10.1016/j.neuron.2015.08.038
- 1098 Neher, E., Brose, N., 2018. Dynamically Primed Synaptic Vesicle States: Key to Understand
1099 Synaptic Short-Term Plasticity. *Neuron* 100, 1283–1291.
1100 doi:10.1016/j.neuron.2018.11.024
- 1101 Nishiki, T., Augustine, G.J., 2004. Synaptotagmin I synchronizes transmitter release in mouse
1102 hippocampal neurons. *J Neurosci* 24, 6127–6132. doi:10.1523/JNEUROSCI.1563-
1103 04.2004
- 1104 Packard, M., Koo, E.S., Gorczyca, M., Sharpe, J., Cumberledge, S., Budnik, V., 2002. The
1105 *Drosophila* Wnt, wingless, provides an essential signal for pre- and postsynaptic
1106 differentiation. *Cell* 111, 319–330. doi:10.1016/s0092-8674(02)01047-4
- 1107 Pang, Z.P., Melicoff, E., Padgett, D., Liu, Y., Teich, A.F., Dickey, B.F., Lin, W., Adachi, R.,
1108 Südhof, T.C., 2006. Synaptotagmin-2 is essential for survival and contributes to Ca²⁺
1109 triggering of neurotransmitter release in central and neuromuscular synapses. *J Neurosci*
1110 26, 13493–13504. doi:10.1523/JNEUROSCI.3519-06.2006
- 1111 Pang, Z.P., Südhof, T.C., 2010. Cell biology of Ca²⁺-triggered exocytosis. *Curr Opin Cell Biol*
1112 22, 496–505. doi:10.1016/j.ceb.2010.05.001
- 1113 Park, D., Li, P., Dani, A., Taghert, P.H., 2014. Peptidergic cell-specific synaptotagmins in
1114 *Drosophila*: localization to dense-core granules and regulation by the bHLH protein
1115 DIMMED. *J Neurosci* 34, 13195–13207. doi:10.1523/JNEUROSCI.2075-14.2014
- 1116 Peled, E.S., Isacoff, E.Y., 2011. Optical quantal analysis of synaptic transmission in wild-type and
1117 rab3-mutant *Drosophila* motor axons. *Nat Neurosci* 14, 519–526. doi:10.1038/nn.2767
- 1118 Perin, M.S., Fried, V.A., Mignery, G.A., Jahn, R., Südhof, T.C., 1990. Phospholipid binding by a
1119 synaptic vesicle protein homologous to the regulatory region of protein kinase C. *Nature*
1120 345, 260–263. doi:10.1038/345260a0
- 1121 Peters, J.H., McDougall, S.J., Fawley, J.A., Smith, S.M., Andresen, M.C., 2010. Primary afferent
1122 activation of thermosensitive TRPV1 triggers asynchronous glutamate release at central
1123 neurons. *Neuron* 65, 657–669. doi:10.1016/j.neuron.2010.02.017
- 1124 Piccioli, Z.D., Littleton, J.T., 2014. Retrograde BMP signaling modulates rapid activity-dependent
1125 synaptic growth via presynaptic LIM kinase regulation of cofilin. *J Neurosci* 34, 4371–
1126 4381. doi:10.1523/JNEUROSCI.4943-13.2014
- 1127 Port, F., Chen, H.-M., Lee, T., Bullock, S.L., 2014. Optimized CRISPR/Cas tools for efficient
1128 germline and somatic genome engineering in *Drosophila*. *Proc Natl Acad Sci U S A* 111,
1129 E2967-76. doi:10.1073/pnas.1405500111
- 1130 Reddy, A., Caler, E.V., Andrews, N.W., 2001. Plasma membrane repair is mediated by Ca²⁺-
1131 regulated exocytosis of lysosomes. *Cell* 106, 157–169. doi:10.1016/s0092-8674(01)00421-
1132 4
- 1133 Ritzau-Jost, A., Jablonski, L., Viotti, J., Lipstein, N., Eilers, J., Hallermann, S., 2018. Apparent
1134 calcium dependence of vesicle recruitment. *J Physiol (Lond)* 596, 4693–4707.
1135 doi:10.1113/JP275911
- 1136 Rodal, A.A., Blunk, A.D., Akbergenova, Y., Jorquera, R.A., Buhl, L.K., Littleton, J.T., 2011. A
1137 presynaptic endosomal trafficking pathway controls synaptic growth signaling. *J Cell Biol*
1138 193, 201–217. doi:10.1083/jcb.201009052

- 1139 Rodal, A.A., Motola-Barnes, R.N., Littleton, J.T., 2008. Nervous wreck and Cdc42 cooperate to
1140 regulate endocytic actin assembly during synaptic growth. *J Neurosci* 28, 8316–8325.
1141 doi:10.1523/JNEUROSCI.2304-08.2008
- 1142 Rozov, A., Bolshakov, A.P., Valiullina-Rakhmatullina, F., 2019. The Ever-Growing Puzzle of
1143 Asynchronous Release. *Front Cell Neurosci* 13, 28. doi:10.3389/fncel.2019.00028
- 1144 Sabatini, B.L., Regehr, W.G., 1996. Timing of neurotransmission at fast synapses in the
1145 mammalian brain. *Nature* 384, 170–172. doi:10.1038/384170a0
- 1146 Sabeva, N., Cho, R.W., Vasin, A., Gonzalez, A., Littleton, J.T., Bykhovskaia, M., 2017.
1147 Complexin Mutants Reveal Partial Segregation between Recycling Pathways That Drive
1148 Evoked and Spontaneous Neurotransmission. *J Neurosci* 37, 383–396.
1149 doi:10.1523/JNEUROSCI.1854-16.2016
- 1150 Saraswati, S., Adolfsen, B., Littleton, J.T., 2007. Characterization of the role of the Synaptotagmin
1151 family as calcium sensors in facilitation and asynchronous neurotransmitter release. *Proc*
1152 *Natl Acad Sci U S A* 104, 14122–14127. doi:10.1073/pnas.0706711104
- 1153 Schmid, B., Schindelin, J., Cardona, A., Longair, M., Heisenberg, M., 2010. A high-level 3D
1154 visualization API for Java and ImageJ. *BMC Bioinformatics* 11, 274. doi:10.1186/1471-
1155 2105-11-274
- 1156 Schneggenburger, R., Rosenmund, C., 2015. Molecular mechanisms governing Ca(2+) regulation
1157 of evoked and spontaneous release. *Nat Neurosci* 18, 935–941. doi:10.1038/nn.4044
- 1158 Schonh, J.-S., Maximov, A., Lao, Y., Südhof, T.C., Sørensen, J.B., 2008. Synaptotagmin-1 and -
1159 7 are functionally overlapping Ca²⁺ sensors for exocytosis in adrenal chromaffin cells.
1160 *Proc Natl Acad Sci U S A* 105, 3998–4003. doi:10.1073/pnas.0712373105
- 1161 Shin, O.-H., Rizo, J., Südhof, T.C., 2002. Synaptotagmin function in dense core vesicle exocytosis
1162 studied in cracked PC12 cells. *Nat Neurosci* 5, 649–656. doi:10.1038/nn869
- 1163 Shupliakov, O., Haucke, V., Pechstein, A., 2011. How synapsin I may cluster synaptic vesicles.
1164 *Semin Cell Dev Biol* 22, 393–399. doi:10.1016/j.semcdb.2011.07.006
- 1165 Söllner, T., Whiteheart, S.W., Brunner, M., Erdjument-Bromage, H., Geromanos, S., Tempst, P.,
1166 Rothman, J.E., 1993. SNAP receptors implicated in vesicle targeting and fusion. *Nature*
1167 362, 318–324. doi:10.1038/362318a0
- 1168 Sone, M., Suzuki, E., Hoshino, M., Hou, D., Kuromi, H., Fukata, M., Kuroda, S., Kaibuchi, K.,
1169 Nabeshima, Y., Hama, C., 2000. Synaptic development is controlled in the periaxonal zones
1170 of *Drosophila* synapses. *Development* 127, 4157–4168.
- 1171 Südhof, T.C., 2012. Calcium control of neurotransmitter release. *Cold Spring Harb Perspect Biol*
1172 4, a011353. doi:10.1101/cshperspect.a011353
- 1173 Südhof, T.C., 2013. Neurotransmitter release: the last millisecond in the life of a synaptic vesicle.
1174 *Neuron* 80, 675–690. doi:10.1016/j.neuron.2013.10.022
- 1175 Sugita, S., Han, W., Butz, S., Liu, X., Fernández-Chacón, R., Lao, Y., Südhof, T.C., 2001.
1176 Synaptotagmin VII as a plasma membrane Ca(2+) sensor in exocytosis. *Neuron* 30, 459–
1177 473. doi:10.1016/s0896-6273(01)00290-2
- 1178 Sugita, S., Shin, O.-H., Han, W., Lao, Y., Südhof, T.C., 2002. Synaptotagmins form a hierarchy
1179 of exocytotic Ca(2+) sensors with distinct Ca(2+) affinities. *EMBO J* 21, 270–280.
1180 doi:10.1093/emboj/21.3.270
- 1181 Sutton, R.B., Fasshauer, D., Jahn, R., Brunger, A.T., 1998. Crystal structure of a SNARE complex
1182 involved in synaptic exocytosis at 2.4 Å resolution. *Nature* 395, 347–353.
1183 doi:10.1038/26412
- 1184 Tsuboi, T., Fukuda, M., 2007. Synaptotagmin VII modulates the kinetics of dense-core vesicle

- 1185 exocytosis in PC12 cells. *Genes Cells* 12, 511–519. doi:10.1111/j.1365-
1186 2443.2007.01070.x
- 1187 Tucker, W.C., Weber, T., Chapman, E.R., 2004. Reconstitution of Ca²⁺-regulated membrane
1188 fusion by synaptotagmin and SNAREs. *Science* 304, 435–438.
1189 doi:10.1126/science.1097196
- 1190 Turecek, J., Regehr, W.G., 2018. Synaptotagmin 7 mediates both facilitation and asynchronous
1191 release at granule cell synapses. *J Neurosci* 38, 3240–3251.
1192 doi:10.1523/JNEUROSCI.3207-17.2018
- 1193 Turecek, J., Regehr, W.G., 2019. Neuronal regulation of fast synaptotagmin isoforms controls the
1194 relative contributions of synchronous and asynchronous release. *Neuron* 101, 938–949.e4.
1195 doi:10.1016/j.neuron.2019.01.013
- 1196 Ullrich, B., Südhof, T.C., 1995. Differential distributions of novel synaptotagmins: comparison to
1197 synapsins. *Neuropharmacology* 34, 1371–1377. doi:10.1016/0028-3908(95)00132-P
- 1198 Uytterhoeven, V., Kuenen, S., Kasprowicz, J., Miskiewicz, K., Verstreken, P., 2011. Loss of
1199 skywalker reveals synaptic endosomes as sorting stations for synaptic vesicle proteins. *Cell*
1200 145, 117–132. doi:10.1016/j.cell.2011.02.039
- 1201 Virmani, T., Han, W., Liu, X., Südhof, T.C., Kavalali, E.T., 2003. Synaptotagmin 7 splice variants
1202 differentially regulate synaptic vesicle recycling. *EMBO J* 22, 5347–5357.
1203 doi:10.1093/emboj/cdg514
- 1204 Voleti, R., Tomchick, D.R., Südhof, T.C., Rizo, J., 2017. Exceptionally tight membrane-binding
1205 may explain the key role of the synaptotagmin-7 C2A domain in asynchronous
1206 neurotransmitter release. *Proc Natl Acad Sci U S A* 114, E8518–E8527.
1207 doi:10.1073/pnas.1710708114
- 1208 Wadel, K., Neher, E., Sakaba, T., 2007. The coupling between synaptic vesicles and Ca²⁺
1209 channels determines fast neurotransmitter release. *Neuron* 53, 563–575.
1210 doi:10.1016/j.neuron.2007.01.021
- 1211 Wagh, D.A., Rasse, T.M., Asan, E., Hofbauer, A., Schwenkert, I., Dürrbeck, H., Buchner, S.,
1212 Dabauvalle, M.-C., Schmidt, M., Qin, G., Wichmann, C., Kittel, R., Sigrist, S.J., Buchner,
1213 E., 2006. Bruchpilot, a protein with homology to ELKS/CAST, is required for structural
1214 integrity and function of synaptic active zones in *Drosophila*. *Neuron* 49, 833–844.
1215 doi:10.1016/j.neuron.2006.02.008
- 1216 Walsh, R.B., Becalska, A.N., Zunitch, M.J., Wang, S., Isaac, B., Yeh, A., Koles, K., Rodal, A.A.,
1217 2019. Opposing functions for retromer and Rab11 in extracellular vesicle cargo traffic at
1218 synapses. *BioRxiv*. doi:10.1101/645713
- 1219 Wang, S., Li, Y., Ma, C., 2016. Synaptotagmin-1 C2B domain interacts simultaneously with
1220 SNAREs and membranes to promote membrane fusion. *elife* 5. doi:10.7554/eLife.14211
- 1221 Waterhouse, A., Bertoni, M., Bienert, S., Studer, G., Tauriello, G., Gumienny, R., Heer, F.T., de
1222 Beer, T.A.P., Rempfer, C., Bordoli, L., Lepore, R., Schwede, T., 2018. SWISS-MODEL:
1223 homology modelling of protein structures and complexes. *Nucleic Acids Res* 46, W296–
1224 W303. doi:10.1093/nar/gky427
- 1225 Weber, J.P., Toft-Bertelsen, T.L., Mohrmann, R., Delgado-Martinez, I., Sørensen, J.B., 2014.
1226 Synaptotagmin-7 is an asynchronous calcium sensor for synaptic transmission in neurons
1227 expressing SNAP-23. *PLoS ONE* 9, e114033. doi:10.1371/journal.pone.0114033
- 1228 Wen, H., Linhoff, M.W., McGinley, M.J., Li, G.-L., Corson, G.M., Mandel, G., Brehm, P., 2010.
1229 Distinct roles for two synaptotagmin isoforms in synchronous and asynchronous
1230 transmitter release at zebrafish neuromuscular junction. *Proc Natl Acad Sci U S A* 107,

- 1231 13906–13911. doi:10.1073/pnas.1008598107
- 1232 Winther, Å.M.E., Vorontsova, O., Rees, K.A., Näreoja, T., Sopova, E., Jiao, W., Shupliakov, O.,
1233 2015. An Endocytic Scaffolding Protein together with Synapsin Regulates Synaptic
1234 Vesicle Clustering in the *Drosophila* Neuromuscular Junction. *J Neurosci* 35, 14756–
1235 14770. doi:10.1523/JNEUROSCI.1675-15.2015
- 1236 Wu, B., Wei, S., Petersen, N., Ali, Y., Wang, X., Bacaj, T., Rorsman, P., Hong, W., Südhof, T.C.,
1237 Han, W., 2015. Synaptotagmin-7 phosphorylation mediates GLP-1-dependent potentiation
1238 of insulin secretion from β -cells. *Proc Natl Acad Sci U S A* 112, 9996–10001.
1239 doi:10.1073/pnas.1513004112
- 1240 Xu, J., Mashimo, T., Südhof, T.C., 2007. Synaptotagmin-1, -2, and -9: Ca(2+) sensors for fast
1241 release that specify distinct presynaptic properties in subsets of neurons. *Neuron* 54, 567–
1242 581. doi:10.1016/j.neuron.2007.05.004
- 1243 Xue, M., Craig, T.K., Shin, O.-H., Li, L., Brautigam, C.A., Tomchick, D.R., Südhof, T.C.,
1244 Rosenmund, C., Rizo, J., 2010. Structural and mutational analysis of functional
1245 differentiation between synaptotagmins-1 and -7. *PLoS ONE* 5.
1246 doi:10.1371/journal.pone.0012544
- 1247 Yang, X., Kaeser-Woo, Y.J., Pang, Z.P., Xu, W., Südhof, T.C., 2010. Complexin clamps
1248 asynchronous release by blocking a secondary Ca(2+) sensor via its accessory α helix.
1249 *Neuron* 68, 907–920. doi:10.1016/j.neuron.2010.11.001
- 1250 Yoshihara, M., Adolfsen, B., Galle, K.T., Littleton, J.T., 2005. Retrograde signaling by Syt 4
1251 induces presynaptic release and synapse-specific growth. *Science* 310, 858–863.
1252 doi:10.1126/science.1117541
- 1253 Yoshihara, M., Guan, Z., Littleton, J.T., 2010. Differential regulation of synchronous versus
1254 asynchronous neurotransmitter release by the C2 domains of synaptotagmin 1. *Proc Natl*
1255 *Acad Sci U S A* 107, 14869–14874. doi:10.1073/pnas.1000606107
- 1256 Yoshihara, M., Littleton, J.T., 2002. Synaptotagmin I functions as a calcium sensor to synchronize
1257 neurotransmitter release. *Neuron* 36, 897–908.
- 1258 Young, S.M., Neher, E., 2009. Synaptotagmin has an essential function in synaptic vesicle
1259 positioning for synchronous release in addition to its role as a calcium sensor. *Neuron* 63,
1260 482–496. doi:10.1016/j.neuron.2009.07.028
- 1261 Zhai, R.G., Bellen, H.J., 2004. The architecture of the active zone in the presynaptic nerve
1262 terminal. *Physiology (Bethesda)* 19, 262–270. doi:10.1152/physiol.00014.2004
- 1263 Zhang, J., Schulze, K.L., Hiesinger, P.R., Suyama, K., Wang, S., Fish, M., Acar, M., Hoskins,
1264 R.A., Bellen, H.J., Scott, M.P., 2007. Thirty-one flavors of *Drosophila* rab proteins.
1265 *Genetics* 176, 1307–1322. doi:10.1534/genetics.106.066761
- 1266 Zhao, H., Ito, Y., Chappel, J., Andrews, N.W., Teitelbaum, S.L., Ross, F.P., 2008. Synaptotagmin
1267 VII regulates bone remodeling by modulating osteoclast and osteoblast secretion. *Dev Cell*
1268 14, 914–925. doi:10.1016/j.devcel.2008.03.022
- 1269 Zhou, Q., Lai, Y., Bacaj, T., Zhao, M., Lyubimov, A.Y., Uervirojnangkoorn, M., Zeldin, O.B.,
1270 Brewster, A.S., Sauter, N.K., Cohen, A.E., Soltis, S.M., Alonso-Mori, R., Chollet, M.,
1271 Lemke, H.T., Pfuetzner, R.A., Choi, U.B., Weis, W.I., Diao, J., Südhof, T.C., Brunger,
1272 A.T., 2015. Architecture of the synaptotagmin-SNARE machinery for neuronal exocytosis.
1273 *Nature* 525, 62–67. doi:10.1038/nature14975
- 1274 Zucker, R.S., Regehr, W.G., 2002. Short-term synaptic plasticity. *Annu Rev Physiol* 64, 355–405.
1275 doi:10.1146/annurev.physiol.64.092501.114547
- 1276

1277 **Figure Legends**

1278

1279 **Figure 1.** SYT1 and SYT7 comparison and generation of *Syt7* mutants. **(A)** Proposed roles for
1280 SYT7 in Ca²⁺-regulated membrane trafficking. **(B)** Phylogenetic tree of SYT1, SYT7 and E-SYT2
1281 from the indicated species generated using the BLOSUM62 matrix with neighbor joining
1282 clustering. **(C)** Comparison of the structure of the C2A and C2B domains of *R. norvegicus* SYT1
1283 (magenta) with a homology model of *D. melanogaster* SYT7 (blue). The C2B residues that form
1284 the SYT1-SNARE complex primary binding site are highlighted in yellow, with the counterpart
1285 changes noted in SYT7. The C2B HB helix in SYT1 is highlighted in green and missing from
1286 SYT7. **(D)** Diagram of the *Syt7* genomic locus on chromosome 4 with coding exons indicated with
1287 boxes. Exon 1 (teal) encodes the intravesicular and transmembrane (TM) domains; exons 2 and 3
1288 (white) encode the linker region; exons 4 and 5 encode the C2A domain (dark blue); and exons 6
1289 and 7 encode the C2B domain (light blue). The location of the *Syt7*^{M2} Minos transposon insertion
1290 in exon 2 is indicated in red. Sequence of the *Syt7*^{M1} CRISPR mutant versus control is shown
1291 below with the start codon in green. The guide RNA sequence used to target *Syt7* is bolded, with
1292 the cleavage site noted by the red arrowhead and the deleted cytosine with a red dash. **(E)** Western
1293 of SYT7 protein levels in head extracts of *white*, CRISPR control, *Syt7*^{M1}, *Syt7*^{M2} and *elav*^{C155}-
1294 GAL4; UAS-*Syt7* (OE SYT7) with anti-SYT7 antisera (top panel). Syntaxin 1 (SYX1) antisera
1295 was used as a loading control (bottom panel). SYT7 is overexpressed 2.48 ± 0.4-fold compared to
1296 controls (p<0.05, Mann-Whitney unpaired t-test, n=4).

1297

1298 **Figure 1 – figure supplement 1.** SYT1 and SYT7 sequence comparisons. Annotated sequence
1299 alignment of the C2A Ca²⁺ binding loops and the C2B domain of SYT1 and SYT7 from the
1300 indicated species. Conserved residues are shaded dark blue, with conservative amino acid
1301 substitutions in light blue. Grey shading denotes subfamily-specific residue conservation in only
1302 SYT1 or SYT7. C2A and C2B Ca²⁺ binding residues are shaded red. Yellow circles denote
1303 residues that form the primary SYT1-SNARE complex binding interface. Four of the five residues
1304 are not conserved in *Drosophila* SYT7, with two containing identical substitutions previously
1305 found to abolish SYT1 function (R334H and E348K).

1306

1307 **Figure 2.** *Syt7* mutants and *Syt7*/*+* heterozygotes display enhanced neurotransmitter release. **(A)**
1308 Average mEJC traces in control (black), *Syt7^{MI}/+* (green) and *Syt7^{MI}* mutants (blue). **(B)**
1309 Quantification of mean mEJC amplitude for the indicated genotypes (control: 0.62 ± 0.020 nA,
1310 $n=17$; *Syt7^{MI}/+*: 0.61 ± 0.021 nA, $n=21$; *Syt7^{MI}*: 0.57 ± 0.013 nA, $n=20$). **(C)** Normalized
1311 cumulative mEJC charge for each genotype. **(D)** Quantification of mean mEJC frequency for the
1312 indicated genotypes (control: 1.30 ± 0.10 Hz, $n=17$; *Syt7^{MI}/+*: 1.66 ± 0.13 Hz, $n=19$; *Syt7^{MI}*: 1.36
1313 ± 0.12 Hz, $n=19$). **(E)** Average eEJC traces in control (black), *Syt7^{MI}/+* (green) and *Syt7^{MI}* (blue).
1314 **(F)** Quantification of mean eEJC amplitude for the indicated genotypes. **(G)** Average normalized
1315 responses for each genotype plotted on a semi-logarithmic graph to display release components.
1316 **(H)** Cumulative release normalized to the maximum response in 2 mM Ca^{2+} for each genotype. **(I)**
1317 Quantification of mean eEJC rise time in the indicated genotypes (control: 1.09 ± 0.08 ms, $n=9$;
1318 *Syt7^{MI}/+*: 1.06 ± 0.09 ms, $n=14$; *Syt7^{MI}*: 1.03 ± 0.08 ms, $n=10$). **(J)** Quantification of mean eEJC
1319 half-width in the indicated genotypes (control: 7.81 ± 0.47 ms, $n=9$; *Syt7^{MI}/+*: 7.77 ± 0.26 ms,
1320 $n=14$; *Syt7^{MI}*: 7.15 ± 0.34 ms, $n=10$). **(K)** Quantification of evoked quantal content with mEJC
1321 amplitude for the indicated genotypes (control: 250.1 ± 30.58 SVs, $n=9$; *Syt7^{MI}/+*: 377.9 ± 31.13 ,
1322 $n=14$; *Syt7^{MI}*: 495.3 ± 36.75 , $n=10$). **(L)** Quantification of evoked quantal content with mEJC
1323 charge for the indicated genotypes (control: 221.3 ± 20.54 SVs, $n=9$; *Syt7^{MI}/+*: 371.6 ± 43.56 ,
1324 $n=14$; *Syt7^{MI}*: 503.6 ± 31.99 , $n=10$). Recordings were performed from 3rd instar segment A3
1325 muscle 6 in 2 mM Ca^{2+} . Statistical significance for all comparisons was determined using one-way
1326 ANOVA (nonparametric) with post hoc Tukey's multiple comparisons test. N.S. = no significant
1327 change. Error bars represent SEM.

1328
1329 **Figure 3.** Neuronal overexpression of SYT7 reduces spontaneous and evoked SV release. **(A)**
1330 Average mEJC traces in control (black) and *elav^{C155}-GAL4; UAS-Syt7* (OE SYT7, magenta). **(B)**
1331 Quantification of mean mEJC amplitudes in the indicated genotypes (control: 0.66 ± 0.03 nA, $n=9$;
1332 OE SYT7: 0.73 ± 0.03 nA, $n=8$). **(C)** Quantification of mean mEJC frequency in the indicated
1333 genotypes (control: 2.81 ± 0.42 Hz, $n=9$; OE SYT7: 1.45 ± 0.18 Hz, $n=8$). **(D)** Average eEJC traces
1334 in control (black) and *elav^{C155}-GAL4; UAS-Syt7* (OE SYT7, magenta). **(E)** Quantification of mean
1335 eEJC amplitudes in the indicated genotypes (control: 256.24 ± 22.38 nA, $n=10$; OE SYT7: 166.66
1336 ± 10.74 nA, $n=7$). **(F)** Quantification of mean eEJC charge in the indicated genotypes (control:
1337 $2.5 \times 10^3 \pm 0.25 \times 10^3$ nA*ms, $n=10$; OE SYT7: $1.4 \times 10^3 \pm 0.12 \times 10^3$ nA*ms, $n=7$). **(G)** Average

1338 normalized responses for each genotype plotted on a semi-logarithmic graph to display release
1339 components. Recordings were performed from 3rd instar segment A3 muscle 6 in 2 mM Ca²⁺.
1340 Statistical significance was determined with a Mann-Whitney unpaired t-test.

1341
1342 **Figure 3 – figure supplement 1.** Overexpression of SYT7 in postsynaptic muscles does not
1343 disrupt synaptic transmission. **(A)** Average eEJC traces in control (black) and *Mhc-GAL4; UAS-*
1344 *Syt7* (OE SYT7, orange). **(B)** Quantification of mean eEJC amplitudes in the indicated genotypes
1345 (control: 252.82 ± 10.98 nA, n=12; *Mhc-GAL4; UAS-Syt7*: 243.91 ± 7.46 nA, n=16). Recordings
1346 were performed from 3rd instar segment A3 muscle 6 in 2 mM Ca²⁺. Statistical significance was
1347 determined with the Mann-Whitney unpaired test.

1348
1349 **Figure 4.** Analysis of synaptic morphology in *Syt7* mutants. **(A, B)** Immunocytochemistry of 3rd
1350 instar muscle 6/7 NMJs with anti-HRP (blue), anti-CPX (magenta) and anti-BRP (green) in control
1351 and *Syt7^{MI}*. The boxed region is magnified below with channels showing BRP, CPX and the merge.
1352 Scale bar = 20 μm for large panels and 2 μm for boxed regions. Synaptic morphology was
1353 quantified for 3rd instar muscle 6/7 **(C-E)** and muscle 4 **(F-H)** in controls and *Syt7^{MI}* mutants. No
1354 significant differences were detected in synaptic bouton number **(C, F;** muscle 6/7: p = 0.78;
1355 control: 81.87 ± 5.301, n=15; *Syt7^{MI}*: 79.60 ± 5.824, n=15; muscle 4: p = 0.24; control: 55.86 ±
1356 3.141, n=14; *Syt7^{MI}*: 62.50 ± 4.575, n=14), BRP puncta **(D, G,** muscle 6/7: p = 0.94; control: 621.1
1357 ± 26.28, n=15; *Syt7^{MI}*: 618.1 ± 25.73, n=15; muscle 4: p = 0.83; control: 450.5 ± 23.25, n=14;
1358 *Syt7^{MI}*: 443.5 ± 21.47, n=14) or BRP puncta per muscle surface area **(E, H,** muscle 6/7: p = 0.13;
1359 control: 0.0088 ± 0.0004, n=15; *Syt7^{MI}*: 0.0098 ± 0.0005, n=15; muscle 4: p = 0.88; control:
1360 0.0105 ± 0.0008, n=14; *Syt7^{MI}*: 0.0107 ± 0.0007, n=14). **(I)** Anti-BRP staining at 3rd instar muscle
1361 4 in control and *Syt7^{MI}* imaged with SIM microscopy. Scale bar = 1 μm. **(J)** Relative cumulative
1362 frequency of AZ T-bar volume defined with anti-BRP staining at 3rd instar muscle 6/7 NMJs (p =
1363 0.026; control: 0.055 ± 0.004 μm², n = 19 NMJs from 5 larvae; *Syt7^{MI}*: 0.044 ± 0.003 μm², n=15
1364 NMJs from 4 larvae). **(K)** Relative cumulative frequency of T-bar spacing defined by distance
1365 between nearest BRP puncta at 3rd instar muscle 6/7 NMJs (p = 0.48; control: 0.28 ± 0.016 μm,
1366 n=20 NMJs from 5 larvae; *Syt7^{MI}*: 0.27 ± 0.014 μm, n=15 NMJs from 4 larvae). Statistical
1367 significance was determined with Student's t-test.

1368

1369 **Figure 5.** Ultrastructural analysis of SV distribution in *Syt7* mutants. **(A)** Representative EM
1370 micrographs of muscle 6/7 synaptic boutons in control and *Syt7^{M1}* 3rd instar larvae. An AZ with its
1371 associated electron dense T-bar is denoted with an arrowhead in each micrograph. **(B)**
1372 Quantification of SV density ($p = 0.41$; control = 0.34 ± 0.033 SVs/ μm^2 , $n = 20$; *Syt7^{M1}* = $0.30 \pm$
1373 0.031 SVs/ μm^2 , $n = 20$). **(C)** Quantification of AZ length defined by the electron dense synaptic
1374 cleft ($p=0.93$; control: 404 ± 34.5 nm, $n=21$ AZs from 5 larvae; *Syt7^{M1}*: 409 ± 28.9 nm, $n=29$ AZs
1375 from 5 larvae). **(D)** Quantification of SVs docked within 100 nm of the T-bar ($p = 0.41$; control =
1376 1.69 ± 0.15 SVs $n = 84$; *Syt7^{M1}* = 1.43 ± 0.15 SVs, $n = 58$). **(E)** Quantification of SVs docked
1377 within 100 - 400 nm of the T-bar ($p = 0.68$; control = 2.46 ± 0.17 SVs $n = 84$; *Syt7^{M1}* = 2.35 ± 0.25
1378 SVs, $n = 58$). **(F)** Quantification of all docked SVs at 0-400 nm from the T-bar ($p = 0.31$; control
1379 = 4.16 ± 0.23 SVs $n = 84$; *Syt7^{M1}* = 3.78 ± 0.29 SVs, $n = 58$). **(G)** Quantification of all SVs within
1380 a 400 nm radius from the T-bar ($p = 0.38$; control = 71.98 ± 4.05 SVs $n = 84$; *Syt7^{M1}* = $78.12 \pm$
1381 5.89 SVs, $n = 58$). **(H)** Quantification of SV distribution at AZs in control and *Syt7^{M1}* mutants.
1382 Statistical significance was determined with Student's t-test.

1383
1384 **Figure 6.** Quantal imaging reveals elevated release probability across the AZ population in *Syt7*
1385 mutants. **(A)** P_r heatmaps for muscle 4 NMJs generated following 0.3 Hz stimulation for 5 minutes
1386 in control and *Syt7^{M1}* mutants. The P_r color map is displayed in the upper right. **(B)** Frequency
1387 distribution of AZ P_r after a 0.3 Hz 5-minute stimulation for control (black dashed line) and *Syt7^{M1}*
1388 (blue line). **(C)** Quantification of mean AZ P_r for the two genotypes ($p \leq 0.01$, Student's t-test;
1389 control: 0.063 ± 0.002 , $n=1158$; *Syt7^{M2}*: 0.12 ± 0.004 , $n=768$).

1390
1391 **Figure 7.** Loss of SYT7 enhances the residual release observed in *Syt1* null mutants. **(A)** Western
1392 of head extracts from control, *Syt7^{M2}*, *Syt1^{Null}* and *Syt1^{null}*; *Syt7^{M2}* (*Double^{Null}*) probed with anti-
1393 SYT7, anti-SYT1 and anti-SYX1 (loading control). SYT1 migrates as a doublet at 55 and 70 kD
1394 (Littleton et al., 1993a). **(B)** Average mEJC traces in *Syt1^{Null}* (black trace) and *Double^{Null}* (red trace)
1395 mutants obtained by summing all mEPSC events under the first peak distribution. **(C)**
1396 Quantification of mean mEJC frequency for the indicated genotypes. **(D)** Average eEJC traces in
1397 *Syt1^{Null}* (black trace) and *Double^{Null}* (red trace). **(E)** Quantification of mean eEJC amplitude for the
1398 indicated genotypes. **(F)** Quantification of mean eEJC charge for the indicated genotypes obtained
1399 by measuring total release over time. **(G)** Average normalized responses for each genotype plotted

1400 on a semi-logarithmic graph to display release components. **(H)** Cumulative release normalized to
1401 the maximum response in 2 mM Ca^{2+} for each genotype. Each trace was adjusted to a double
1402 exponential fit. **(I)** Quantification of eEJC failure ratio (%) in the indicated genotypes. Recordings
1403 were performed from 3rd instar segment A3 muscle 6 in 2 mM extracellular Ca^{2+} . Statistical
1404 significance was determined with the Mann-Whitney unpaired t-test.

1405

1406 **Figure 8.** Short-term synaptic facilitation can occur without SYT7 or SYT1. **(A)** Quantification of
1407 eEJC failure ratio (%) in the indicated genotypes. **(B)** Average eEJC traces recorded in 0.175 mM
1408 Ca^{2+} (control, grey; *Syt7^{MI}*, light blue) or 0.2 mM Ca^{2+} (control, black; *Syt7^{MI}*, dark blue). **(C)**
1409 Quantification of mean eEJC amplitude for the indicated genotypes (0.175 mM Ca^{2+} : control, 5.42
1410 \pm 2.0 nA, n=7; *Syt7^{MI}*, 8.70 \pm 1.6 nA, n=14; 0.2 mM Ca^{2+} : control, 7.73 \pm 1.5 nA, n=9; *Syt7^{MI}*,
1411 23.72 \pm 6.2 nA, n=9). **(D)** Representative eEJC traces to 10 ms or 50 ms paired-pulse stimuli
1412 recorded in 0.2 mM Ca^{2+} (control, black; *Syt7^{MI}*, dark blue) or 0.175 mM Ca^{2+} (*Syt7^{MI}*, light blue).
1413 **(E)** Quantification of facilitation (P2/P1) at 10 ms interval for the indicated genotypes (0.2 mM
1414 Ca^{2+} : 1.93 \pm 0.095, n=9; *Syt7^{MI}*, 1.28 \pm 0.12, n=9; 0.175 mM Ca^{2+} : *Syt7^{MI}*, 1.47 \pm 0.11, n=12). **(F)**
1415 Quantification of facilitation (P2/P1) at 50 ms interval for the indicated genotypes (0.2 mM Ca^{2+} :
1416 control, 1.64 \pm 0.043, n=9; *Syt7^{MI}*, 1.23 \pm 0.056, n=9; 0.175 mM Ca^{2+} : *Syt7^{MI}*, 1.34 \pm 0.054, n=12).
1417 Statistical significance was determined using one-way ANOVA (nonparametric) with post hoc
1418 Tukey's multiple comparisons test for panels A-F. **(G)** Average eEJC quantal content determined
1419 from mEJC charge in 2 mM Ca^{2+} during a 10 Hz stimulation paradigm (30 stimuli at 0.5 Hz, 500
1420 stimuli at 10 Hz, and return to 0.5 Hz) in *Syt1^{Null}* (black) and *Double^{Null}* (red). **(H)** Average quantal
1421 content for the last four responses of 0.5 Hz stimulation and the first 14 responses during 10 Hz
1422 stimulation in *Syt1^{Null}* (black) and *Double^{Null}* (red). P1 denotes the 1st response and P2 the 2nd
1423 response to 10 Hz stimulation. **(I)** Quantification of P2/P1 ratio in *Syt1^{Null}* (black, 1.15 \pm 0.089,
1424 n=12) and *Double^{Null}* (red, 1.55 \pm 0.22, n=13) at onset of 10 Hz stimulation. Statistical significance
1425 was determined with a Mann-Whitney unpaired t-test for panels H and I.

1426

1427 **Figure 9.** *Syt7* mutants have a larger releasable pool of SVs and normal endocytosis. **(A)**
1428 Representative mean eEJC quantal content determined by mEJC charge during 1000 stimuli at 10
1429 Hz in 2 mM Ca^{2+} in control (black) and *Syt7^{MI}* (blue). The inset shows representative eEJC traces
1430 in control (black) and *Syt7^{MI}* (blue). **(B)** Quantification of average cumulative quanta released

1431 during the 1000 stimuli at 10 Hz tetanic stimulation in control (black, $19.21K \pm 2.88K$, $n=7$) and
1432 *Syt7^{MI}* (blue, $36.18K \pm 5.67K$, $n=8$). (C) Quantification of average quantal content at steady-state
1433 release at the end of the 10 Hz stimulation in control (black, 131.54 ± 10.71 , $n=7$) and *Syt7^{MI}* (blue,
1434 123.05 ± 10.47 , $n=8$). Statistical significance for B and C was determined with a Mann-Whitney
1435 unpaired t-test. (D) FM1-43 loading in control and *Syt7^{MI}* larvae at muscle 6/7 NMJs in 2 mM
1436 Ca^{2+} following 150, 300 or 600 stimuli delivered at 0.5 Hz. (E) FM1-43 loading with 500 stimuli
1437 at 10 Hz in 2 mM Ca^{2+} and FM1-43 unloading with high K^+ (90 mM) in control and *Syt7^{MI}* larvae
1438 at muscle 6/7 NMJs. (F) Quantification of FM1-43 loading following 150, 300 or 600 stimuli
1439 delivered at 0.5 Hz. (G) Quantification of FM1-43 loading after 500 stimuli at 10 Hz. (H)
1440 Quantification of FM1-43 unloading with high K^+ (90 mM). Statistical significance was
1441 determined with Student's t-test for F-H. Scale bar = 5 μ m.

1442

1443 **Figure 10.** *Syt7* mutants have enhanced refilling of the RRP that does not require endocytosis. (A)
1444 Average eEJC quantal content during the indicated stimulation protocol in 2 mM external Ca^{2+} for
1445 control (black), *Syt7^{MI/+}* (green) and *Syt7^{MI}* (blue). (B) Quantification of P2/P1 ratio (P1 = 1st
1446 response to 10 Hz, P2 = 2nd response to 10 Hz) in control (black, 1.13 ± 0.03 , $n=8$), *Syt7^{MI/+}* (green,
1447 0.95 ± 0.009 , $n=14$) and *Syt7^{MI}* (blue, 0.82 ± 0.01 , $n=8$). Representative eEJC traces of P1 and P2
1448 for control (black) and *Syt7^{MI}* (blue) are shown on the right. (C) Quantification of P531/P530 ratio
1449 (P530 is the last response to 10 Hz and P531 is the 1st response to 0.5 Hz stimulation delivered 2
1450 seconds after P530) in control (black, 0.93 ± 0.06 , $n=8$), *Syt7^{MI/+}* (green, 1.33 ± 0.04 , $n=12$) and
1451 *Syt7^{MI}* (blue, 1.91 ± 0.09 , $n=8$). Representative eEJC traces of P530 and P531 for control (black)
1452 and *Syt7^{MI}* (blue) are shown on the right. (D) Representative eEJC traces for control with DMSO
1453 (black) or 4 μ M bafilomycin (gray) and *Syt7^{MI}* with DMSO (dark blue) or 4 μ M bafilomycin (light
1454 blue) in 2 mM external Ca^{2+} with the indicated stimulation protocol repeated three times. (E)
1455 Quantification of P531/P530 for the indicated genotypes (1st stimulation protocol: Control +
1456 DMSO, 0.98 ± 0.056 , $n=17$; Control + bafilomycin, 1.53 ± 0.12 , $n=17$; *Syt7^{MI}* + DMSO, $1.83 \pm$
1457 0.058 , $n=17$; *Syt7^{MI}* + bafilomycin, 2.10 ± 0.11 , $n=17$; 2nd stimulation protocol: Control + DMSO,
1458 0.97 ± 0.045 , $n=17$; Control + bafilomycin, 1.25 ± 0.064 , $n=17$; *Syt7^{MI}* + DMSO, 1.95 ± 0.10 ,
1459 $n=17$; *Syt7^{MI}* + bafilomycin, 2.09 ± 0.19 , $n=17$). Statistical significance was determined with a
1460 one-way Anova with Sidak's multiple comparisons test. (F) Quantification of mean eEJC
1461 amplitudes for P530 and P531 for the indicated genotypes (1st stimulation protocol: P530 in

1462 Control + DMSO, 87.39 ± 3.85 , n=17; P531 in Control + DMSO, 80.22 ± 5.25 , n=17; P530 in
1463 Control + bafilomycin, 44.68 ± 2.80 , n=17; P531 in Control + bafilomycin, 66.26 ± 5.03 , n=17;
1464 P530 in *Syt7^{MI}* + DMSO, 97.62 ± 4.04 , n=17; P531 in *Syt7^{MI}* + DMSO, 177.34 ± 7.80 , n=17; P530
1465 in *Syt7^{MI}* + bafilomycin, 52.44 ± 3.83 , n=17; P531 in *Syt7^{MI}* + bafilomycin, 102.50 ± 8.07 , n=17;
1466 2nd stimulation protocol: P530 in Control + DMSO, 68.21 ± 3.97 , n=17; P531 in Control + DMSO,
1467 70.05 ± 5.95 , n=17; P530 in Control + bafilomycin, 15.09 ± 1.26 , n=17; P531 in Control +
1468 bafilomycin, 18.15 ± 1.34 , n=17; P531 in *Syt7^{MI}* + DMSO, 82.89 ± 4.64 , n=17; P531 in *Syt7^{MI}* +
1469 DMSO, 163.52 ± 9.74 , n=17; P530 in *Syt7^{MI}* + bafilomycin, 11.98 ± 1.26 , n=17; P531 in *Syt7^{MI}* +
1470 bafilomycin, 24.71 ± 3.00 , n=17). Statistical significance was determined with a Student's paired
1471 t-test.

1472
1473 **Figure 10 – figure supplement 1.** Enhanced recovery after termination of 10 Hz stimulation in
1474 *Syt7* mutants. (A) Average eEJC quantal content to 2000 stimuli at 10 Hz stimulation at 3rd instar
1475 segment A3 muscle 6 in 2 mM external Ca²⁺ for control (black) and *Syt7^{MI}* (blue). (B)
1476 Representative average quantal content of the last 3 responses to 10 Hz and the 1st 12 responses to
1477 0.5 Hz stimulation. P2000 = last response to 10 Hz stimulation, P2001 = 1st response to 0.5 Hz
1478 stimulation 2 seconds after P2000. (C) Quantification of P2001/P2000 ratio for control (black,
1479 0.90 ± 0.03 , n=9) and *Syt7^{MI}* (blue, 1.84 ± 0.10 , n=8). Statistical significance was determined with
1480 a Mann-Whitney unpaired t-test.

1481
1482 **Figure 10 – figure supplement 2.** SYT7 overexpression reduces RRP refilling following 10 Hz
1483 stimulation. (A) Representative average eEJC quantal content for the indicated stimulation in 2
1484 mM external Ca²⁺ in control (black) and *elav^{C155}-GAL4; UAS-Syt7* (OE SYT7, magenta). (B)
1485 Representative average quantal content for the last 4 responses during 10 Hz and the 1st 14
1486 responses during 0.5 Hz in control (black) and OE SYT7 (magenta). (C) Quantification of
1487 P531/P530 ratio for control (black, 1.43 ± 0.052 , n=9) and OE SYT7 (magenta, 0.85 ± 0.068 , n=7).
1488 Statistical significance was determined with a Mann-Whitney unpaired t-test.

1489
1490 **Figure 11.** Tagging and location of endogenous SYT7. (A) CRISPR strategy used to insert RFP
1491 in frame at the *Syt7* 3' end to generate SYT7^{RFP}. Exon coloring is the same as Figure 1D. The guide
1492 RNA cleavage site is displayed in yellow. (B) Two *Syt7* UAS-RNAi lines (#1 and #2) were used

1493 to pan-neuronally knockdown SYT7^{RFP}. Western analysis of head extracts probed with anti-RFP
1494 (top panel) from SYT7^{RFP} adults following pan-neuronal knockdown of SYT7: lane 1: UAS-*Syt7*
1495 RNAi#1; SYT7^{RFP}: lane 2: *elav*^{C155}-GAL4, UAS-Dicer2; UAS-*Syt7* RNAi#1; SYT7^{RFP}: lane 3:
1496 UAS-*Syt7* RNAi#2; SYT7^{RFP}: lane 4: *elav*^{C155}-GAL4, UAS-Dicer2; UAS-*Syt7* RNAi line#2;
1497 SYT7^{RFP}. SYX1 antisera was used as a loading control (bottom panel). (C) Immunocytochemistry
1498 with anti-HRP (top) and anti-RFP (bottom) in SYT7^{RFP} 3rd instar larvae at muscle 6/7 NMJs.
1499 SYT7^{RFP} staining is abundant in the presynaptic terminal, with a few postsynaptic membrane
1500 compartments also labeled. (D) 3D rendering of the terminal bouton (left) from above. The
1501 SYT7^{RFP} intra-terminal compartment is labeled in magenta, with HRP-labeled plasma membrane
1502 indicated with a grey mesh. Scale bar = 2 μ m.

1503
1504 **Figure 11 – figure supplement 1.** Location of SYT7^{GFP} within synaptic boutons. (A)
1505 Immunocytochemistry with anti-HRP (top) and anti-GFP (bottom) in SYT7^{GFP} 3rd instar larvae at
1506 muscle 6/7 NMJs. SYT7^{GFP} staining, like SYT7^{RFP}, localizes throughout the presynaptic terminal.
1507 Scale bar = 2 μ m. (B) Synaptic bouton immunolabeled with anti-BRP and anti-GFP in SYT7^{GFP}
1508 larvae. SYT7 surrounds but does not co-localize with BRP-labeled AZs, similar to other previously
1509 described peri-AZ proteins. Scale bar = 1 μ m.

1510
1511 **Figure 11 – figure supplement 2.** Knockdown of SYT7^{RFP} with *Syt7* RNAi eliminates RFP
1512 immunostaining. (A) Immunocytochemistry with anti-HRP (cyan) and anti-RFP (magenta) in
1513 SYT7^{RFP} 3rd instar larvae without (left) or with *elav*^{C155}-GAL4, UAS-Dicer2; UAS-*Syt7* RNAi#1.
1514 (B) Immunocytochemistry with anti-HRP and anti-RFP in SYT7^{RFP} without (left) or with *elav*^{C155}-
1515 GAL4, UAS-Dicer2; UAS-*Syt7* RNAi#2 (right). Neuronal knockdown of SYT7^{RFP} eliminates
1516 presynaptic and most postsynaptic SYT7 staining, suggesting a small fraction of SYT7^{RFP} may
1517 undergo exosome-mediated transfer, as shown for SYT4. The majority of SYT7 protein resides in
1518 the presynaptic terminal. Scale bar = 2 μ m.

1519
1520 **Figure 12.** Localization of SYT7 in presynaptic terminals. Immunostaining for the indicated
1521 proteins in each panel was performed at 3rd instar larval muscle 6/7 NMJs. Staining for all panels
1522 except A were done in the SYT7^{RFP} endogenously tagged background using anti-RFP to label the
1523 SYT7 compartment, with the merged image shown on the right. The Pearson correlation

1524 coefficient (r) calculated from the cytofluorogram co-localization plots is shown on the upper right.
1525 All images are from single confocal planes. **(A)** Co-localization of the SV proteins SYT1 (left,
1526 magenta, anti-SYT1 antisera) and nSYB (middle, green, endogenous nSYB^{GFP}) as a positive
1527 control. The remaining panels show boutons co-stained for SYT7^{RFP} (left, magenta, anti-RFP
1528 antisera) and the indicated compartment marker (middle, green): **(B)** Dynamin (anti-DYN
1529 antisera); **(C)** SYX1 (anti-SYX1 antisera); **(D)** Reticulin like-1 (*elav*^{C155}-GAL4; UAS-RTNL1-
1530 GFP); **(E)** lysosomal Na⁺/H⁺ exchanger 1 (*elav*^{C155}-GAL4; UAS-NHE-GFP); **(F)** HRP (anti-HRP
1531 antisera); **(G)** BRP (anti-BRP Nc82 antisera); **(H)** nSYB (nSYB^{GFP}); **(I)** Atrial natriuretic peptide
1532 (*elav*^{C155}-GAL4; UAS-ANF-GFP); **(J)** SYT4 (endogenously tagged SYT4^{GFP-2M}); **(K)** RAB7
1533 (anti-RAB7 antisera); and **(L)** Golgin84 (anti-GOLGIN84 antisera). Co-localization plots were
1534 generated with normalized pixel intensity of stacked images of boutons from 3 animals, with the
1535 color representing the frequency of data points as shown in the right scale bar. The vertical line on
1536 the X-axis indicates the threshold used to identify pixels above background for the compartment
1537 stain. The horizontal line on the Y-axis represents the threshold used to identify pixels above
1538 background for SYT7. Scale bar = 1 μ m.

1539

1540 **Figure 12 – figure supplement 1.** SYT7 tubules reside in proximity to multiple presynaptic
1541 compartments. Immunostaining for endogenously-tagged SYT7^{RFP} (label) and a lysosomal marker
1542 (NHE), a late endosomal marker (RAB7) and a peri-AZ endosomal protein (RAB11). The merged
1543 image is shown on the right. Scale bar = 0.5 μ m.

1544

1545 **Figure 12 – figure supplement 2.** SYT7 localization is not altered by specific RAB protein
1546 manipulations. Dominant-negative (D.N), constitutively-active (C.A.) or wildtype (WT) RAB4,
1547 RAB5, RAB7 and RAB11 were expressed from UAS constructs with *elav*^{C155}-GAL4 in the
1548 SYT7^{RFP} background. Immunostaining with anti-HRP and anti-RFP to label the SYT7
1549 compartment is shown for each manipulation. Several manipulations resulted in extremely reduced
1550 larval viability and could not be analyzed. Scale bar = 1 μ m.

1551

1552 **Figure 12 – figure supplement 3.** Localization of compartment-specific markers in *Syt7* mutants.
1553 Immunocytochemistry with anti-HRP (cyan) and anti-GFP (green) in control and *Syt7*^{M1} 3rd instar
1554 larvae to label: **(A)** endogenously-tagged RAB5; **(B)** endogenously-tagged SYT4 (SYT4^{GFP-2M});

1555 (C) RAB7 (anti-RAB7 antisera); (D) NWK (anti-NWK antisera); and (E) endogenously tagged
1556 RAB11. No changes were observed in *Syt7^{M1}* mutants. Scale bar = 1 μ m.

1557

1558 **Figure 12 – figure supplement 4.** Model for SYT7 localization and function. SYT7 functions to
1559 decrease the fusogenicity of SVs in the RRP and slow refilling of the RRP following stimulation.
1560 SYT7 localizes to internal tubular membranes within the peri-AZ network. This location places
1561 SYT7 at a key node to modulate SV re-entry into the RRP in a Ca²⁺-dependent manner by
1562 interfacing with other membrane compartments and the SV sorting machinery at peri-AZs.

1563

Figure 1

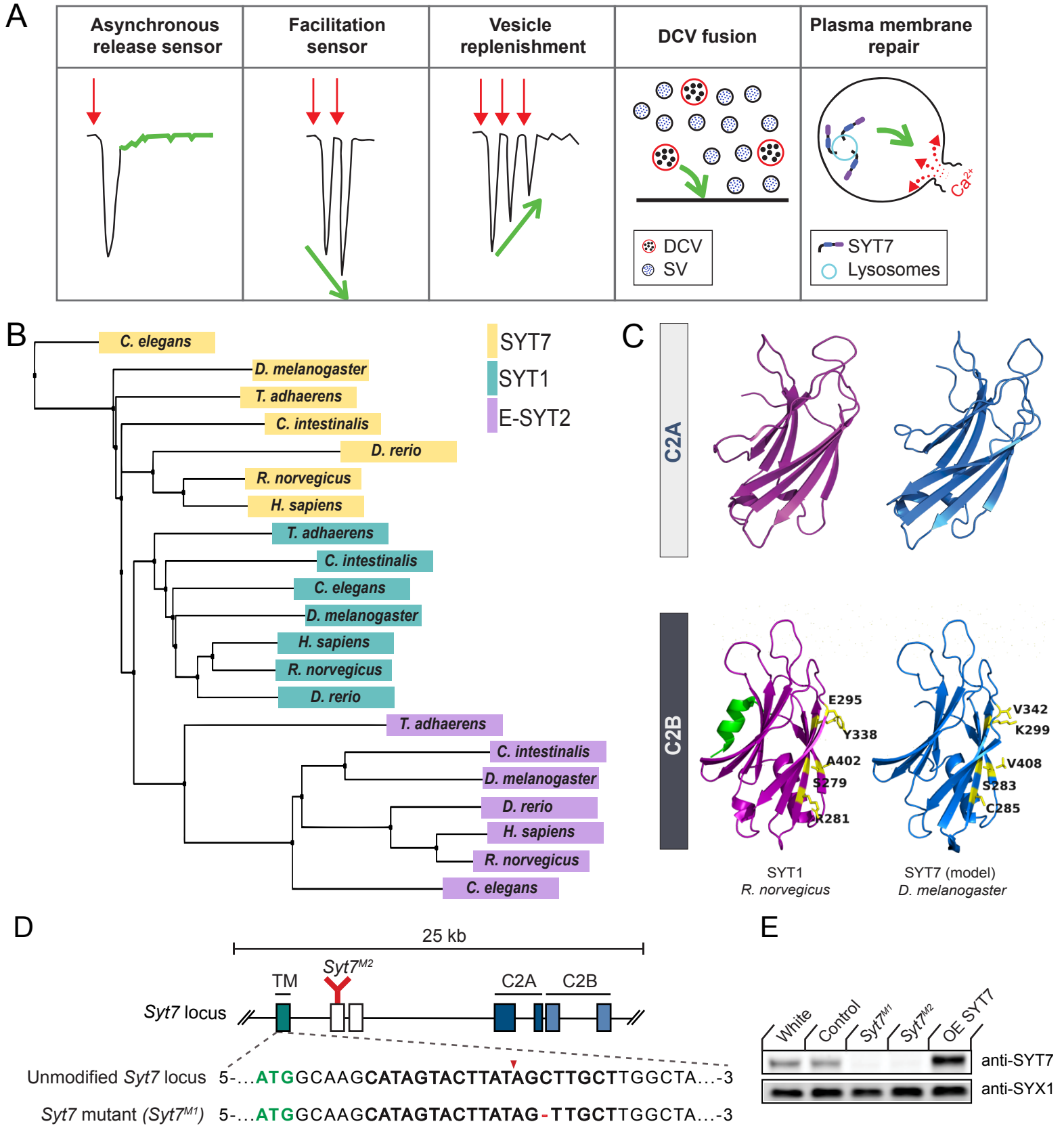


Figure 1- supplemental figure 1

A

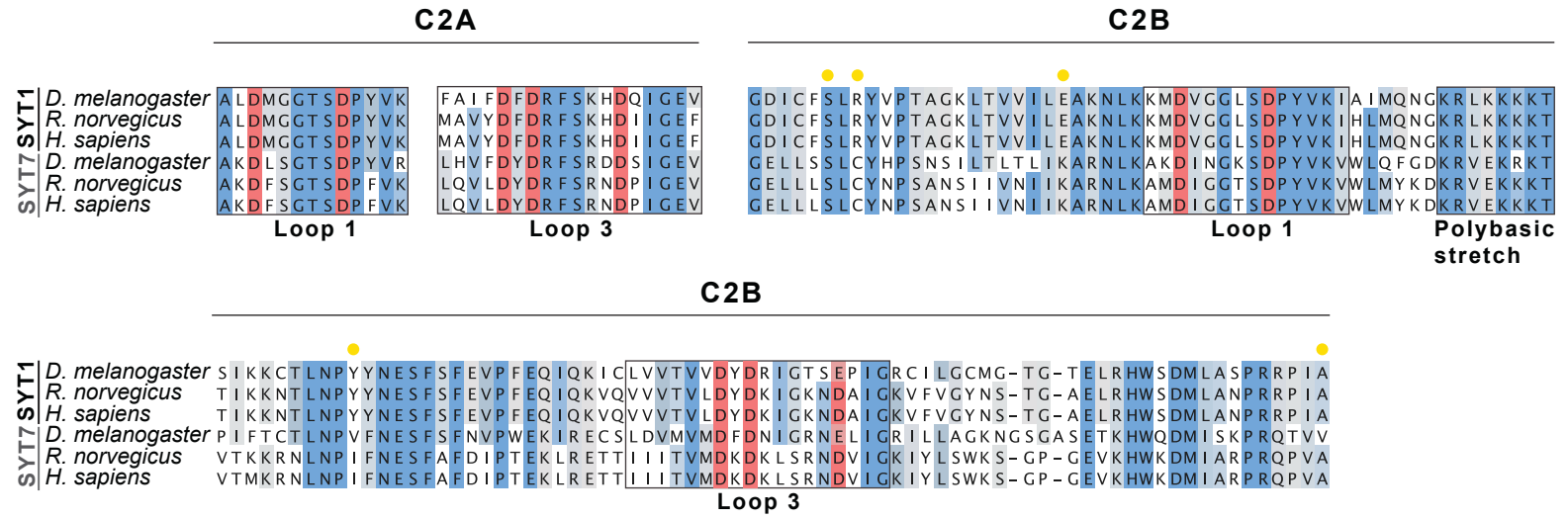


Figure 2

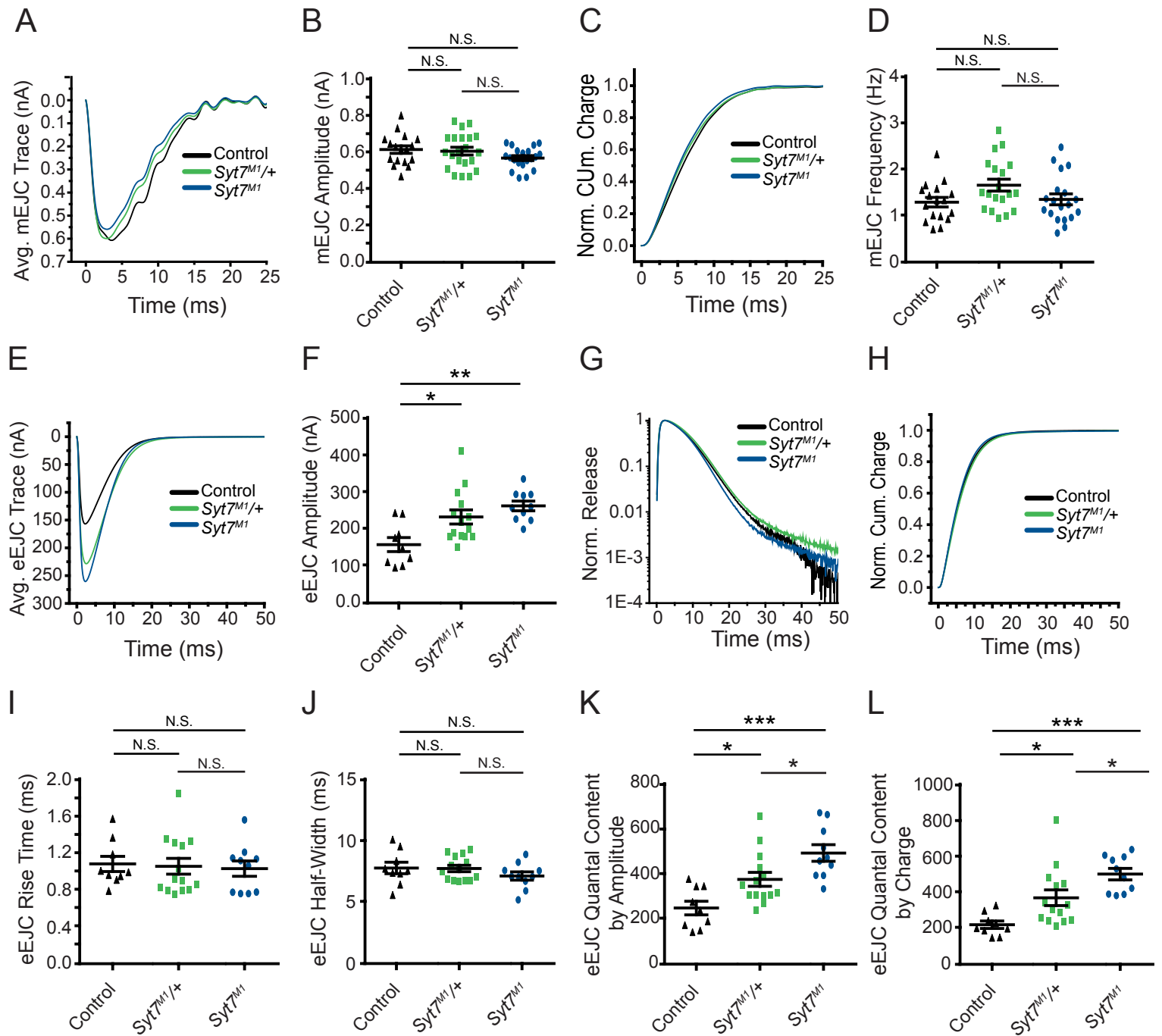


Figure 3

bioRxiv preprint doi: <https://doi.org/10.1101/2020.01.30.926246>; this version posted February 3, 2020. The copyright holder for this preprint (which was not certified by peer review) is the author/funder, who has granted bioRxiv a license to display the preprint in perpetuity. It is made available under aCC-BY 4.0 International license.

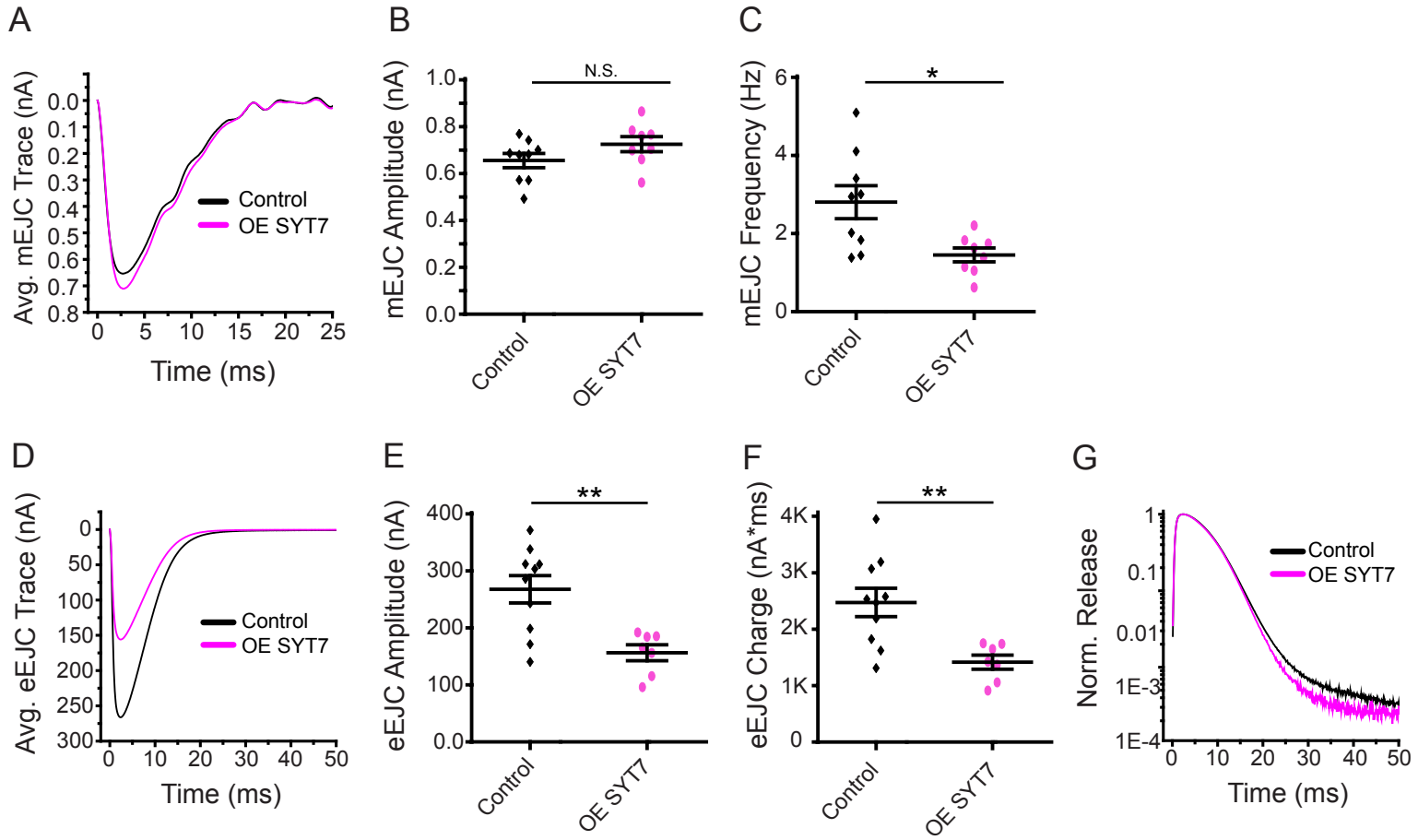


Figure 3 - supplemental figure 1

bioRxiv preprint doi: <https://doi.org/10.1101/2020.01.30.926246>; this version posted February 3, 2020. The copyright holder for this preprint (which was not certified by peer review) is the author/funder, who has granted bioRxiv a license to display the preprint in perpetuity. It is made available under aCC-BY 4.0 International license.

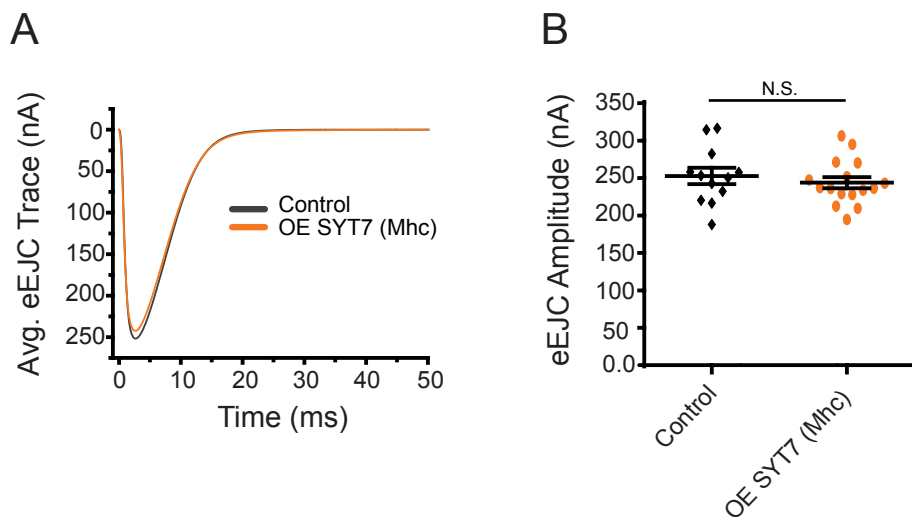


Figure 4

bioRxiv preprint doi: <https://doi.org/10.1101/2020.01.30.926246>; this version posted February 3, 2020. The copyright holder for this preprint (which was not certified by peer review) is the author/funder, who has granted bioRxiv a license to display the preprint in perpetuity. It is made available under aCC-BY 4.0 International license.

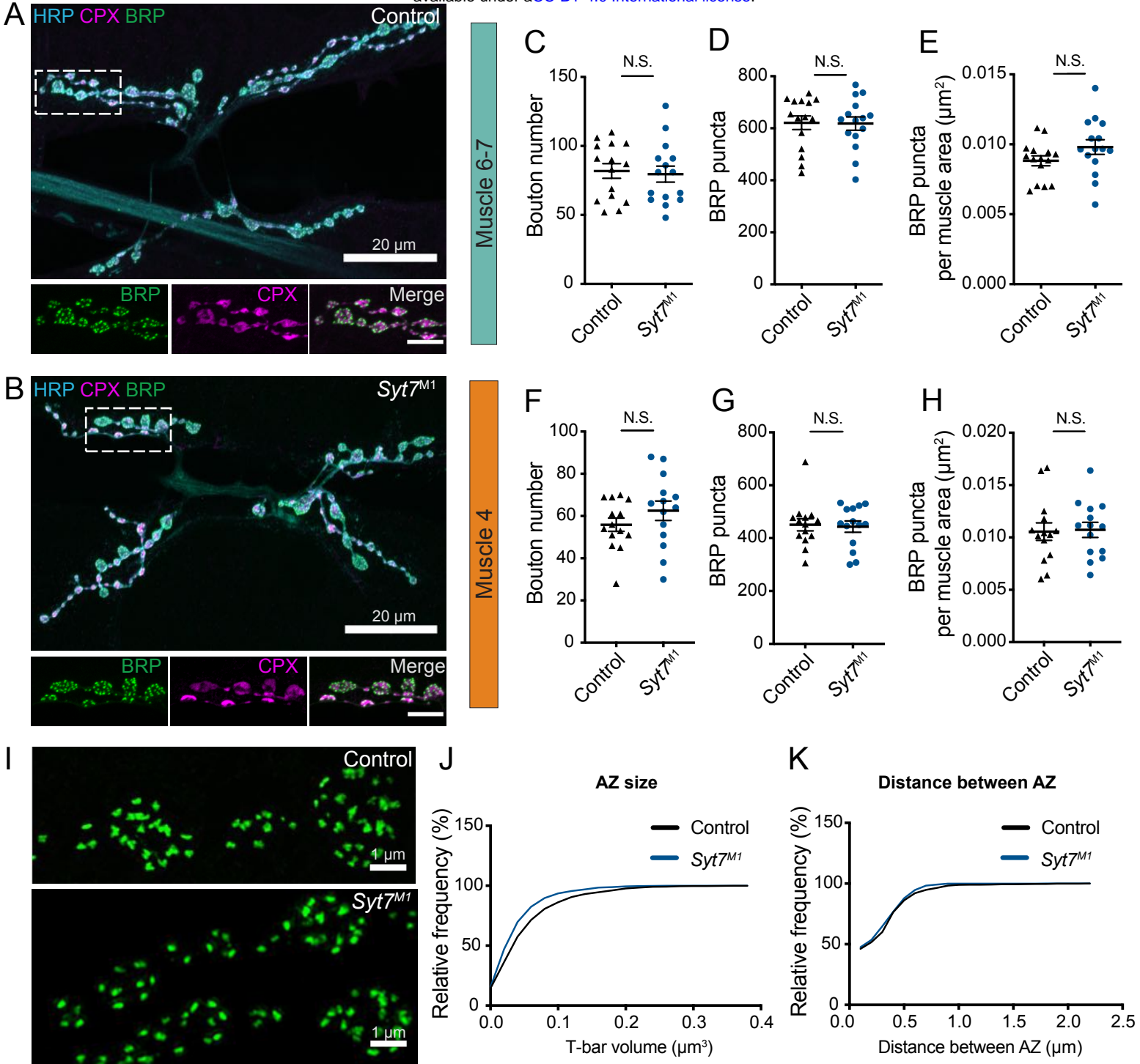
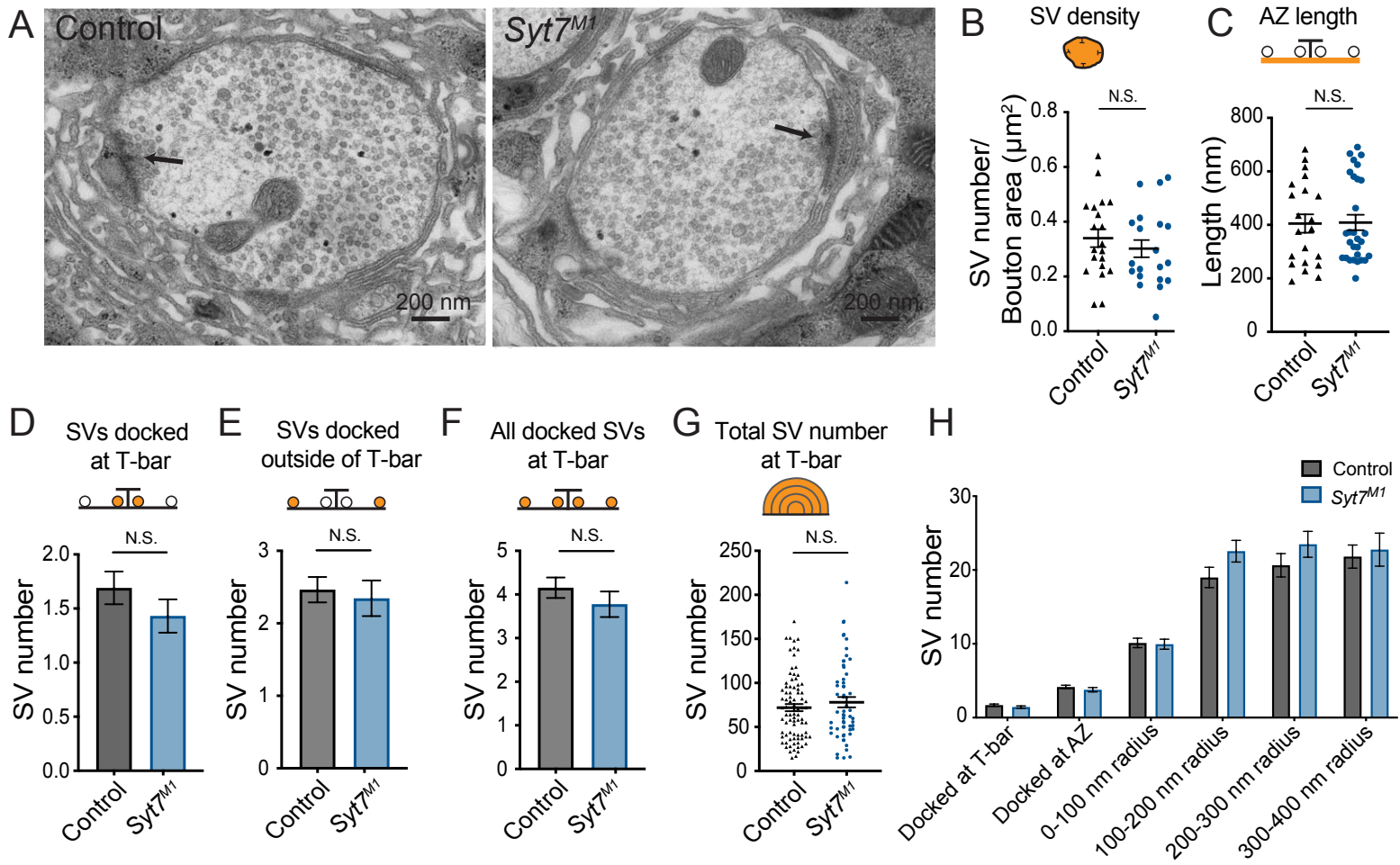


Figure 5

bioRxiv preprint doi: <https://doi.org/10.1101/2020.01.30.926246>; this version posted February 3, 2020. The copyright holder for this preprint (which was not certified by peer review) is the author/funder, who has granted bioRxiv a license to display the preprint in perpetuity. It is made available under aCC-BY 4.0 International license.



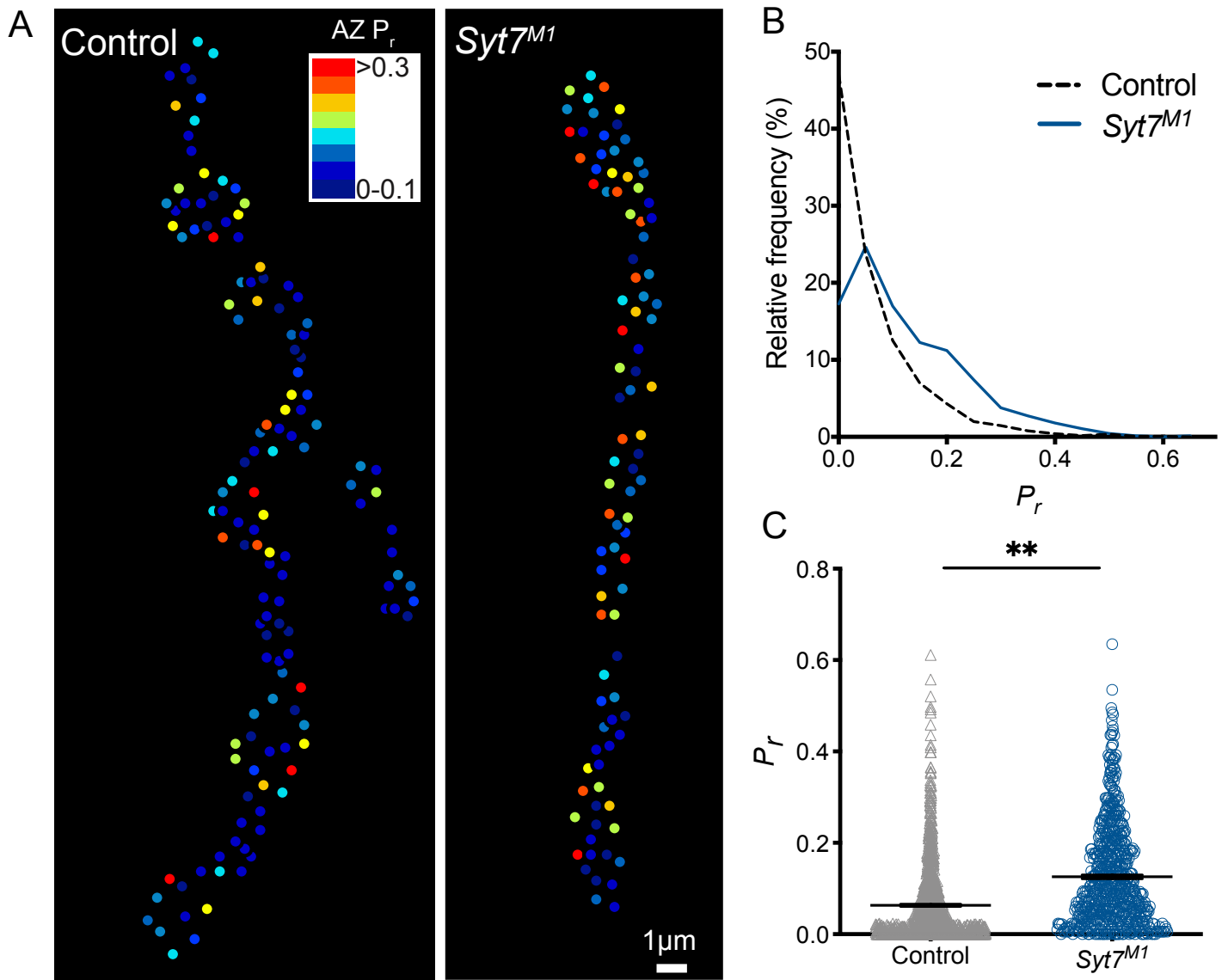


Figure 7

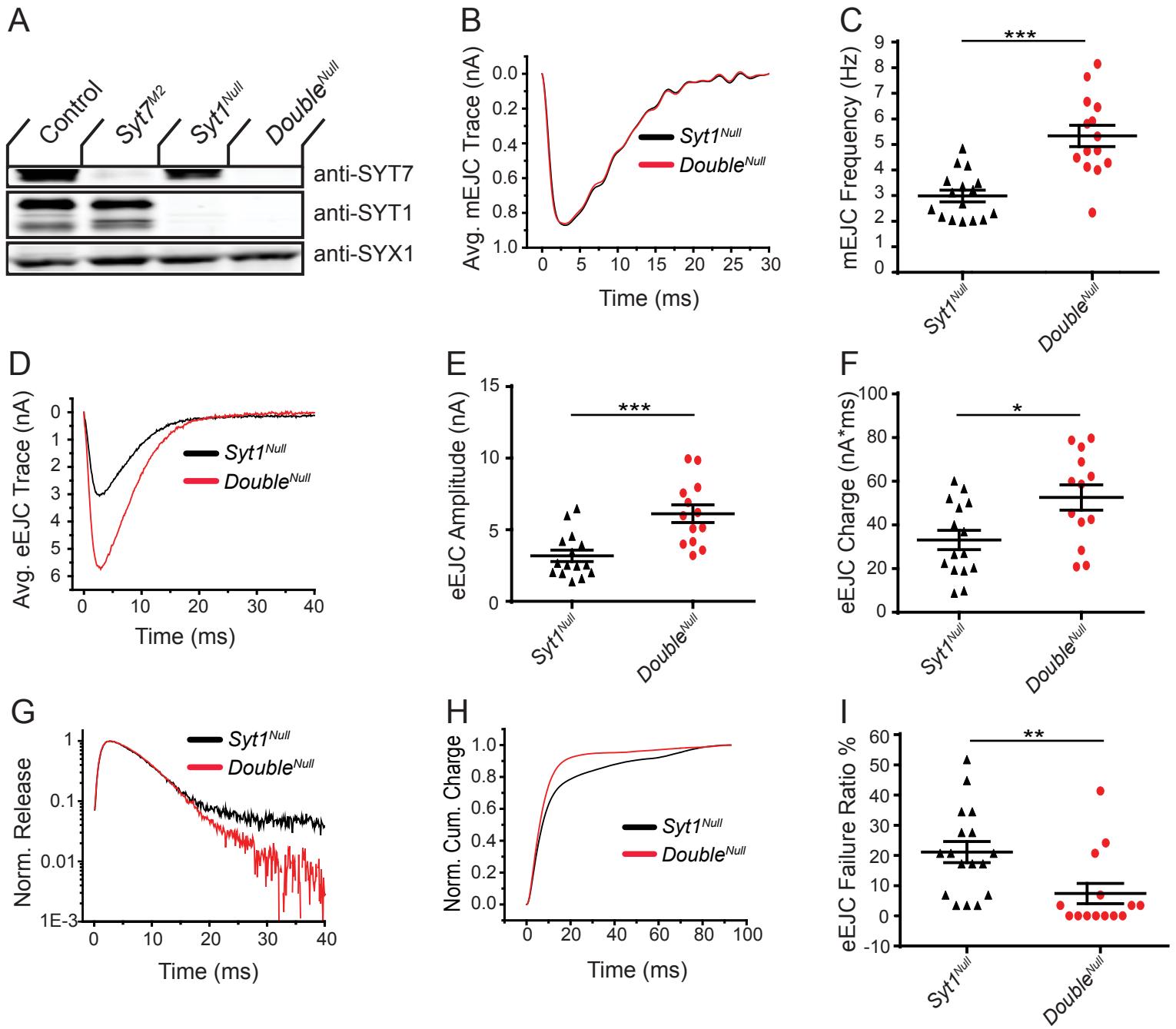


Figure 8

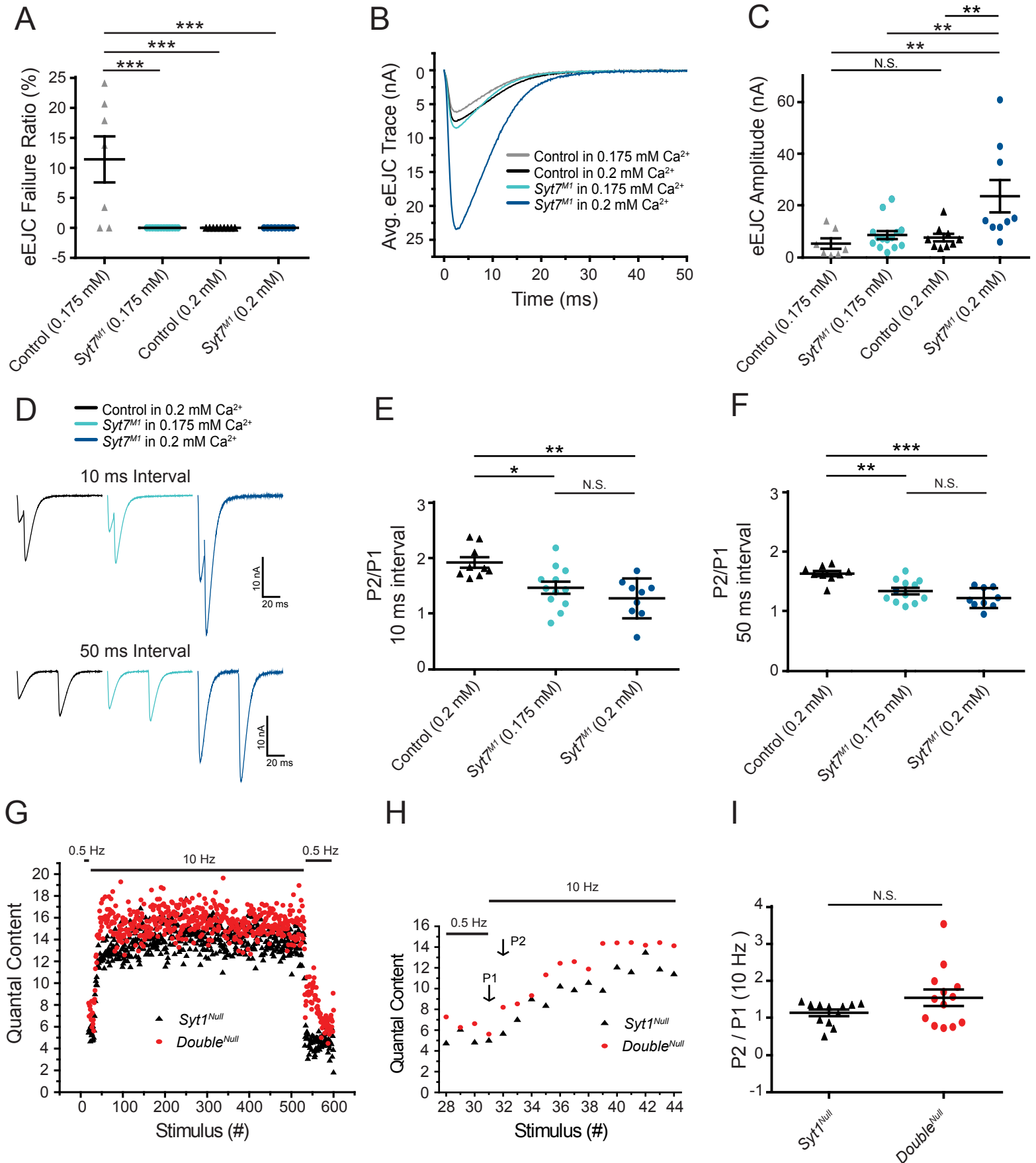


Figure 9

bioRxiv preprint doi: <https://doi.org/10.1101/2020.01.30.926246>; this version posted February 3, 2020. The copyright holder for this preprint (which was not certified by peer review) is the author/funder, who has granted bioRxiv a license to display the preprint in perpetuity. It is made available under aCC-BY 4.0 International license.

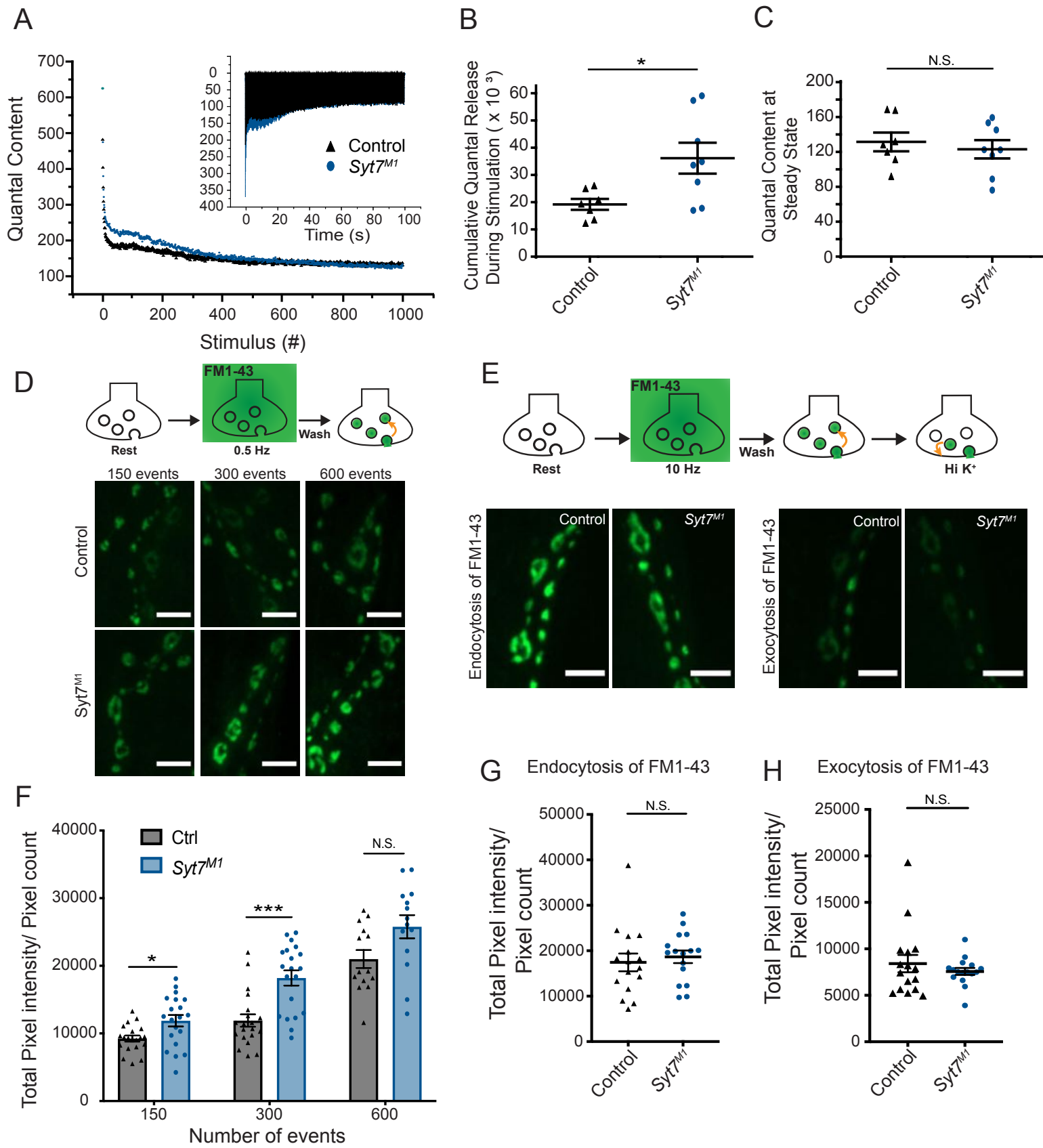


Figure 10

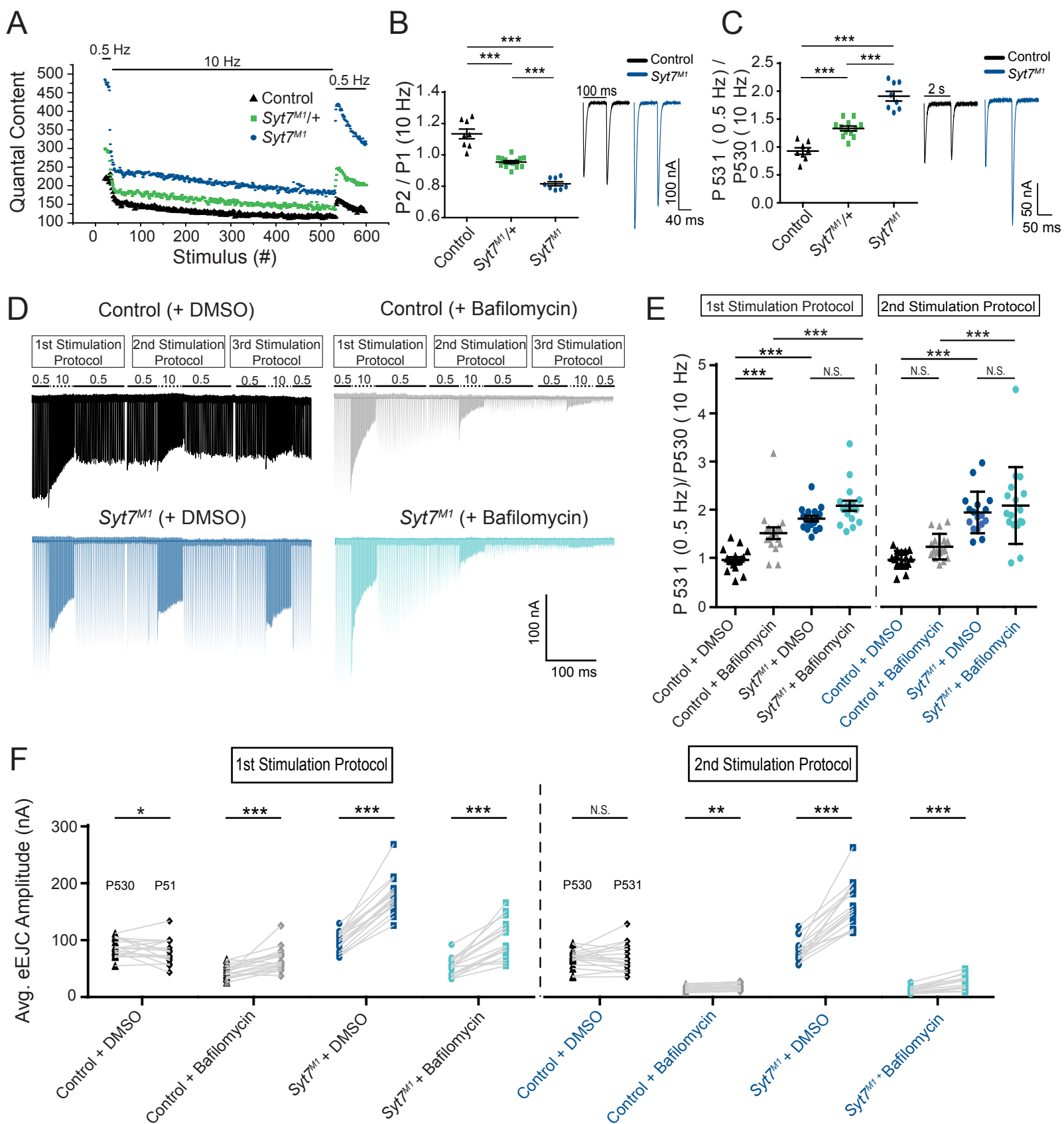


Figure 10 - supplemental figure 1

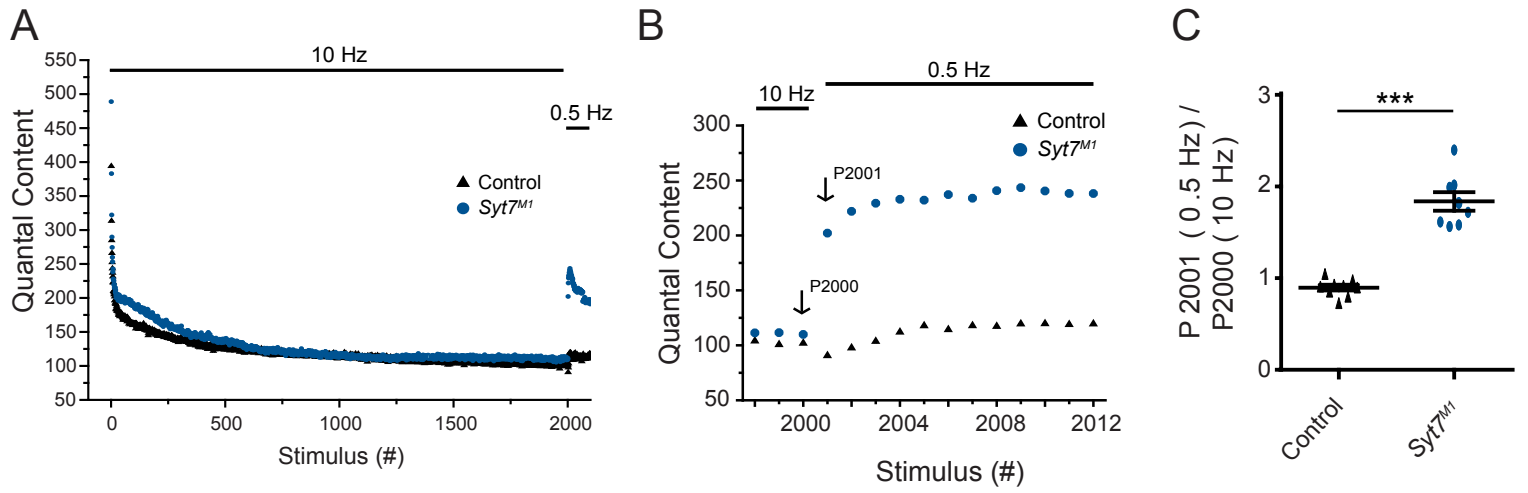


Figure 10, supplemental figure 2

bioRxiv preprint doi: <https://doi.org/10.1101/2020.02.03.952248>; this version posted February 3, 2020. The copyright holder for this preprint (which was not certified by peer review) is the author/funder, who has granted bioRxiv a license to display the preprint in perpetuity. It is made available under aCC-BY 4.0 International license.

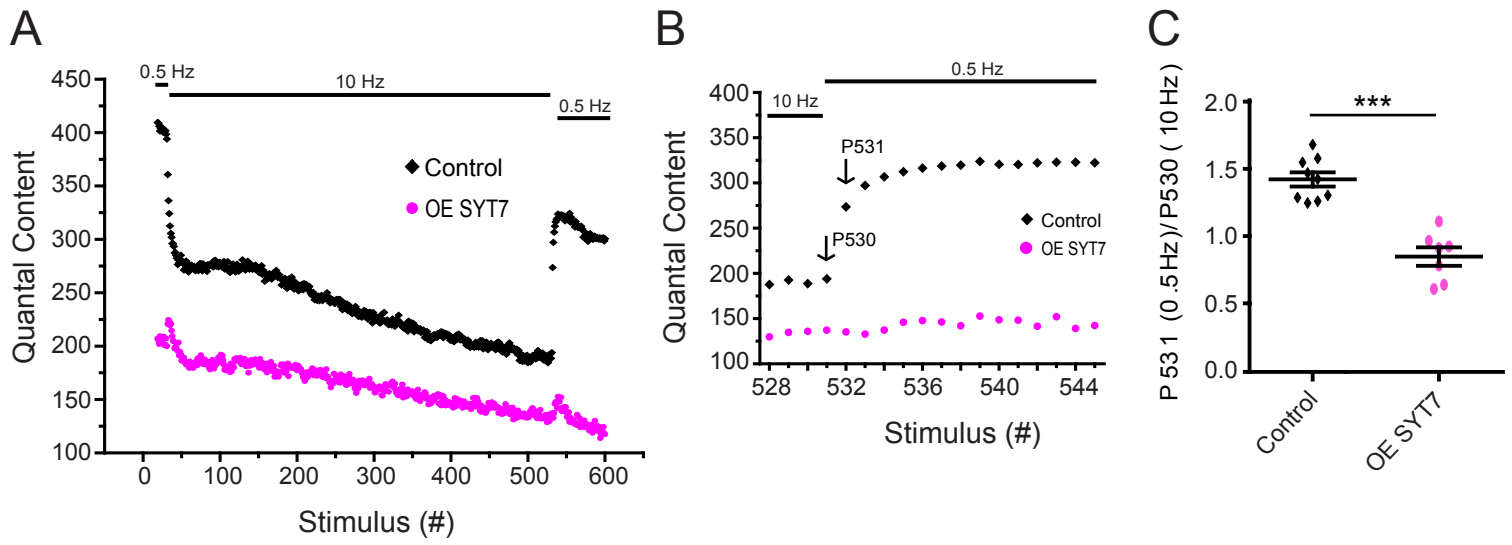


Figure 11

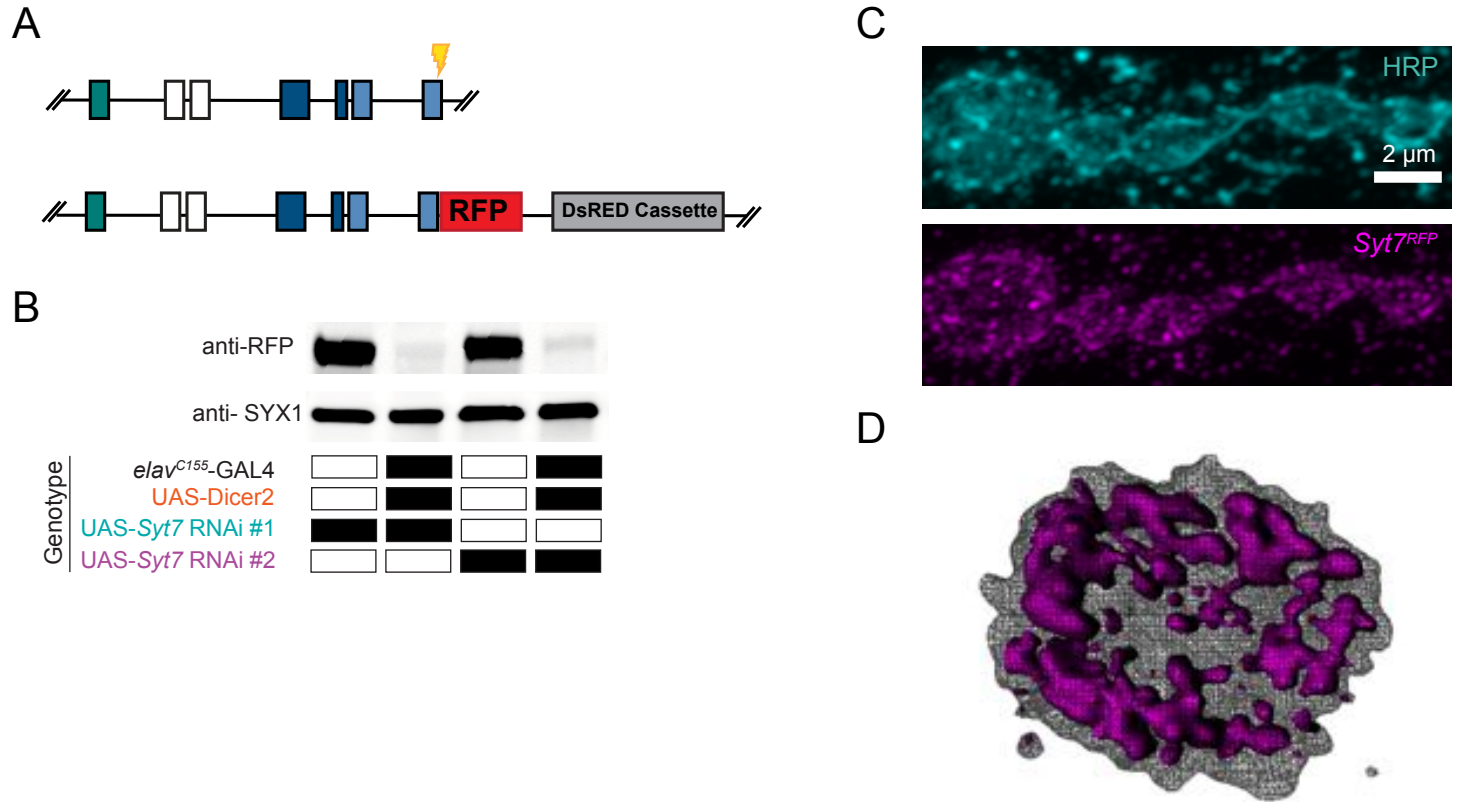


Figure 11 - supplemental figure 1

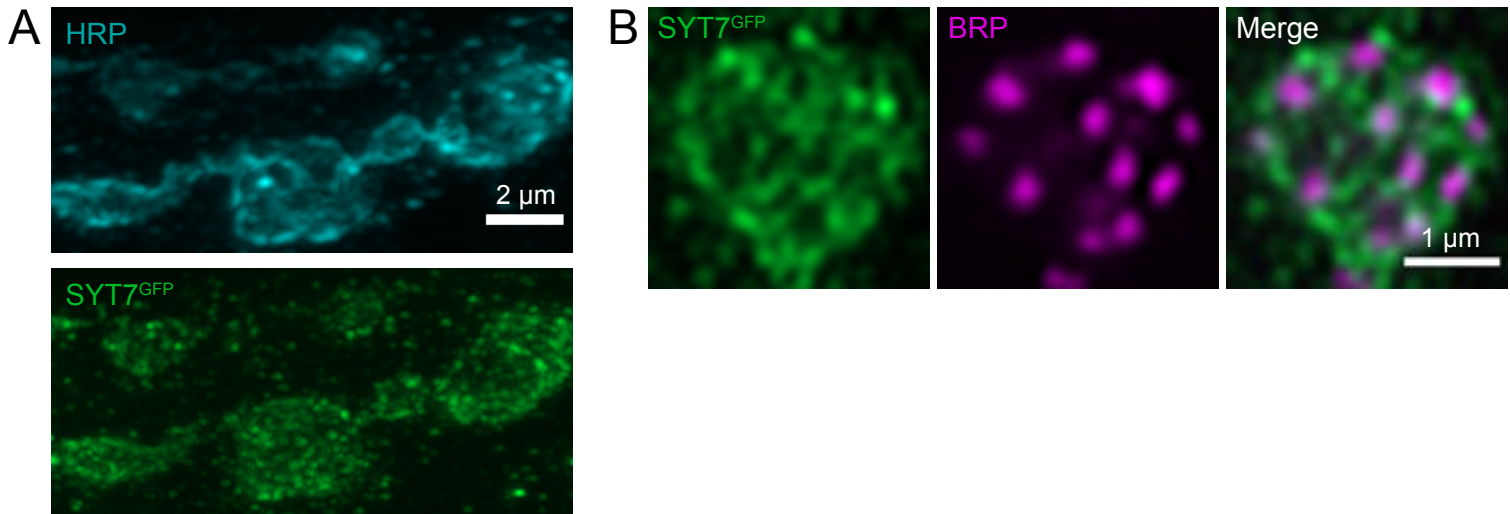


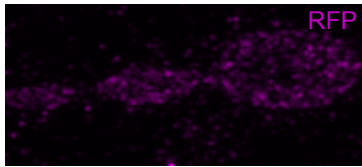
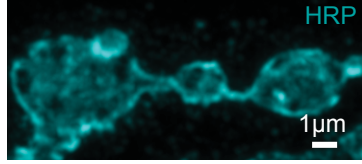
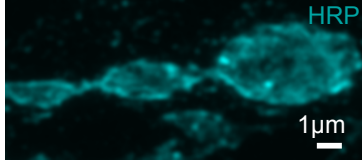
Figure 11 - supplemental figure 2

A

Syt7 RNAi 1

UAS-Syt7 RNAi 1
+ SYT7^{RFP}

elav^{C155}-GAL4>UAS-Syt7 RNAi 1
+ SYT7^{RFP}



B

UAS-Syt7 RNAi 2

UAS-Syt7 RNAi 2
+ SYT7^{RFP}

elav^{C155}-GAL4>UAS-Syt7 RNAi 2
+ SYT7^{RFP}

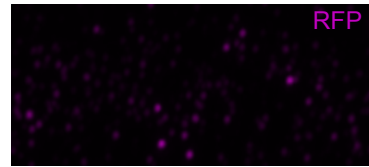
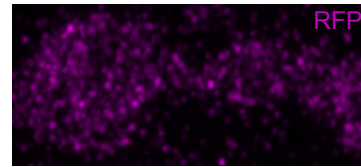
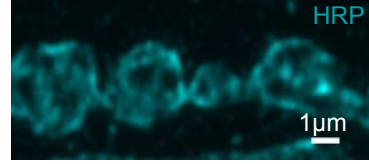
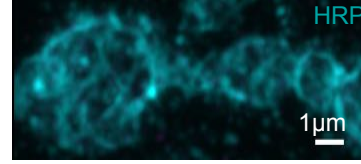


Figure 12

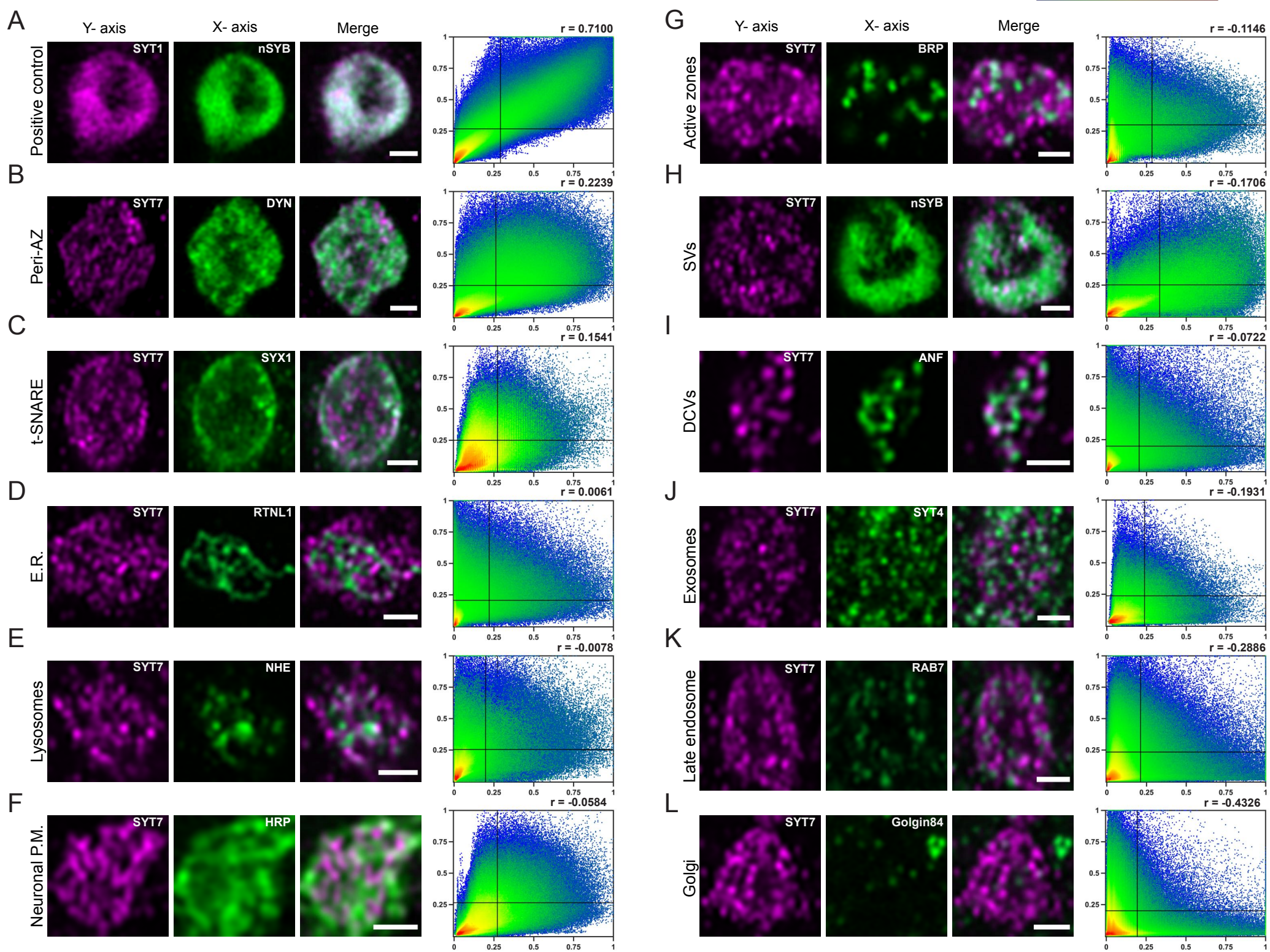


Figure 12 - supplemental figure 1

bioRxiv preprint doi: <https://doi.org/10.1101/2020.01.30.926246>; this version posted February 3, 2020. The copyright holder for this preprint (which was not certified by peer review) is the author/funder, who has granted bioRxiv a license to display the preprint in perpetuity. It is made available under aCC-BY 4.0 International license.

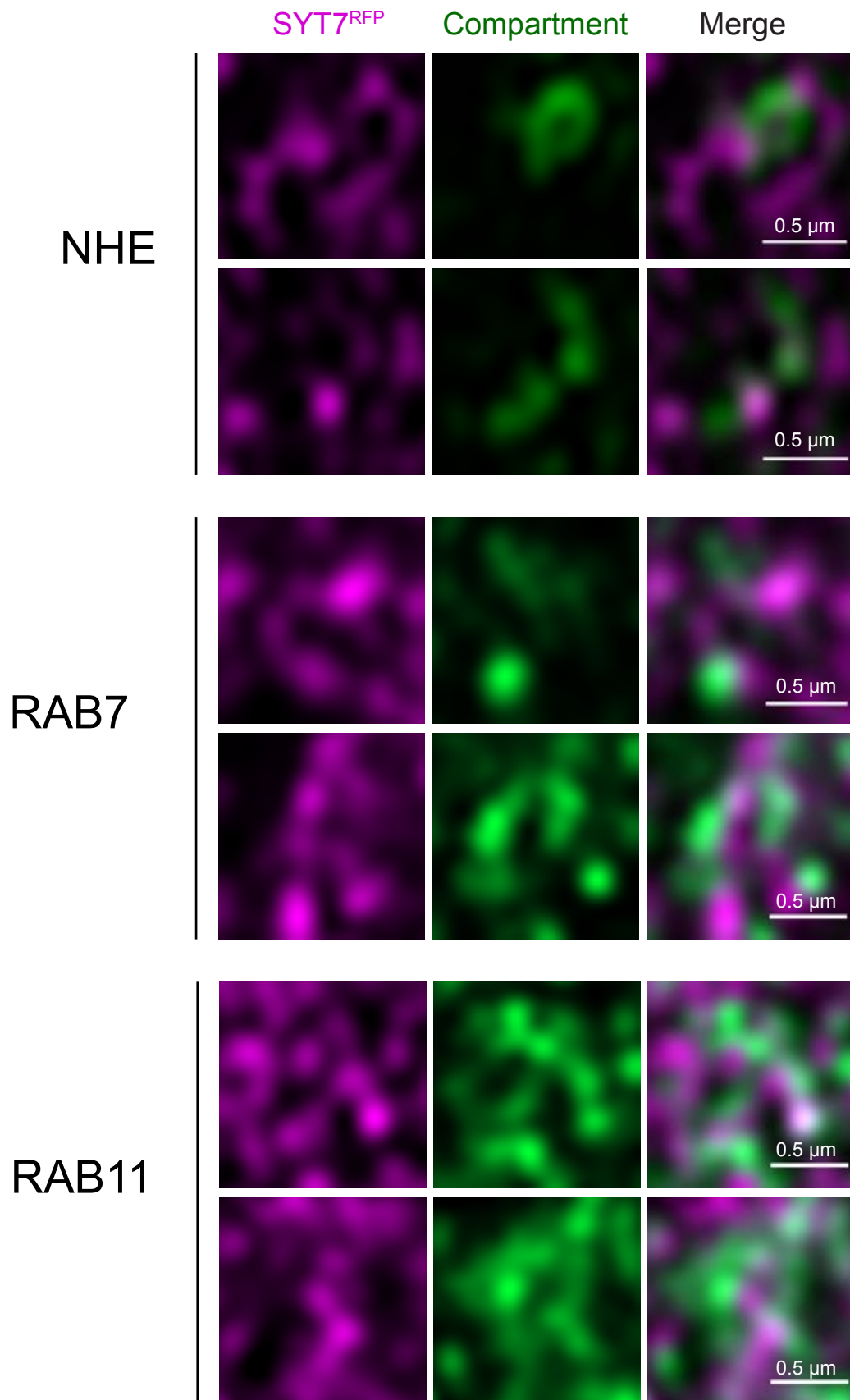


Figure 12 – supplemental figure 2

bioRxiv preprint doi: <https://doi.org/10.1101/2020.01.30.986244>; this version posted February 3, 2020. The copyright holder for this preprint (which was not certified by peer review) is the author/funder, who has granted bioRxiv a license to display the preprint in perpetuity. It is made available under aCC-BY 4.0 International license.

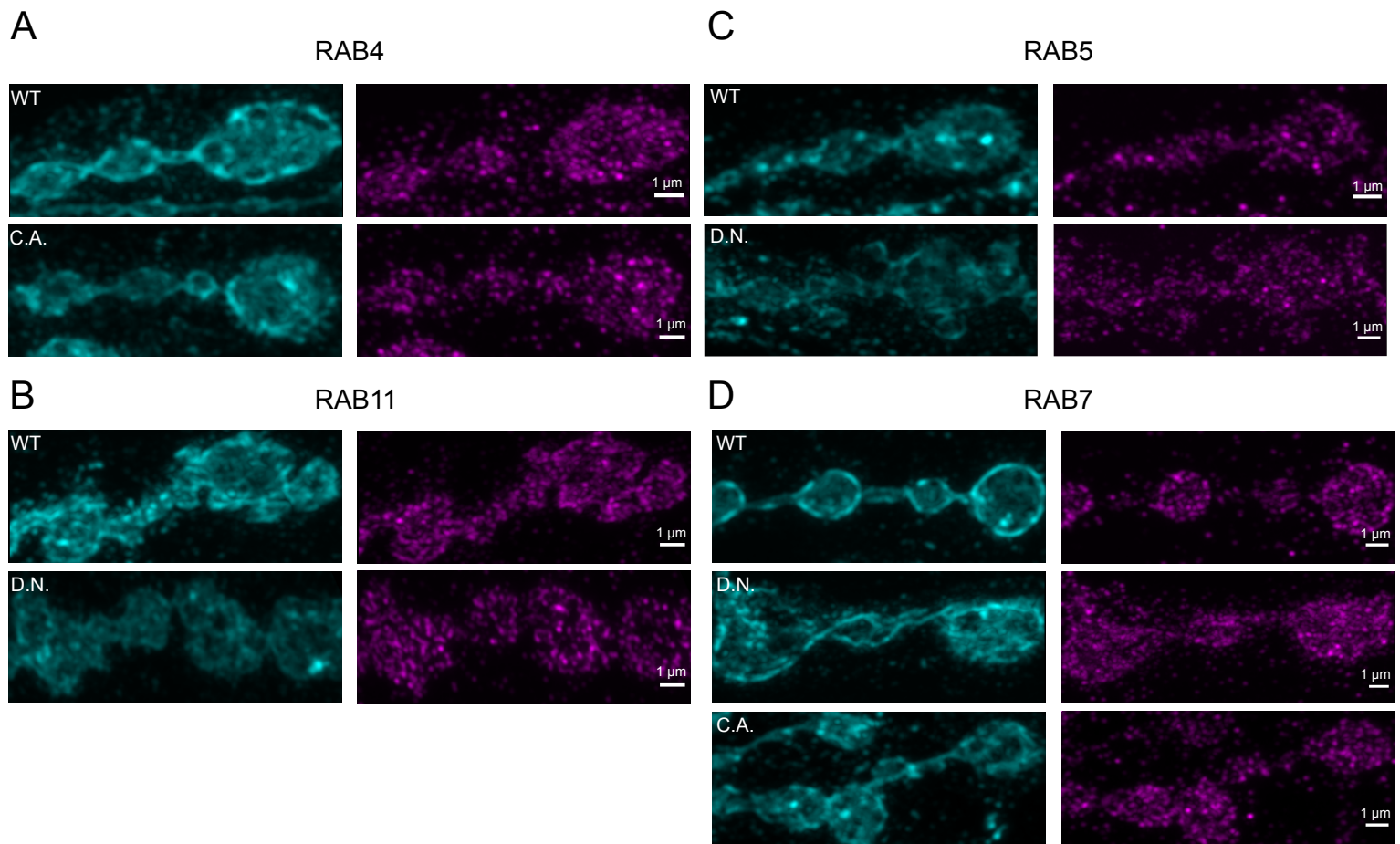


Figure 12 - supplemental figure 3

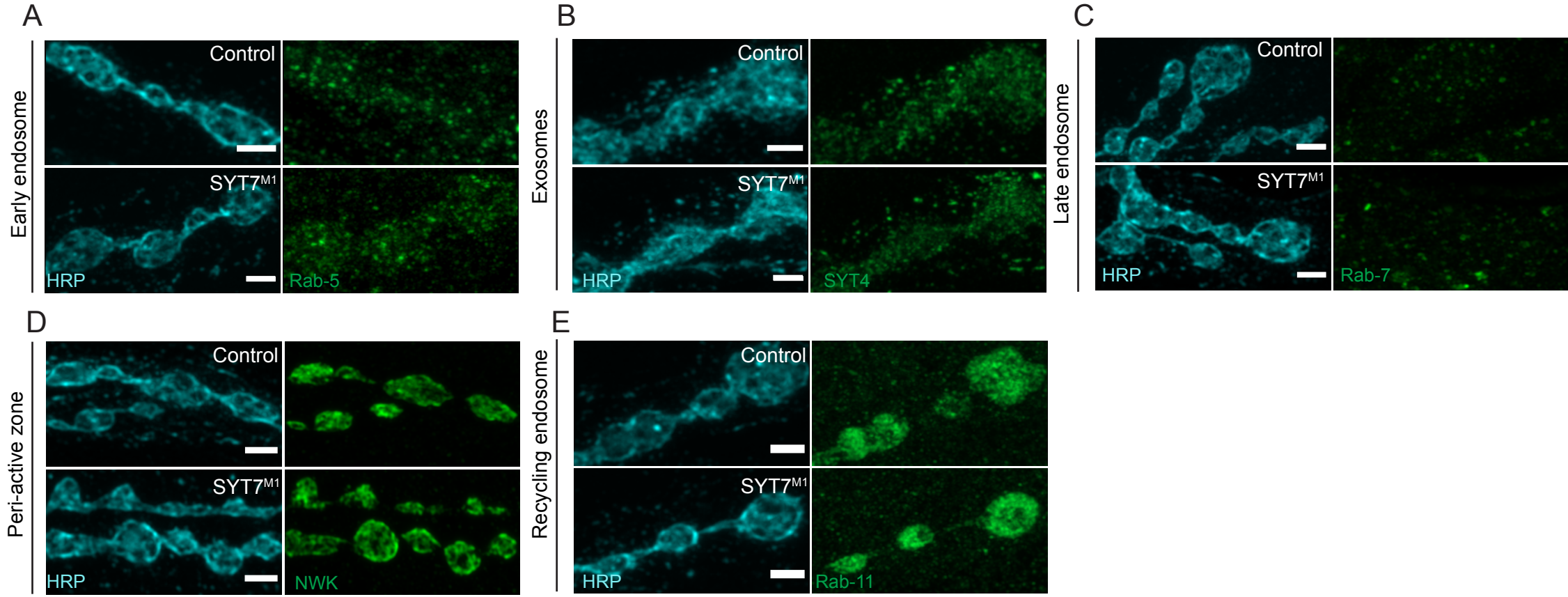


Figure 12 - supplemental figure 4

